Institut für Angewandte Photophysik
Fachrichtung Physik
Fakultät Mathematik und Naturwissenschaften
Technische Universität Dresden

Organic p-i-n Homojunctions: Fundamentals and Applications

Dissertation
zur Erlangung des
Doktorgrades der Naturwissenschaften
(Doctor rerum naturalium)

vorgelegt von
Kentaro Harada
geboren am 08.12.1966 in Fukuoka

Dresden 2008

Eingereicht am 06.03.2008

1. Gutachter: Prof. Dr. K. Leo
2. Gutachter: Prof. Dr. G. Paasch
3. Gutachter: Prof. Dr. M. Hiramoto

Verteidigt am 22.07.2008

Abstract

In this thesis, we study the physical properties of doped organic semiconductors. We first demonstrate the impact of doping on C_{60} films. In contrast to previous reports for organic thin films, the *n*-doped C_{60} films show a decrease of mobility with increasing doping levels; i.e., they follow the well-known Matthiessen rule which is generally observed in inorganic semiconductors. Using further strong organic donors and acceptors, we realize *p*-*i*-*n* homojunctions of several organic matrices: zinc-phthalocyanine, pentacene, and an iridium-complex TER004. We observe stable and reproducible diode characteristics, which can be described by the standard Shockley theory with an exception concerning the temperature dependence of the diode parameters. The current-voltage characteristics of the pentacene homojunctions under illuminated conditions indicate that the thermodynamic limitation of the open-circuit voltage is determined by the built-in voltage of 1.65 V, and that the recombination process is influenced by the distinct charge transport properties of electrons and holes. The very high built-in voltage of 2.2 V in the TER004 homojunction allows a red phosphorescent homo-OLED, which shows visible emission around 650 nm with low operation voltage. We examine the charge balance status in the homojunction structure, revealing that TER004 has superior electron transport properties.

Publications

a) Articles

1. K. Harada, A. G. Werner, M. Pfeiffer, C. J. Bloom, C. M. Elliott, and K. Leo, "Realization of organic pn-homojunction using a novel n-type doping technique", in *Proceedings of Organic Optoelectronics and Photonics* (SPIE, 2004), vol. 5464, pp. 1–9.
2. K. Harada, A. G. Werner, M. Pfeiffer, C. J. Bloom, C. M. Elliott, and K. Leo, "Organic homojunction diodes with a high built-in potential: Interpretation of the current–voltage characteristcs by a generalized Einstein relation", Phys. Rev. Lett. **94**, 036601 (2005).
3. F. Li, M. Pfeiffer, A. Werner, K. Harada, K. Leo, N. Hayashi, K. Seki, X. Liu, and X.-D. Dang, "Acridine orange base as a dopant for n doping of C_{60} thin films", J. Appl. Phys. **100**, 023716 (2006).
4. K. Harada, F. Li, B. Maennig, M. Pfeiffer, and K. Leo, "Ionized impurity scattering in n-doped C_{60} films", Appl. Phys. Lett. **91**, 092118 (2007).
5. Z. R. Hong, R. Lessmann, B. Maennig, Q. Huang, K. Harada, M. Riede, and K. Leo, "Antenna effects and improved efficiency in multiple heterojunction photovoltaic cells based on pentacene, zinc phthalocyanine and C_{60}", Appl. Phys. Lett., submitted.
6. K. Harada, M. Riede, K. Leo, O. R. Hild, and C. M. Elliott, "Pentacene homojunctions: Electron and hole transport properties and related photovoltaic responses", Phys. Rev. B, **77**, 195212 (2008).

b) Conferences

1. K. Harada, A. G. Werner, M. Pfeiffer, K. Leo, C. J. Bloom, and C. M. Elliott, "Organic pn-homojunction using a new class of organic donors", Frühjahrstagung der Deutschen Physikalischen Gesellschaft (Regensburg, 2004). In: Verhandl. DPG (Poster), SYOH 5.39.
2. K. Harada, A. G. Werner, O. Kühl, M. Pfeiffer, and K. Leo, "Organic p-i-n homojunctions: Fundamental properties and application in red phosphorescent OLED", Frühjahrstagung der Deutschen Physikalischen Gesellschaft (Berlin, 2005). In: Verhandl. DPG (Poster), p. 641.
3. K. Harada, A. G. Werner, O. Kühl, M. Pfeiffer, and K. Leo, "Organic p-i-n homojunctions: Fundamental properties and application in red phosphorescent OLED", 8th European Conference on Molecular Electronics – ECME8 (Bologna, 2005). In: Book of Abstracts (Oral contribution), p. 74.

4. K. Harada, A. G. Werner, O. Kühl, M. Pfeiffer, and K. Leo, “Organic *p*-*i*-*n* homojunctions: Fundamental properties and application in red OLED”, 3rd European Conference on Organic Electronics and Related Phenomena – ECOER’05 (Winterthur, 2005). In: Book of Abstracts (Oral contribution), p. 20.
5. K. Harada, F. Li, M. Pfeiffer, A. G. Werner, and K. Leo, “Field-effect mobility in *n*-doped C_{60} thin films”, Frühjahrstagung der Deutschen Physikalischen Gesellschaft (Dresden, 2006). In: Verhandl. DPG (Poster), p. 99.

c) Patents

1. A. Werner, M. Pfeiffer, K. Leo, K. Harada, and C. M. Elliott, “N-doping of organic semiconductors”, Application Nr. PCT/DE2004/002247, Publication Nr. WO2005/036667.
2. A. Lux, A. Werner, H. Hartmann, O. Kühl, K. Harada, A. Grüßing, M. Limmert, and S. Gessler, “Use of metal complexes as n-dopants for organic semiconductors and production thereof including their ligands”, Application Nr. PCT/DE2005/000372, Publication Nr. WO2005/086251.
3. J. Birnstock, A. Werner, M. Hofmann, J. Blochwitz-Nimoth, M. Pfeiffer, and K. Harada, “Arrangement for an organic pin-type light-emitting diode and method for manufacturing”, Application Nr. EP05008105.8 and EP07005048.9, Publication Nr. EP1713136 and EP1818996.
4. M. Pfeiffer, K. Leo, K. Harada, G. Schwartz, and K. Walzer, “Electroluminescent light-emitting device”, Application Nr. EP06000436.3, Publication Nr. EP1808909.
5. M. Pfeiffer, K. Harada, G. Schwartz, K. Walzer, A. Werner, T. Canzler, O. Zeika, and P. Wellmann, “Electronic component with at least one organic layer”, Application Nr. EP06026743.2, Publication Nr. EP1808910.

Contents

1 Introduction

> *You can know the name of a bird in all the languages of the world, but when you're finished, you'll know absolutely nothing whatever about the bird... So let's look at the bird and see what it's doing – that's what counts.*
>
> Richard Feynman

Some of the organic materials have been historically called "dyes" since their electronic transitions mainly occur in the range of visible light. We know that life on Earth relies on the benefits from the sun. Indeed, most living things produce and utilize organic compounds to enjoy solar energy and to maintain themselves, associated with a variety of life processes; e.g., rhodopsin for the visual pigment, chlorophyll for photosynthesis, luciferin for bioluminescence, etc.

The *artificial* organic dyes got in the spotlight when it was recognized that many of them are photoconductive, and intensive attention was paid toward applications in xerography developed by Carlson in 1938. The study of conductive charge-transfer complexes began with the discovery of an extremely high conductivity in a perylene-iodine complex by Akamatsu, Inokuchi, and Matsunaga in 1954, followed by the observation of metallic conduction in a fulvalene-quinonimine complex by Ferraris *et al.* and Coleman *et al.* in 1972. In the late 1970s, the pioneering works on conducting polymers by Heeger, Shirakawa, and Macdiarmid opened the new era of plastic electronics.

Organic semiconductors have recently gained much attention due to applications in a new class of optoelectronic devices, such as large-area organic light-emitting diodes (OLEDs) or low-cost organic solar cells (OSCs). Color organic electroluminescence display panels are demonstrating their competitiveness in the market: e.g., Sony Corporation has launched in December 2007 the world's first flat television based on OLED technology with a lifetime of 30,000 hours. Organic photovoltaic devices are an alternative to conventional silicon solar cells: Recently, the solar cell industry has faced a tight market for silicon feedstock. In view of the accelerating growth of global solar cell production, fabrication of low-cost OSCs may be a matter of urgency. Organic thin-film transistors and circuits have been investigated for many years, and are expected to be used in, e.g., display back panels: In recent years, their performance has become sufficient to attract serious attention from the electronics community. Understanding of the fundamental charge transport properties in organic thin films and related device characteristics are thus of great significance for the further development of optoelectronic applications and improvement of the energy conversion efficiencies.

Despite the progress in applications, the physical understanding of organic semiconductors is still much less developed than for inorganic semiconductors such as silicon. There are two important features that distinguish organic materials from inorganic ones: the generally low dielectric constant and the weak intermolecular coupling. The former leads to a large exciton binding energy, and the latter results in a narrow bandwidth and/or loss of coherence in the organic system. Research on carrier transport in organic materials has been traditionally divided in two areas: Much work was already done in the 1980s by the pioneering work of Karl *et al.* [1] on idealized single crystals. However, such single crystals are not suitable for large-area and low-cost device applications. Therefore, further research has concentrated on the development of thin-film electronic and optoelectronic devices. Complexity in the physical understanding may be introduced by two seemingly contradicting approaches to organic films: (1) the band model approach that emphasizes the solid-state characters of conduction states, describing them in terms of traditional band picture and delocalized charge carriers; (2) the hopping model approach that emphasizes the disorder features of a molecular aggregate, typically characterized by localization of charge carriers. Such dualism does not readily allow to apply the traditional concepts of solid-state physics to organic thin films, and it requires a search for new approaches.

In this thesis work, we take advantage of an alternative approach: Electrical doping of organic films with strong molecular donors and acceptors. Using the novel molecular doping methods, we can make a given organic semiconductor both n- and p-type conducting. We are thus able to prepare an organic variant of the p–n homojunction, which is the most basic device of semiconductor physics, with stable and reproducible diode characteristics. In our previous work [2], we have demonstrated that organic homojunctions composed of p- and n-type zinc-phthalocianine layers show characteristics adequately described by the Shockley equation with an exception concerning the temperature dependence of the diode parameters. The problem of realization of the molecular doping lies in the energetics between the host and dopant molecules; e.g., for n-type doping, the dopant should have the highest occupied orbital located energetically near or above the lowest unoccupied molecular orbital of the host material. In contrast to p-type doping already investigated in detail [3–5], the criterion is generally difficult to meet for n-doping since a low ionization potential of strong donor molecules makes them readily oxidizable in air. A solution to the problem is the n-doping with air-stable cationic dyes [6, 7]; e.g., doping of C_{60} with acridine dyes enables efficient charge transfer from the donor to the matrix, strongly increasing the bulk conductivity in the C_{60} films [8]. Further strong n-doping approaches have been developed by Bloom *et al.* [9] with a neutral form of ruthenium-terpyridine complexes utilizing an electrochemical synthesis of the transition metal complexes without exposure to air.

The scope of this work is to demonstrate that the transport properties and device characteristics in organic films can be in many aspects, despite the marked molecular features, described by the standard semiconductor theory without much complexity. For this purpose, we confine the arguments in this thesis to physics in organic thin-film systems with small molecules, especially those with excellent carrier transport properties. In the following discussion, we demonstrate that *n*-doped C_{60} films can indeed show transport properties strongly different from previous observations in organic thin films characterized by carrier localization: The data can be explained by the Matthiessen's rule generally applied for band transport in inorganic semiconductors.

The strong doping methods which are much more efficient than previous approaches make it possible to prepare an organic homojunction in materials with larger energy gap. We have chosen pentacene as the matrix for studies of photovoltaic effects in organic homojunctions. It can be shown that the thermodynamic limitation of open-circuit voltage in the organic homojunctions is in accordance with the energy conversion model developed for the description of inorganic solar cell performance. The concept of organic homojunctions can be further extended to the application in red phosphorescent OLED. A surprisingly large built-in voltage is observed due to the difference in the Fermi energies of the *p*- and *n*-type organic layers induced by the efficient doping with the strong acceptor and donor molecules.

We organize this thesis in the following way: Chapter 1 presents background theories essential for the following discussions, in which we place a particular emphasis on models of the transport properties in organic films by comparison with that in covalent crystals. In Chapter 2, we introduce and explain the features of organic materials used in this work, where the physical properties of the novel donor molecules are especially a matter of interest. Chapter 3 presents the experimental methods used in this work, and some of the theoretical basis necessary for analysis and interpretation of the results are also introduced.

Results and discussions consist of four Chapters: We first discuss in Chapter 4 the fundamental carrier transport properties in doped C_{60} thin films, utilizing temperature-dependent field-effect measurements to elucidate the scattering mechanism. Chapter 5 deals with the basic characterization of the archetype organic homojunctions. We show that several organic semiconductors can be used for the homojunction matrices, and their energetics are discussed in terms of carrier statics of the doped organic films. Chapter 6 discusses the temperature and light intensity dependence of solar cell parameters, such as open-circuit voltage and short-circuit current, of pentacene homojunctions. We also investigate influence of deep trap states in the matrix by using single-carrier homojunction devices. In Chapter 7, we discuss the performance of a red homo-OLED, utilizing a triplet-emitter compound as the matrix. An improvement of luminescent efficiency is discussed in terms of charge balance in the homojunction structure.

2 Physical Properties and Theories

In this Chapter, we give an overview of the basic physics necessary for understanding the experimental phenomena and subsequent discussions in this study. The first two sections deal with features of organic molecules upon formation of solid states. We only briefly explain general theories and related models referring to the simplest cases, yet there lies the very essence of the nature of organic materials. The third section deals with standard device theories, which are commonly used for inorganic semiconductors. Our main interest, the applicability of these theories to the organic solids, will be discussed later. In the last Section, we introduce carrier generation and recombination processes typically present in organic solids, together with the established models for real applications.

2.1 General Properties of Organic Small Molecules

2.1.1 Molecular Orbital Theory

Let us begin by considering the formation of a small molecule constituting of a number of atoms. Molecular orbital (MO) theory, developed in the course of modern chemistry, is a method for determining a given molecular structure. There, unlike in valence bond theory, electrons are not assigned to individual bonds between atoms, but are treated as moving under the influence of the nuclei in the whole molecule. The total number of orbitals is conserved; i.e., the number of MOs equals the number of original atomic orbitals. The theory asserts that atomic orbitals no longer hold significant meaning after atoms form a molecule, and that electrons no longer *belong* to any particular atom but to the molecule as a whole. MO theory was initially considered as a competitor to valence bond theory before it was realized that the two methods are closely related, and by an extension of the concepts, they eventually become equivalent.

Linear Combination of Atomic Orbitals

The linear combination of atomic orbitals (LCAO) does not give exact solutions to the Schrödinger equation, but provides approximate solutions. Several approximations and simplifications are required before LCAO to determine electronic energies in MOs. The first approximation can be made assuming that electrons can move much faster than nuclei: the Born-Oppenheimer approximation. We can therefore treat the nuclear and electronic motions independently. By neglecting the nuclear kinetic energy, the electronic Hamiltonian for solving the Schrödinger equation has a simple form.

The next approximation is known as the independent electron model. Assuming each electron to move in an *average potential*, which incorporates the interactions with the nuclei and an *averaged interaction* with the other electrons, the electronic Hamiltonian can be separated into individual parts:

$$\hat{H} = \hat{H}_1 + \hat{H}_2 + \cdots , \tag{2.1}$$

where $\hat{H}_i$ is dependent only on the properties of each electron. The total electronic energy is then given by: $E = \varepsilon_1 + \varepsilon_2 + \cdots$, i.e., by the sum of energies of the individual molecular orbital occupied with an electron. The problem is then reduced to an one-electron Schrödinger equation:

$$\hat{H}_i \Psi_i = \varepsilon_i \Psi_i, \tag{2.2}$$

where Ψ_i is the one-electron wavefunction of a molecular orbital.

The final approximation is made by the LCAO method. This method supposes that we can construct a MO by linear superposition of atomic orbitals centered on individual atoms as

$$\Psi_i = \sum_{j=1}^{n} (c_{ij} \Phi_j), \tag{2.3}$$

where Φ_i is an atomic orbital. The coefficients c_{ij} may be determined numerically, e.g., by insertion of Eq. (2.3) into the Schrödinger equation (2.2) and by application of a variational principle such as the Hartree-Fock method.

Energy Splittings

The linear combination of wavefunctions results in two types of solutions: symmetric and antisymmetric functions. An equal number of bonding orbitals and antibonding orbitals are thus formed. The splitting of energies between the two different types of orbitals generally depends on the degree of overlap of the atomic orbitals. For a qualitative understanding, we can consider two distinct atoms each having one electron: Let us now take the simplest case of homonuclear molecules, such as diatomic (H_2, He_2, O_2, $\cdots$) or ethylene (C_2H_4) molecules. As the atoms are brought together, their orbitals overlap, and the increasing Coulomb interaction between the atom cores and the electron splits the orbital energy levels. The eigenvalue of an LCAO orbital, $\Psi = c_1\Phi_1 + c_2\Phi_2$, is given by

$$\varepsilon = \frac{c_1^2\beta_1 + 2c_1c_2\gamma_{12} + c_2^2\beta_2}{c_1^2 + c_2^2 + 2c_1c_2S}, \tag{2.4}$$

leading to nontrivial solutions for the energy

$$\begin{aligned} \varepsilon &= (\beta + \gamma)/(1 + S) \quad && \text{bonding} \\ \varepsilon^* &= (\beta - \gamma)/(1 - S) \quad && \text{antibonding,} \end{aligned} \tag{2.5}$$

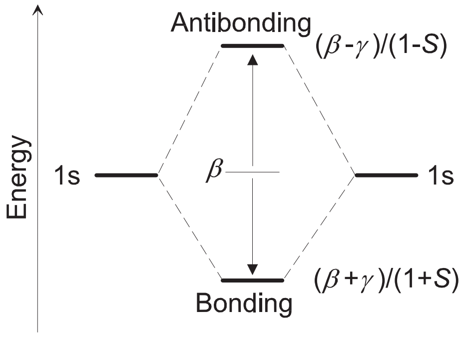

Figure 2.1: Evolution of the energy levels of an aromatic molecule with an LCAO approach.

where β_j (for a homonuclear molecule, $\beta = \beta_1 = \beta_2$) is known as the *Coulomb integral* which equals the energy of an electron in the corresponding atomic orbital j in the molecular environment. $\gamma_{jk}\,(\gamma = \gamma_{12})$ is the *resonance integral* which is a measure of the strength of bonding interaction as a result of overlap of the orbital j and k. S represents the *overlap integral* which is a measure of the effectiveness of overlap of the orbitals.

The bonding orbital is *bonding* in the sense that it is lower in energy than its constituent atomic orbitals. Neglecting the overlap integral S, the splitting between the bonding and antibonding orbitals is approximately 2β, as it can be derived from Eq. (2.5). The number of split MOs is equal to the number of contributing atomic orbitals. Figure 2.1 shows a schematic of evolution of the energy levels for the simplest case.

Extended π systems

Orbitals that are symmetric with respect to reflection in a dihedral plane are denoted as "σ", and those antisymmetric are called "π" orbitals. In a hydrogen molecule, the atomic 1s orbitals can overlap in a σ fashion to form a σ-bonding orbital and a σ-antibonding orbital. A π-type MO can be constructed on spatially extended groups of atoms. Let us imagine for instance each atomic p orbital contributing an extended π system: This MO is parallel to the p orbitals on neighbouring atoms so that they can engage in a π fashion. Another example is lone-pair electrons contained in antisymmetric orbitals, which are usually strongly delocalized and considered to form a part of the π system, called "n" orbitals.

Electrical conductivity and photosensitivity can be often found in aromatic hydrocarbons and conjugated heterocyclic compounds. These molecules contain delocalized π systems as well as heteroatoms with n electrons. It is just the π and n orbitals, which are the potential sources of charge carriers in organic semiconductors.

As an example, the MO picture of a benzene molecule composed of six identical C-C bonds is schematically shown in Fig. 2.2. In this molecule, 24 of the 30 total valence orbitals are devoted to form twelve σ bonding MOs [Fig. 2.2 (a)], which are mostly located between pairs of atoms (C-C or C-H). For simplicity, we here consider the ground state MO only: The remaining six p orbitals may participate in three π bonding MOs that are delocalized around

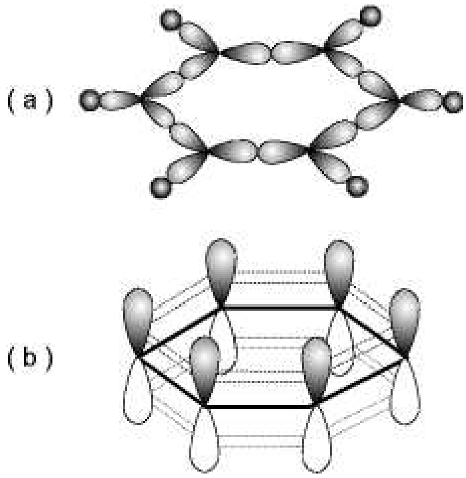

Figure 2.2: Schematic view of the (a) σ and (b) π framework of benzene molecular orbitals.

the ring. The two rings in Fig. 2.2 (b) above and below the plane of the molecule represent one MO. Two delocalized electrons may be found anywhere within those rings, but will not resemble the atomic p electrons any longer. The other four delocalized electrons may exist in two similar (but energetically not identical) MOs. All of these six delocalized π electrons thus reside in a large space.

Koopmans' Theorem

The orbital energies ε_i resulting from quantum-mechanical calculations can be associated with measurable quantities by means of Koopmans' theorem:

1. The energy of an occupied orbital in Ψ_i is equal to minus the ionization potential (IP) for the orbital, i.e., to the amount of energy needed to bring an electron onto the orbital from the vacuum level;
2. The energy of a virtual orbital in Ψ_i is equal to minus the electron affinity (EA) for the orbital, i.e., to minus the amount of energy gained when an electron is brought from infinity and added to the molecule.

Usually, the terms ionization potential and electron affinity refer to IP_1 and EA_1—that is, the lowest IP and the highest EA for the molecule. The applicability of Koopmans' theorem to real molecules is based on some assumptions that are only approximately valid. It neglects the following effects:

1. The reorganization energy of the electrons in the ion;
2. The difference between the correlation energy of the neutral molecule and that of the ion.

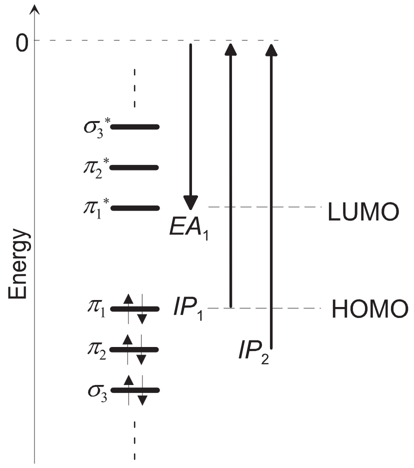

Figure 2.3: Koopmans' theorem: The highest occupied molecular orbital π_1 corresponds to the ionization potential IP_1; the lowest unoccupied molecular orbital π_1^* corresponds to the electron affinity EA_1.

The first point is due to the fact that a charge distribution of the residing electrons gives rise to an effective potential for each particular electron. If an electron is then removed, this effective potential is naturally altered. The second point is due to the tendency towards mutual avoidance by electrons of the same spin. Indeed, the correlation energy is generally neglected in the first and second order approximation of the variational method. Koopmans' theorem states that these alterations are small. Despite the limited accuracy, the terms "highest occupied molecular orbital (HOMO)" and "lowest unoccupied molecular orbital (LUMO)" are commonly used by convention to refer to *IP* and *EA*, respectively.

2.1.2 Self-Polarization in Organic Solids

When organic molecules condense to form a solid phase, the molecular features tend to retain their individuality, i.e., the electronic structure of a molecule changes only slightly due to weak intermolecular interaction of van der Waals type. Therefore, organic solids differ considerably in their mechanical, optical, and electronic properties from covalent or ionic crystals with a strongly bonded rigid atomic or ionic lattice characterized by complete loss of individual properties of the atomic particles. On the other hand, the energy relaxation caused by the displacement of dipole moments existing in a lattice environment is not negligible, especially for highly polarizable organic compounds such as aromatic and heterocyclic molecules. From these aspects, the LCAO eigenvalues calculated for an isolated molecule are actually not valid for the molecules in the condensed matter.

Spectroscopic measurements reveal that the ionization potential of an anthracene crystal is by about 1.5 eV lower than that of an isolated molecule [10]; i.e., the ionization of a solid requires less energy than that of a molecular gas. This can be attributed to the energy gain P_h caused by the electronic polarization of the solid during the ionization process. The

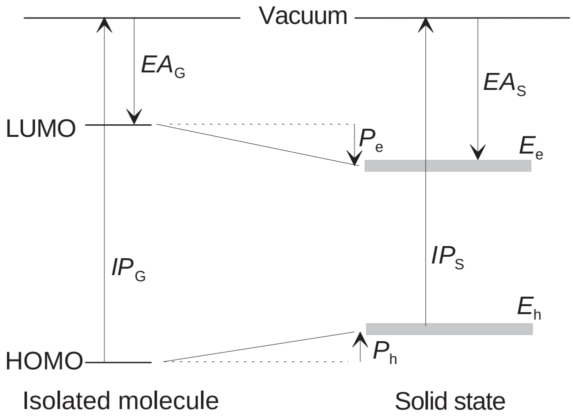

Figure 2.4: Schematic energy diagram of isolated and solid states of an organic molecule. IP_{G} and EA_{G} refer to the ionization potential and electron affinity, respectively, in the isolated state. IP_{S} and EA_{S} are those in the solid state.

evolution of a valence level E_h in a organic solid due to the effect of self-polarization is schematically indicated in Fig. 2.4.

Similarly, the electron affinity EA_{S} of a solid can be defined approximately by the sum of the electron affinity EA_{G} of a molecule and the electronic polarization P_e of the surrounding molecules, leading to a conduction level E_h. Thus, self-energies E_h and E_e are of those quasi charge particles determined by many-electron interactions within the solid state, and the energy levels differ from the HOMO and LUMO for an isolated molecule. Nevertheless, we will use in this study by convention the terms “HOMO” and “LUMO” to refer to those levels in organic solids.

Polarons

The effects of polarization by quasilocalized charge carriers in organic solids are categorized in terms of their different interaction types; i.e., vibronic, phononic, and electronic interactions. The typical relaxation times for the three polaronic interactions are summarized in Table 2.1.

Intramolecular vibrations are specific features of organic systems. Therefore, an interaction of a quasilocalized carrier with the intramolecular vibronic modes can be expected to take place in most of the organic solids. The vibronic relaxation results in changes in the bond lengths and the vibrational frequencies of the molecule due to a redistribution of the localized charge. This dynamic state is called a *vibronic polaron.* Another type of polaron is due to an interaction with phonons. Lattice relaxation times in organic crystals are in general large, and the interaction of a quasilocalized charge with surrounding lattice vibrations is usually not possible. However, a *lattice polaron* due to the local lattice deformation may be formed when the charge carriers reside in shallow traps in which the mean capture time of carriers is larger than the lattice relaxation time.

The most important effect upon formation of the molecular solid phase is, however, electronic polarization. A localized charge carrier manages to polarize the electron orbitals of surrounding neutral molecules in the solid. The time needed for the induced dipole formation is very short; therefore, the charge carriers appear to move together with their electronic polarization *cloud*. Such a quasistatic formation is called an *electronic polaron*. We shall again deal with electronic polarons in Section 2.2 in the context of *carrier localization*.

Table 2.1: Various types of polaron interactions. Typical relaxation time scales and interaction energies of a charge carrier in an anthracene-type crystal. (After [11])

Interaction type	Relaxation time scale (s)	Interaction energy (eV)
Electronic polarization	$10^{-16} \sim 10^{-15}$	1.0∼1.5
Vibronic relaxation	$10^{-15} \sim 10^{-14}$	≃0.15
Lattice relaxation	$10^{-12} \sim 10^{-11}$	≃0.03

2.1.3 Excited States in Organic Solids

We here briefly deal with the process of light absorption and possible types of excitons in a lattice environment. Actually, excited states in organic semiconductors can be created through a large number of ways: e.g., light absorption, X-ray or electron irradiation, thermal or chemical excitation, as well as charge injection by an electric field. In general, an electron in the excited states of semiconductors tends to be coulombically coupled with its counter charge, leading to formation of a quasiparticle: the exciton. Two types of excitons, the Frenkel and charge-transfer exciton, are characteristic to organic solids. It is the charge-transfer exciton that plays a prominent role in photogeneration and recombination of charge carriers as we shall see in Section 2.4.

Certain new optical properties appear in solid-state organic semiconductors due to the collective molecular interaction, such as (1) displacement of emission and absorption bands relative to the isolated-state bands, (2) splitting of spectral lines with corresponding change in the polarization effects, and (3) variation of the selection rules and oscillator strength for optical transitions. On the other hand, the exciton binding energy found in an organic solid is usually large due to the low dielectric permittivity, and the weakness of the van der Waals interaction causes a localization of excitons on individual molecules of organic solids. Therefore, a specific shape of exciton bands in an absorption spectrum of organic solids usually does not significantly differ from the spectral shape of isolated molecules. For instance, Q- and B-bands resulting from a resonance interaction of excited states with intramolecular vibration modes, typical to phthalocyanine molecules, can be also observed similarly in the solid-state spectrum.

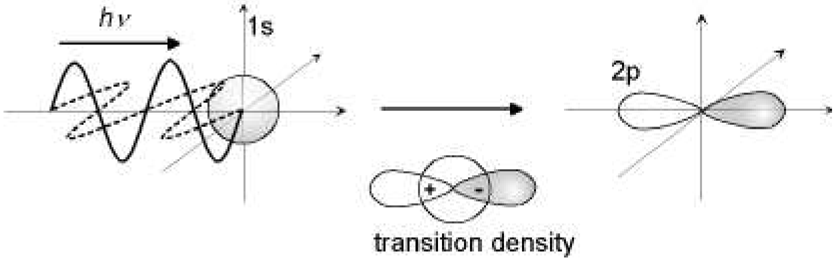

Figure 2.5: Orbital representation of a 1s hydrogen atom absorbing radiation causing a 1s → 2p transition. The corresponding transition density is largely dipolar in character and interacts with light as a dipole. (After [12])

Light Absorption

The most common process that causes an initial electronic excitation in organic materials is light absorption. Apart from the exciton formalism appropriate to organic solids, it is possible to describe the exchange of energy between light and molecules in a semiclassical fashion: It can be associated with an interaction of a field of the electromagnetic wave with an oscillating electric dipole moment set up in a molecule. The oscillating dipole moment has an amplitude and direction determined by a vector $\boldsymbol{M}$ known as the electric dipole transition moment. The transition density can be visualized as the amount of orbital overlap between the ground and excited state, which interacts with the corresponding electric component of the incident light. A schematic illustration of a transition density for the simplest case of an excitation from 1s to 2p orbitals is given in Fig. 2.5.

If we consider a lattice environment that can be approximated as an extended array of oriented but noninteracting molecules, the transition dipole moment $\boldsymbol{M}$ is given by a sum of dipoles over all electrons in the array:

$$\boldsymbol{M} = q \sum_i \boldsymbol{r}_i, \tag{2.6}$$

where q is the elementary charge and $\boldsymbol{r}_i$ is the position of the i-th electron in the coordinate. The transition amplitude for absorption is then described as

$$T_{i \to f} = \langle\, \Psi^{(i)}\, |\boldsymbol{M} \cdot \mathcal{E}_i|\, \Psi^{(f)} \rangle, \tag{2.7}$$

where $\mathcal{E}_i$ is the incident electric field at the corresponding electron. The transition moment integral $T_{i \to f}$ with regard to the initial state $\Psi^{(i)}$ and the final state $\Psi^{(f)}$ is related to the probability of light absorption, which expresses the charge displacement occurring during the passage from the ground state to excited state.

During the transition process, the energy is conserved if the incident radiation wavelength is much larger than the dimensions of the unit cell: In the long wavelength limit, only $\boldsymbol{k} = 0$ lattice states are accessible in dipole absorption. Standard optical absorption thus only probes the direct transitions, which are in general governed by spin selection rules. Transitions involving a change of spin are forbidden, and the transition probabilities are considerably

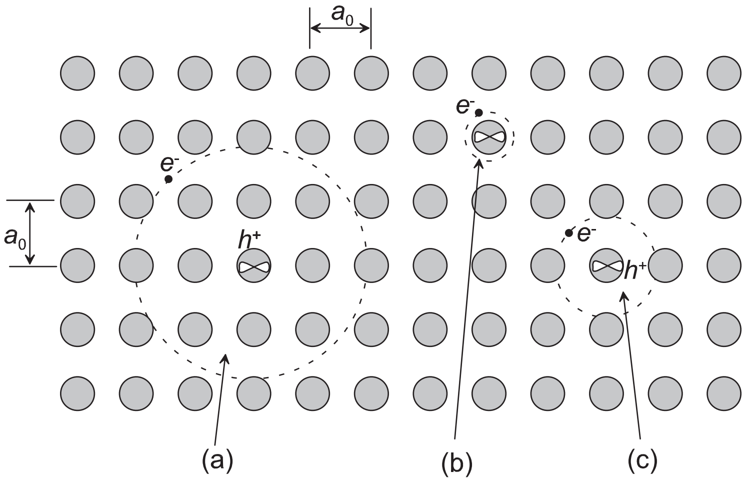

Figure 2.6: (a) Wannier exciton with a radius large in comparison with the lattice constant a_0. (b) Frenkel exciton with a radius small in comparison with the lattice constant. (c) CT exciton of, in this case, a nearest neighbour. (After [16])

low. However, the probability may be increased by spin-orbit coupling if, e.g., a heavy atom is present in the organic molecule.

Excitons

Mott and Wannier [13] first proposed an exciton model due to transition of an electron from the valence band to the conduction band: An electron-hole pair is formed with a large e–h distance (40–100 Å) and a correspondingly weak coulombic interaction. This is the *Wannier exciton*. The model can be applied whenever the dielectric constant of the material is sufficiently large. For organic materials with low dielectric constants and strong coulombic interactions, the Mott-Wannier model is in general not applicable.

Another model proposed by Frenkel [14] is an excitation of a molecule to a neutral state, which can be considered as a tightly bound e–h pair held together by a strong coulombic interaction. The *Frenkel exciton* is sometimes regarded as a correlated electron–hole pair located on the same molecular site and moves as a unit through the lattice. The radius of an exciton can be defined as the average separation of the electron from its corresponding hole. The Frenkel exciton is thus a small-radius exciton ($< 5\,\mathring{A}$). Excited states in organic solids can be classified as either neutral or ionized, and the ionized states are mainly created via the neutral states. Therefore, it can be considered that the neutral Frenkel exciton is the essential model for excited states in organic solids.

In addition to the neutral small-radius excitons with the electron–hole pair located on the same molecular site, there exist excited states in which the excited electron is transferred to a nearest or next-nearest neighbouring molecular site, but still remains correlated with its parent hole. The correlated electron–hole pairs that have a spatial extent of several lattice constants were termed "ionic states" by Lyons [15] in the 1950s, and are nowadays commonly called "*charge-transfer excitons*" (CT excitons).

The three types of exciton mentioned above are schematically depicted in Fig. 2.6. An expectation for the relation between energies of the Frenkel and CT exciton is that the binding energy of a CT exciton may be lowered from the initial Frenkel excited state by the amount

$$\Delta E_{bin} = \frac{q^2}{4\pi\epsilon r}, \tag{2.8}$$

where ϵ is the dielectric permittivity and r is the radius of the CT exciton. We shall treat this issue again in Section 2.4 in the context of geminate dissociation and recombination of e–h pairs.

To summarize the distinct molecular solid features from those of inorganic solids, a comparison of characteristics between anthracene and silicon crystals is listed in Table 2.2 together with the fundamental bulk parameters.

Table 2.2: Comparison of characteristic features between organic and inorganic solid states.

Example	Organic solids (Anthracene)	Inorganic solids (Crystalline silicon)
Interaction type	Van der Waals force	Covalent bonding
Interaction energy	10^{-3}–10^{-2} eV [11]	2–4 eV [11]
Elastic constant	$C_{11} \sim 8.5$–8.9×10^5 N/cm^3 [10]	$C_{11} \sim 1.7 \times 10^7$ N/cm^3 [17]
Static permittivity	$\epsilon \sim 3.6$ [10]	$\epsilon \sim 12$ [17]
Mean polarizability	$\bar{\alpha}_m \sim 25$–26 Å^3	—
Excitonic feature	Frenkel-type excitons CT-excitons	Wannier-type excitons

2.2 Electronic Transport in Organic Solids

Charge carrier mobilities found in organic devices are usually by far lower than that of conventional inorganic devices. The reason can be ascribed from two distinct aspects. If we assume a band transport mechanism in the molecular system, the narrow bandwidth of the van der Waals crystal should result in an increased effective mass of the charge carriers. On the other hand, if transport of charge carriers is governed by random processes, the mobility in the organic solid will be determined by the effectiveness of carrier hopping between the molecular sites. As seen in Section 2.1, a certain degree of charge localization intrinsically stems from the nature of organic solids. Besides that, the localization can be enhanced by structural and energetic disorder typically present in thin-film devices, regardless of the type of bonding interaction.

The critical issue, which of the above two cases should be taken into account, may depend on the degree of carrier localization under the respective molecular solid configuration. It is beyond our scope to present a comprehensive physical model applicable to both two extreme cases for organic solids. We here first present traditional models established for the coherent band transport, and then, we show more recently developed approaches to model the hopping transport, which have been successfully applied to organic films for particular cases.

2.2.1 Band Transport in Crystals

The theory for fundamental transport in a perfect crystal is well established and can be found in textbooks; e.g., in [17]. If the periodicity of a lattice structure permits the use of Bloch-like wavefunctions for describing a delocalized electron, the character of interaction forces between the lattice constituents determines the formation of the energy band structure as well as the bandwidth. We first introduce one of the standard methods well developed for inorganic metals and semiconductors to describe the band transport properties.

Tight-Binding Method

The tight-binding method is a kind of one-electron LCAO approximation. Let us suppose the ground state of an electron, $\varphi(\boldsymbol{r})$, moving in one of the periodic potentials of isolate atoms. If the influence of one atom on the other is small, we obtain an approximate wavefunction for one electron in the whole crystal by taking

$$\psi_{\boldsymbol{k}}(\boldsymbol{r}) = \sum_n C_{\boldsymbol{k}n} \varphi(|\boldsymbol{r} - \boldsymbol{a}_n|), \tag{2.9}$$

where $C_{\boldsymbol{k}n}$ is the coefficient and the sum is over all lattice points $\boldsymbol{a}_n$. The Bloch condition, $\psi_{\boldsymbol{k}}(\boldsymbol{r} + \boldsymbol{T}) = \mathrm{e}^{\mathrm{i}\boldsymbol{k}\cdot\boldsymbol{T}}\psi_{\boldsymbol{k}}(\boldsymbol{r})$, is satisfied assuming a translation vector $\boldsymbol{T}$ connecting two lattice points, which gives for a crystal of N atoms

$$\psi_{\boldsymbol{k}}(\boldsymbol{r}) = N^{-1/2} \sum_n \exp(\mathrm{i}\boldsymbol{k} \cdot \boldsymbol{a}_n) \varphi(|\boldsymbol{r} - \boldsymbol{a}_n|). \tag{2.10}$$

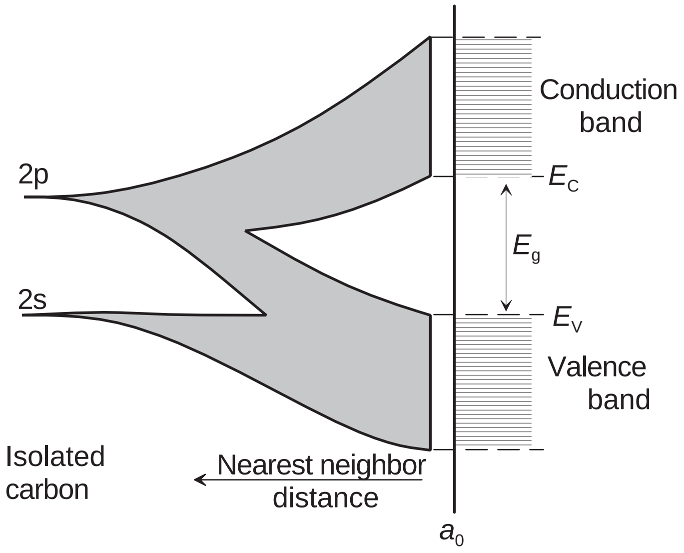

Figure 2.7: Formation of energy bands with decreasing distance of carbon atoms in a diamond crystal; E_g is the energy gap.

Similarly to the LCAO approach in the MO theory, the resonance integral γ represents the energy of interaction between the wavefunctions. For example, for a face-centered cubic lattice with the lattice constant a_0, the first order energies are given by

$$E_{\boldsymbol{k}} \simeq -\beta - 12\gamma + \gamma \cdot \boldsymbol{k}^2 \cdot a_0^2, \tag{2.11}$$

where β is the Coulomb integral. As the atoms are brought closer together, the electrons around each of the nuclei will begin to feel the potential caused by the other nuclei. This potential is a perturbation which lifts the degeneracy more and more effectively as the distance between the atoms is decreased. Each state of given quantum number of the free atom is spread in the crystal into a *band* of energies.

In the case of a covalent diamond crystal, the discrete atomic carbon levels 2s and 2p split and interpenetrate as the atoms approach each other. As interatomic distance becomes equal to the lattice parameter a_0, two bands of quasicontinuous states are formed: the valence band E_V, which is completely occupied by electrons, and the unoccupied conduction band E_C. Figure 2.7 shows the schematics of an energy band formation in a diamond crystal.

Bandwidth and Mobility

In the formalism of the tight-binding approach, the bandwidth B is considered to be proportional to the strength of the overlap interaction between neighbouring atoms. Assuming s-like wavefunctions, B can be associated with γ by an expression

$$B = 2Z_C\gamma, \tag{2.12}$$

where Z_C is the coordination number of the sites. Obviously, the weaker the overlap, the narrower is the energy band.

In a periodic potential well, the effective mass m^* is defined such that motion of an electron in the field follows the semiclassical kinetics

$$m^* = \frac{\hbar^2}{\partial^2 E_{\boldsymbol{k}} \partial \boldsymbol{k}^2}, \tag{2.13}$$

where $\hbar$ is the Planck constant. On the other hand, the mobility μ is in the Drude model given by

$$\mu = \frac{q\,\tau_0}{m^*}, \tag{2.14}$$

where q is the elementary charge, and τ_0 is the mean free time during which the field acts on the electron. From Eq. (2.11) and (2.12), it is possible to correlate the mobility of charge carriers with the resonance integral γ, hence also with the bandwidth B as

$$\mu = \frac{2\gamma\, a_0^2\, q\, \tau_0}{\hbar^2} \propto B. \tag{2.15}$$

Band Transport in Organic Crystals

Charge carriers in pure and perfect organic crystals are described within the framework of coherent Bloch waves. It is generally true that the presence of translational symmetry of a crystal lattice is a necessary condition for applying the band theory. However, this is not a sufficient condition; another important requirement is that the interaction of particles residing at the lattice sites is sufficiently strong. Because of the weak van der Waals bonding, calculations by the one-electron tight-binding method for organic crystals yield rather narrow bandwidths, typically on the order of 10–100 meV [10].

For a more decisive argument, Warta and Karl [1] showed that carrier transport in naphthalene crystals can be properly described by the standard band theory, taking into account an increase of the effective mass in the narrow band. Two possible causes of deviation from the pure band model are suggested: (1) onset of optical phonon emission due to an energy gain of charge carriers by field acceleration; (2) an increase of the effective mass in a nonparabolic band profile. For case (1), the kinetic energy of the charge carrier is consumed in generating the lowest optical phonon mode. The carrier velocity v is therefore limited by the phonon frequency ω_{phon} as $v \sim (\hbar\omega_{phon}/m^*)^{-1/2}$. Case (2) reflects a reasonable assumption that, in a narrow band, curvatures of $E_{\boldsymbol{k}}$ in the Brillouin zones are nonparabolic and flattened. According to Eq. (2.13), the effective mass then becomes large especially at higher energy states in the band. If the bandwidth is within several tenth of meV, the thermal energy of the charge carriers is sufficient to populate the energetically higher states. Therefore, an average value of the effective mass increases greatly with increasing temperature.

2.2.2 Localization

The bandwidths calculated by the one-electron model for organic crystals are actually not large enough to support the full applicability of the classical band theory to them. Rough estimations to check the validity of the band approximation can be made; firstly, the mean free path of charge carriers ℓ_0 must be larger than the lattice parameter a_0,

$$\ell_0 > a_0. \tag{2.16}$$

In a similar way, the mean free time τ_0 must be significantly longer than the carrier lifetime τ associated with the Heidelberg's principle

$$\tau_0 \gg \tau = \frac{\hbar}{B}, \tag{2.17}$$

where $\hbar$ is the Planck constant. The former condition (2.16) requires the carrier mobility to be at least $\sim 1\,\mathrm{cm^2/(Vs)}$ for typical molecular crystals [18, 19]. For most of the narrow band crystals, the estimated τ_0 according to Eq. (2.14) does not apparently fulfill the latter condition (2.17).

For such narrow bands, it can be expected that the carrier mobility is very small when the thermal energy $k_B T$ is comparable to the bandwidth; at sufficiently high temperatures, the mean free path eventually reduces to the lattice constant. Therefore, coherent electronic wavefunctions can be hardly expected: In other words, carriers are actually localized. Such localization excludes the traditional band concepts since the electron motion cannot be described by a wave vector $\boldsymbol{k}$ any longer.

Polaron Localization

For highly polarizable molecular solids, the effect of polarization by a charge carrier on neighbouring molecules is substantial. This is the electronic polaron effect. The carrier motion is then equivalent to a very strong scattering event occurring at each molecular site, and the motion is considered as randomized at each jump; i.e., each jump is independent of the preceding one. We can tentatively define for such cases a hopping time τ_h instead of the carrier lifetime in Eq. (2.17). The hopping time can be associated with the resonance integral γ_{ij} of the molecular interaction as

$$\tau_h = \frac{\hbar}{\gamma_{ij}}. \tag{2.18}$$

Thus, the duration of the charge carrier localization on a molecular site can be discussed in terms of τ_h, and is of the order of $10^{-14} \sim 10^{-13}\,\mathrm{s}$ for an anthracene-type crystal. On the other hand, the dipole relaxation time of electronic polarons is very short (10^{-16}–$10^{-15}\,\mathrm{s}$, see Table 2.1). Therefore, it can be expected that localization of the charge carrier on each

individual molecule naturally occurs in such organic crystals.
The vibronic relaxation of an organic crystal is of the same order as the hopping time τ_h. An interaction of a localized carrier with intramolecular vibronic modes may thus also take place. In contrast, the lattice relaxation time for anthracene-type crystals is usually of the order of 10^{-12} s and is greater than τ_h. In such a case, the localized charge carrier is not able to polarize the surrounding lattice during τ_h. However, as mentioned in Section 2.1, a presence of shallow traps may allow an interaction of the carrier with local lattice deformation.

Anderson Localization

Apart from the polaron effect, the charge localization mechanism of disorder origin has been the subject of intensive investigations. The influence of disorder on electron diffusion properties was first treated by Anderson [20], considering a random potential superimposed on a periodic potential. The Anderson model is also a tight-binding method with only one state per lattice site; random potential wells whose depths range within a value V_0 are considered. The effect of disorder on the density of states (DOS) is schematically shown in Fig. 2.8. In this model, disorder removes sharp band edges originated from the lattice periodicity, and a distributed DOS appears.
If the degree of random fluctuations V_0 approaches the bandwidth B, the mean free path ℓ of electrons is on the order of the lattice constant. This means that wavefunctions lose their

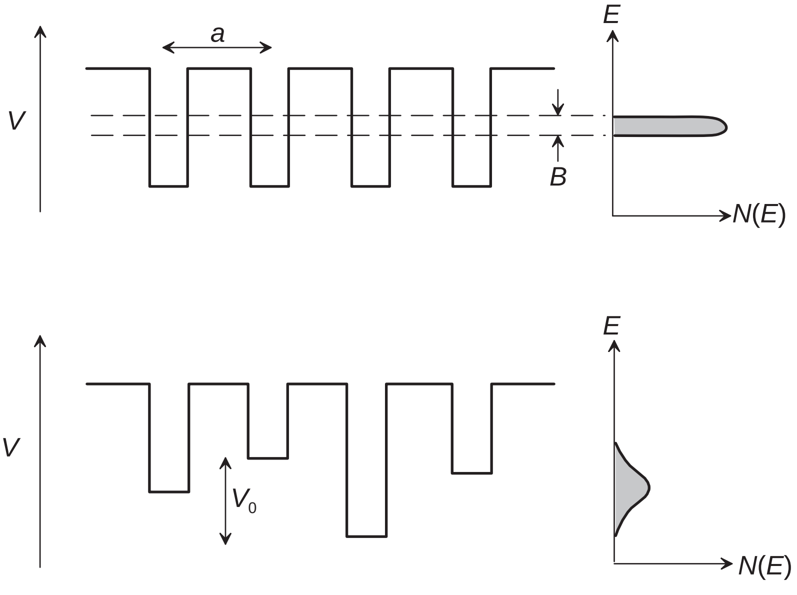

Figure 2.8: Schematic representation of the potential energy V in a system. The density of states $N(E)$ are also indicated. (a) A periodic potential with $V_0 = 0$. Electronic states are located within the bandwidth B which can be calculated by the tight-binding approximation. (b) Random potential wells with the finite value V_0. (After [21])

coherence when they move from a well to another. Such wavefunctions may have a form

$$\psi = \sum_n C_n \exp(\mathrm{i}\phi_n)\varphi(|\boldsymbol{r} - \boldsymbol{a}_n|), \tag{2.19}$$

where ϕ_n is a random phase, C_n is the coefficient, and $\boldsymbol{a}_n$ is the coordinate of the respective lattice site.

Localization of wavefunctions begins when V_0 becomes larger than B. This results in a decrease of the DOS at the center of the band, leading to a decrease of conductivity. Anderson predicted that for an electron moving in the potential of Fig. 2.8 (b), all states are localized when V_0/B exceeds a critical value, which was later shown to be of order 2 [22]. Here, *localization* means that the electron wavefunction does not resemble Eq. (2.19) any longer; then, *each* wavefunction describes an electron localized at a spatial point $\boldsymbol{r}_0$ as

$$\psi = \exp\{-\alpha_B|\boldsymbol{r} - \boldsymbol{r}_0|\} \sum_n C_n \exp(\mathrm{i}\phi_n)\varphi(|\boldsymbol{r} - \boldsymbol{r}_n|), \tag{2.20}$$

where α_B is considered as an inverse localization length, or the Bohr radius.

Mobility Edge

The extended band model was originally developed to explain the substantial electrical conductivity observed in inorganic amorphous metals and semiconductors. When V_0/B is less than the critical value, according to Mott [23], the states in the tails are in any case localized, but a sharp energy, E_μ—the mobility edge, separates the localized and extended states. Schematic representation of localized and extended states are shown in Fig. 2.9.

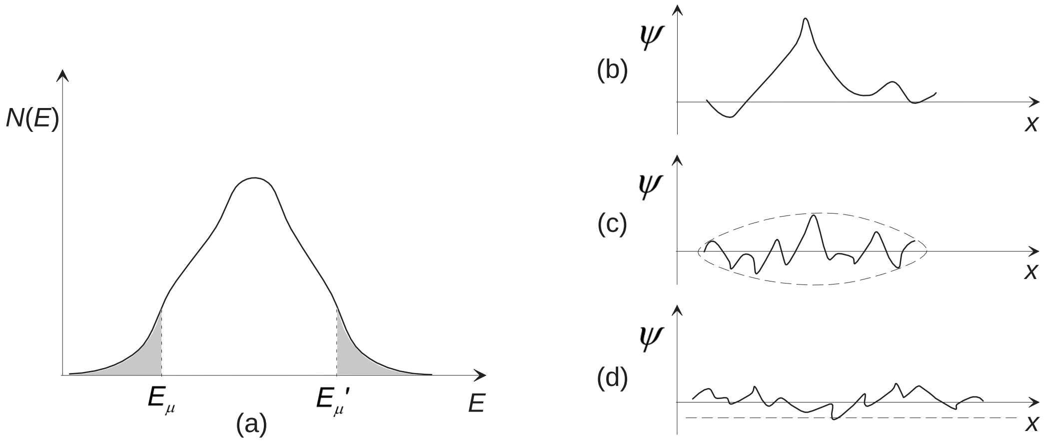

Figure 2.9: Left hand; (a) schematic representation of the density of states $N(E)$ as a function of energy E for a band of a disordered solid. The energies E_μ and E'_μ separate the regions of localized states (gray colored) from that of nonlocalized ones. Right hand; schematic representation of (b) a strongly localized, (c) weakly localized, and (d) extended wavefunction. After [21].

Let us consider two cases when the Fermi energy E_F can move across the mobility edge by a variation of the degree of disorder or the density of electrons. If E_F lies well above E_μ [but below E'_μ in Fig. 2.9 (a)], only a small scattering probability for electrons can be expected, and electrons can propagate with a mean-free path large compared with the distance between neighbouring atoms. On the other hand, when E_F lies below the mobility edge, i.e., when the states at the Fermi energy are localized, two conduction mechanisms can be expected: At low temperatures, conduction is realized by thermally activated hopping from a localized state to another; at high temperatures, electrons are excited into states above E_μ. Conductivity in the high-temperature regime therefore behaves as [24]

$$\sigma = \sigma_0 \exp\left(-\frac{E_\mu - E_F}{k_B T}\right), \tag{2.21}$$

where σ_0 is a prefactor. As we will see below, this Arrhenius transport behaviour is indeed commonly observed not only for inorganic amorphous films, but also for most of organic thin films within a limited temperature range.

2.2.3 Hopping Transport Models

For the treatment of real organic thin-film systems, an attempt to unify the *molecular* and *solid-state* aspects may bring complexity. The lack of long-range order often invalidates the use of elegant theories. Although no complete and comprehensive solution is available so far, there are indeed several transport models that show good agreement with measurements for some particular systems. Here, we present the most common transport models frequently quoted in literature.

Miller–Abrahams Hopping Rate

Calculation of carrier transition rate of phonon assisted tunnelling was first addressed by Miller and Abrahams [25] in order to study hopping conduction in disordered systems in the presence of a weak electric field. For this purpose, a random-resistor network was considered, in which the current flows through *bonds* connecting many *sites* (see Fig. 2.10). Owing to the large number of sites in actual systems (of order 10^{20}), a calculation of the hopping conductivity requires determination of the hopping probability with a configuration average procedure, while in ordered systems there is no need for averaging.

Assuming no correlation between occupation probabilities of different localized states, the average electron flow from a site i to j is written as

$$I_{ij}/q = \langle f_i(1 - f_j) w_{ij} \rangle, \tag{2.22}$$

with f_i being the occupation probability of the state i, and w_{ij} is the carrier transition rate from the occupied state i to the empty state j. The hopping process originates from

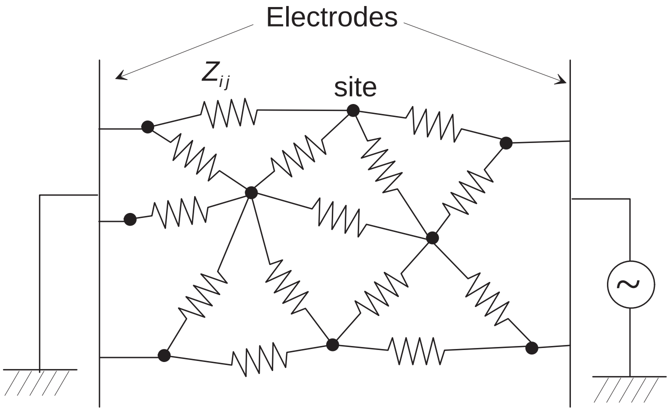

Figure 2.10: Schematic representation of the random-resistor network of Miller and Abrahams. Z_{ij} refers to the resistance between sites i and j. (After [21])

tunnelling events, and the tunnelling probability depends on the degree of wavefunction overlap. Assuming an s-like wavefunction, the resonance integral between the sites i and j is expected to have a form

$$\gamma_{ij} \propto \exp(-\alpha_B|\boldsymbol{R}_{ij}|), \tag{2.23}$$

where $\boldsymbol{R}$ is the relative coordinate between the two sites and α_B is the inverse localization length.

The electron transition rate from the site i of energy E_i to the site j of energy E_j can be formulated by means of a thermodynamic consideration. When k_BT is very small compared to $|E_j - E_i|$, it is then a good approximation to write

$$w_{ij} = w_0 \exp(-2\alpha_B|\boldsymbol{R}_{ij}|) \begin{cases} \exp\left(-\dfrac{E_j - E_i}{k_BT}\right) & \text{for } E_j > E_i \\ 1 & \text{for } E_j < E_i \end{cases} \tag{2.24}$$

where the prefactor w_0 is interpreted as the attempt-to-hop frequency which depends on the electron-phonon coupling strength, the phonon density of states, and the energetic difference between the sites. Utilizing Eq. (2.24) and the Fermi statics for the expression (2.22), the conductance is given by

$$Z_{ij}^{-1} \equiv \frac{I_{ij}}{k_BT} \simeq Z_0^{-1} \exp\left(-2\alpha_B|\boldsymbol{R}_{ij}| - \frac{|E_i - E_F| + |E_j - E_F| + |E_j - E_i|}{2k_BT}\right), \tag{2.25}$$

where Z_0^{-1} is a prefactor that is weakly dependent on the configuration ($\boldsymbol{R}_{ij}$ or $E_j - E_i$), and E_F is the Fermi energy. Here, k_BT is assumed to be small compared with all energies appeared. This expression, although first addressed by Ambegaokar [26], is often referred to as the “Miller–Abrahams conductance”.

Variable-Range Hopping

In the formalism developed by Mott [27], the hopping process is simplified by assuming that the dominant contribution to the hopping current occurs through states around the Fermi level within a range of $k_B T$, thereby eliminating the exact occupation probabilities of the states in Eq. (2.25).

According to Eq. (2.25), the conductivity can be dominated by nearest-neighbour hops if the temperature exponent is not important. At low temperatures, however, this exponent indeed plays an important role. Mott suggested that an electron may prefer to hop to a more remote site than to the nearest-neighbour one, in order to reduce the energy required for the hop: This is the so-called "variable-range hopping". For hops near the Fermi level, where $E_i < E_F$ and $E_j > E_F$ (or vice versa), Eq. (2.25) is reduced to

$$Z_{ij}^{-1} = Z_0^{-1} \exp\left(-2\alpha_B |\boldsymbol{R}_{ij}| - \frac{|E_i - E_j|}{k_B T}\right), \tag{2.26}$$

regardless of whether $E_i < E_j$ or $E_i > E_j$. In this situation, the conductivity is determined by hops giving rise to a minimal exponent in Eq. (2.26).

Assuming a nearly constant density of states $N(E)$ around the Fermi level, the minimal activation energy for the hops in the course of a distance R can be given by the number of available sites per unit energy:

$$\Delta E_{min} = \left[\frac{4\pi R^3}{3} N(E_F)\right]^{-1}. \tag{2.27}$$

Substitution of $|E_i - E_j|$ in Eq. (2.26) with ΔE_{min} leads to the exponent: $-2\alpha_B R - 3/[4\pi R^3 N(E_F) k_B T]$. The optimal hopping distance is obtained by minimizing the exponent as

$$R_{min} = \left[\frac{9}{8\pi N(E_F)\alpha_B k_B T}\right]^{1/4}. \tag{2.28}$$

Using Eqs. (2.26) and (2.28), Mott's law for three-dimensional variable-range hopping can be derived as

$$\sigma = \sigma_0 \exp\left(-\frac{T_0}{T}\right)^{1/4}, \text{ with } T_0 = 4\left(\frac{2}{9\pi}\right)\left\{\frac{\alpha_B^3}{k_B\ N(E_F)}\right\}. \tag{2.29}$$

Here, the prefactor σ_0 may be proportional to the phonon frequency, but cannot be determined without a more specific model of conduction.

Gaussian DOS Model

Pioneering modelling studies of the hopping mobility in disordered organic systems were carried out by Bässler [28]. In the model, both positional disorder (fluctuation in inter-site distance) and energetic disorder (fluctuation in site-energy) are considered. It is assumed that the polaronic effect can be neglected and that the hopping rate can be described by the Miller-Abrahams formalism (2.25). The energy distribution of localized states is assumed to be a Gaussian function

$$N_{gauss}(E) = \frac{N_t}{(2\pi\hat{\sigma})^2} \exp\left(-\frac{E^2}{2\hat{\sigma}^2}\right), \tag{2.30}$$

where N_t is the total density of sites, $\hat{\sigma}$ is the width of the Gaussian distribution, and the energy E is measured relative to the center of the DOS.

Monte Carlo simulations revealed that carriers (in this case electrons) with an arbitrary energy within the Gaussian DOS tend to relax into an equilibrium level $-\hat{\sigma}^2/k_BT$ below the center of the DOS distribution, therefore settling a level of dominant carrier transport at $-(5/9)\hat{\sigma}^2/k_BT$. This gives the temperature dependence of mobility as

$$\mu(T) \propto \exp\left[-\left(\frac{2\hat{\sigma}}{3k_BT}\right)^2\right]. \tag{2.31}$$

The hopping mobility in principle depends on also electric field since an average barrier height for energetic uphill jumps is reduced in a field. In the limit of high electric field and high degree of positional disorder, the carrier mobility is given by

$$\mu_{gauss} = \mu_0 \exp\left[-\left(\frac{2\hat{\sigma}}{3k_BT}\right)^2\right] \exp\left\{C\left[\left(\frac{\hat{\sigma}}{k_BT}\right)^2 - \Sigma^2\right]\sqrt{\mathcal{E}}\right\}, \tag{2.32}$$

where μ_0 is a prefactor, C is a constant that depends on the site spacing, Σ is the degree of positional disorder, and $\mathcal{E}$ is the electric field.

Percolation Approach

The variable range hopping model was further developed by Vissenberg and Matters [29] in order to explain the charge transport in polymer field-effect transistors (FETs). Their transport model considers filling of localized states with charge carriers, in contrast to Bässler's one particle model. The model predicts that the transport properties are determined by a distribution of Gaussian tail states, which is approximated by an exponential DOS:

$$N_{exp}(E) = \frac{N_t}{k_BT_0} \exp\left(\frac{E}{k_BT_0}\right), \tag{2.33}$$

where T_0 is the characteristic temperature that corresponds to the slope of the exponential tail. The density of charge carriers in the DOS at equilibrium is then given by the Fermi-Dirac occupation function $f(E, E_F, T)$ as

$$\delta N_t = \int_{-\infty}^{0} N(E) f(E, E_F, T) \mathrm{d}E, \tag{2.34}$$

with $\delta \in [0, 1]$ being a fraction of the occupancy.

Within the framework of the percolation theory, a system is viewed as a random resistor network. A critical percolation conductance of the system is given by

$$G_C = G_0 \exp(-s_C), \tag{2.35}$$

where G_0 is a prefactor, and the exponent s_C can be numerically calculated by making use of the Miller-Abrahams rate (2.25) and the DOS distribution (2.33).

The assumption in this model is that the Fermi level is located away from the characteristic tail width k_BT_0 ($-E_F \gg k_BT_0$). This condition is fulfilled when the carrier density is relatively low and $T < T_0$, meaning that most carriers occupy the lower sites in the DOS distribution. Another assumption is that the energy jump required for the critical percolation is large ($s_Ck_BT \gg k_BT_0$). Under such conditions, the tunnelling term in Eq. (2.25) cannot dominate the conduction at the bottom of the tail because of the low DOS. The dominant hopping occurs via an activated jump since there are much more available states at higher energy states.

Hopping in a strongly increasing DOS leads to a superlinear increase of conductivity with an increasing density of occupied states [29]:

$$\sigma \propto (\delta N_t)^{T_0/T}, \tag{2.36}$$

where δ is the fraction of occupied states, i.e., δN_t is the charge carrier density. An increase of carrier density leads to an increase in average energy of carriers due to the filling of lower localized states, and it further facilitates the activated jump of the carriers.

Also, the activated hopping in a distribution of DOS results in the conductivity with an Arrhenius-like temperature dependence

$$\sigma \sim \exp\left(-\frac{E_{act}}{k_BT}\right), \tag{2.37}$$

with an activation energy E_{act} weakly temperature dependent. Equation (2.37) has the same form as that in Eq. (2.21), indicating that an average over the random jumps can be effectively described by an activation of carriers from the Fermi level to a specific transport level E_μ.

Multiple Trapping and Release

The multiple trapping and release (MTR) model was originally developed to account for the low mobility in hydrogenated amorphous silicon devices. Assuming a distribution of band-tail states close to the extended states, the transport can be explained by thermal emission from the localized tail states.

In organic solids, a narrow band may be associated with a high concentration of trap levels. These traps may be deep traps located near the center of the gap, or shallow traps located close to the band. Transport then occurs in the band edge until recapture in the trap states occurs. This process occurs in a repeated fashion, the kinetics being mainly determined by a thermal emission rate ν. The rate depends exponentially on the energy difference between each localized state and the band edge; i.e., the activation energy E_{act}

$$\nu = \nu_0 \exp\left(-\frac{E_{act}}{k_BT}\right), \tag{2.38}$$

where ν_0 is an attempt-to-escape frequency in the respective phonon range.
The MTR model has been used more recently by Horowitz *et al.* [31] to explain the transport in sexithiophene FETs, assuming an exponential distribution of gap states. A filling of the gap states by gate induced charge carriers reduces the activation energy E_{act}, leading to an enhancement of the effective mobility. The effective mobility μ_{FE} is defined as

$$\mu_{FE} = \mu_0 \frac{n_f}{n_t + n_f}, \tag{2.39}$$

where μ_0 is the intrinsic mobility maximum; n_f and n_t are the free and trapped, respectively, carrier density. In their study, the Boltzmann approximation has been used to estimate the free-carrier density in the transport level; i.e., $E_{act} = E_\mu - E_F$. Therefore, the MTR model essentially resembles the Arrhenius equation (2.21), but differs in that μ_{FE} is introduced to evaluate the distributed trap site density. The MTR transport thus depends on the temperature and the details of the localized DOS distribution.

2.3 Theories for J–V Characteristics

This Section deals with the standard models for semiconductor devices to interpret the dark current–voltage (J–V) characteristics. Several types of devices and corresponding approaches for the idealized cases are briefly presented. A common prediction for the semiconductor diodes deduced form the theories is the exponential dependence of J on applied voltage and inverse temperature. Nonideality in the exponential dependence will be treated in the end of this Section referring to the *p*-*i*-*n* junction device.

2.3.1 Shockley Equation

When *n*- and *p*-type semiconductors are joined, free electrons in the *n*-side and free holes in the *p*-side begin to diffuse to the other side, leading to recombination of these carriers at the interface region. The positively ionized donors and the negatively ionized acceptors then start to create a built-in electric field $\partial V_{bi}/\partial x$ across the interface dipolar region; a thin depletion layer is formed. The field prevents further diffusion of carriers, and eventually, the built-in field and the diffusion process are balanced at equilibrium. This type of junction, the *p*-*n* junction, is the archetype of semiconductor diodes, which is the basis for modern electronic applications and for understanding of other semiconductor devices.
The basic theory for J–V characteristics of the *p*-*n* junction was established by Shockley [32]. The derivation of the ideal J–V characteristics are based on several assumptions. Firstly, an abrupt depletion layer is assumed: The built-in and applied voltages are supposed to drop only across the dipole layer with abrupt boundaries, and no field is assumed in the semiconductor layers outside the boundaries. Secondly, the Boltzmann approximation is used to describe the carrier concentrations: This approximation sufficiently holds for occupation of electronic states located several k_BT away from the Fermi level; e.g., for electrons in the conduction band and holes in the valence band of a nondegenerate system. It gives the following equations for majority carrier concentrations of electrons n_n and holes p_p in the *n*- and *p*-layer, respectively:

$$n_n = N_C \exp\left(-\frac{E_C - E_{Fn}}{k_BT}\right) \tag{2.40}$$

$$p_p = N_V \exp\left(-\frac{E_{Fp} - E_V}{k_BT}\right), \tag{2.41}$$

where N_C and N_V refer to the effective density of states of the conduction and valence band, respectively; E_{Fn} and E_{Fp} are the Fermi levels in the *n*- and *p*-layer, respectively; E_C and E_V are the energy levels of the conduction band edge and valence band edge, respectively.
At thermal equilibrium [see Fig. 2.11 (a)], the electrochemical potential of the *p*- and *n*-layer must be aligned; the built-in voltage V_{bi} can be estimated from the Fermi levels of the two layers as

$$qV_{bi} = E_{Fn} - E_{Fp}\,. \tag{2.42}$$

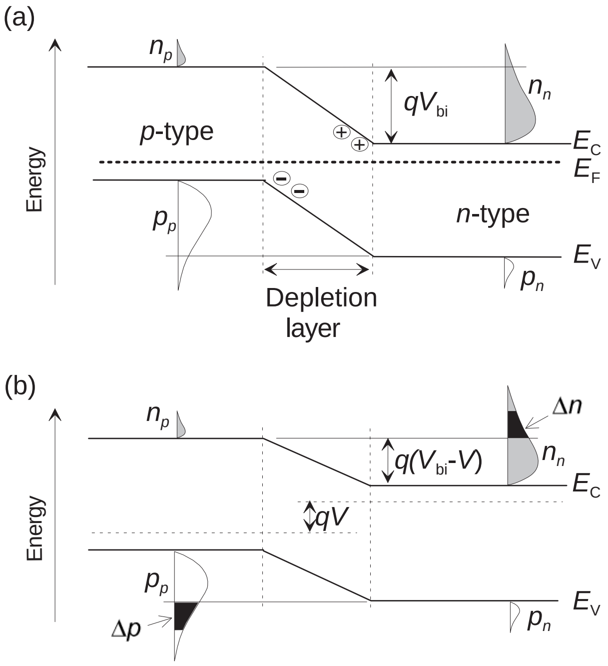

Figure 2.11: Energy-band diagram of a p-n junction; (a) thermal equilibrium condition, in which both layers have a common Fermi level E_F; (b) forward bias condition with an applied voltage V.

In this situation with no current flowing, a small fraction of n_n that can overcome the built-in potential to diffuse to p-side is virtually balanced with the minority carrier concentrations n_p of the p-layer. The same consideration holds for a fraction of p_p and the minority carrier concentration p_n. This gives the following equilibrium conditions:

$$n_p = n_n \exp\left(-\frac{qV_{bi}}{k_BT}\right) \tag{2.43}$$

$$p_n = p_p \exp\left(-\frac{qV_{bi}}{k_BT}\right). \tag{2.44}$$

With a forward bias V applied, the potential barrier height across the two layers is decreased to $q(V_{bi} - V)$. Consequently, excess carrier concentrations, Δn in the n-layer and Δp in the p-layer, actually diffuse to the other sides [see Fig. 2.11 (b)]; Δn and Δp are needed for a quasi balance in the nonequilibrium steady state. The electron concentration Δn can be obtained by replacing E_C in Eq. (2.40) by $E_C + q(V_{bi} - V)$, and with Eq. (2.43),

$$\begin{aligned}\Delta n &= N_C \exp\left(-\frac{E_C + qV_{bi} - qV - E_{Fn}}{k_BT}\right) - n_p \\ &= n_p \exp\left(\frac{qV}{k_BT}\right) - n_p = n_p\left[\exp\left(\frac{qV}{k_BT}\right) - 1\right].\end{aligned} \tag{2.45}$$

The hole concentration Δp is likewise given by Eq. (2.41) and Eq. (2.44) as

$$\Delta p = p_n\left[\exp\left(\frac{qV}{k_BT}\right) - 1\right]. \tag{2.46}$$

Now, we first consider the current density of holes in the n-layer. Since no electric field is present there, the current equation should consist of a diffusion current only:

$$J_p(x,t) = -qD_p \frac{\partial p(x,t)}{\partial x}, \tag{2.47}$$

where D_p refers to the diffusion coefficient of holes. Here, the hole concentration p depends on position and time. Assuming that no generation current exists, the continuity equation is in general given by

$$\begin{aligned} \frac{\partial p(x,t)}{\partial t} &= -\frac{1}{q} \cdot \frac{\partial J_p(x,t)}{\partial x} - \frac{p(x,t)-p_n}{\tau_p} \\ &= D_p \frac{\partial^2 p(x,t)}{\partial x^2} - \frac{p(x,t)-p_n}{\tau_p}, \end{aligned} \tag{2.48}$$

where τ_p is the hole lifetime in the n-layer. At steady state, no divergence exists and $p(x) - p_n = \mathit{\Delta} p(x)$. Since p_n does not depend on x, Eq. (2.48) can be rewritten as

$$\frac{\mathrm{d}^2 \mathit{\Delta} p(x)}{\mathrm{d}x^2} = \frac{\mathit{\Delta} p(x)}{\tau_p D_p} = \frac{\mathit{\Delta} p(x)}{L_p^2}, \tag{2.49}$$

where a definition for the diffusion length, $L_p \equiv (\tau_p D_p)^{1/2}$, is used for the last expression. The solution of Eq. (2.49) is easily given by the boundary condition (2.46) at the p–n interface where x is approximated as zero (see Fig. 2.12), and by an assumption $\mathit{\Delta} p(\infty) \simeq 0$,

$$\mathit{\Delta} p(x) = p_n \left[\exp\left(\frac{qV}{k_B T} \right) - 1 \right] \exp\left(\frac{-x}{L_p} \right). \tag{2.50}$$

Since $x > 0$ is assumed in the n-layer, Eq. (2.50) indicates an exponential decrease of the minority carrier concentration going away from the interface. The hole current density at $x = 0$ is then given by

$$J_p(0) = -qD_p \frac{\mathrm{d}\mathit{\Delta} p(x)}{\mathrm{d}x} = \frac{qD_p p_n}{L_p} \left[\exp\left(\frac{qV}{k_B T} \right) - 1 \right]. \tag{2.51}$$

The same consideration holds for diffusion of electrons in the p-layer; i.e.,

$$\frac{\mathrm{d}^2 \mathit{\Delta} n(x)}{\mathrm{d}x^2} = \frac{\mathit{\Delta} n(x)}{\tau_n D_n} = \frac{\mathit{\Delta} n(x)}{L_n^2}, \tag{2.52}$$

leading to the diffusion current density of electrons at $x = 0$;

$$J_n(0) = qD_n \frac{\mathrm{d}\mathit{\Delta} n(x)}{\mathrm{d}x} = \frac{qD_n n_p}{L_n} \left[\exp\left(\frac{qV}{k_B T} \right) - 1 \right], \tag{2.53}$$

with τ_n being the lifetime, D_n the diffusion coefficient, and L_n the diffusion length of electrons in the p-layer.

The total current density J is actually constant everywhere through the device, and no drift

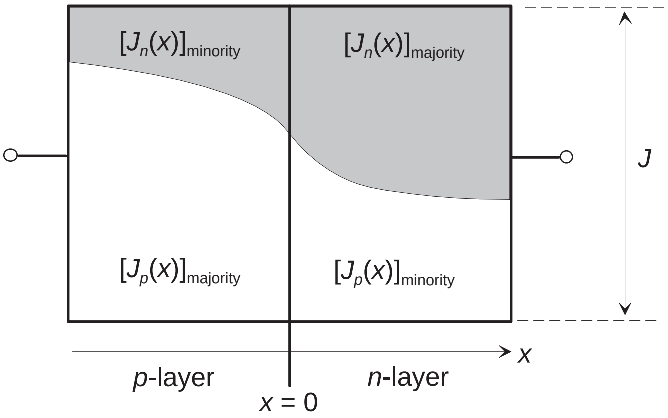

Figure 2.12: Schematic picture for the distribution of diffusion currents in a p–n junction.

current is assumed there. This means that, in each layer, J consists of two diffusion current densities of the majority and minority carriers. In the p-layer,

$$J = [J_p(x)]_{\text{majority}} + [J_n(x)]_{\text{minority}}, \tag{2.54}$$

and in the n-layer

$$J = [J_p(x)]_{\text{minority}} + [J_n(x)]_{\text{majority}}. \tag{2.55}$$

A schematic picture for Eq. (2.54) and Eq. (2.55) is drawn in Fig. 2.12.
Estimation of the majority carrier current is in fact rather difficult, therefore, J can be obtained only by summation of the minority current densities at $x = 0$; i.e., by the sum of Eq. (2.51) and Eq. (2.53):

$$\begin{aligned} J &= [J_p(0) + J_n(0)]_{\text{minority}} \\ &= q\left(\frac{D_p p_n}{L_p} + \frac{D_n n_p}{L_n}\right)\left[\exp\left(\frac{qV}{k_B T}\right) - 1\right] \qquad (2.56) \\ &\propto \exp\left(-\frac{E_C - E_V}{k_B T}\right)\left[\exp\left(\frac{qV}{k_B T}\right) - 1\right], \qquad (2.57) \end{aligned}$$

where the last expression (2.57) is due to Eqs. (2.40), (2.41), (2.43), and (2.44), and is true only when the parameters for electrons and holes, such as effective densities and diffusion coefficients, are both of the same order.

2.3.2 Schottky Junction

When a semiconductor makes contact with a metal, the metal work function Φ_{M} and the Fermi level E_F of the semiconductor are aligned at thermal equilibrium. In general, whether it is a Schottky contact or not depends on the the carrier conduction level of the semiconductor relative to Φ_{M}. Figure 3.10 shows the energy alignment on an n-type Schottky contact. As the isolated two materials (left picture in Fig. 3.10) come close together and

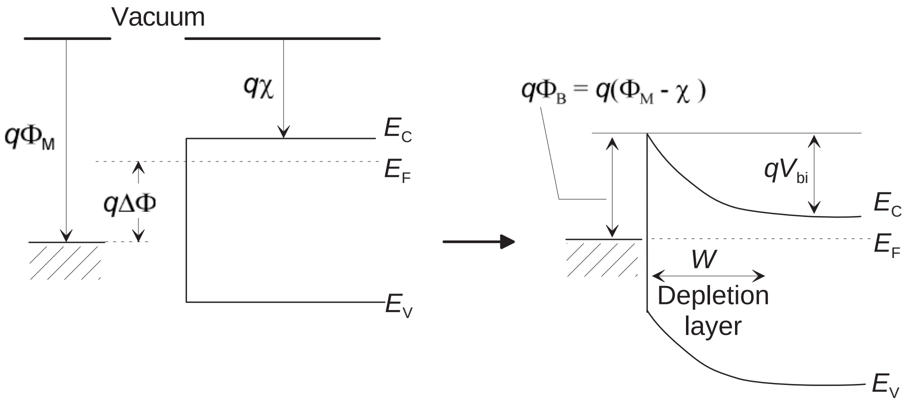

Figure 2.13: Energy-band diagram for formation of an ideal Schottky contact. $\Delta\Phi$ indeed equals V_{bi} as seen in Eq. (2.59).

make a contact (right picture in Fig. 3.10), a potential barrier is formed at the interface. The barrier hight Φ_B equals the potential difference between Φ_M and the electron affinity χ of the semiconductor so that

$$q\Phi_B = q(\Phi_M - \chi). \tag{2.58}$$

The built-in potential qV_{bi} measures the difference between $q\Phi_B$ and the conduction band edge E_C of the semiconductor. According to the energetics on the interface formation, qV_{bi} is equal to the difference between $q\Phi_M$ and E_F so that in the ideal case

$$qV_{bi} = q\Phi_M - E_F \equiv q\Delta\Phi. \tag{2.59}$$

The region of the semiconductor near the interface will be depleted after the contact; a depletion layer is formed in the similar manner to that of the *p*-*n* junction. The depletion width W ($x = 0$ at the interface and $W > 0$) can be estimated assuming a parabolic potential [33] as

$$U(x) = \frac{qN_D}{\epsilon}\left(Wx - \frac{1}{2}x^2\right) - q\Phi_B, \tag{2.60}$$

where N_D is the density of donor states that is to be fully ionized and ϵ is the permittivity of the semiconductor. By solving the Poisson equation, one obtains

$$W \approx \sqrt{\frac{2\epsilon}{qN_D}(V_{bi} - V)}, \tag{2.61}$$

where V is the applied bias voltage.

Note that if the Fermi energy E_F of the semiconductor is effectively close to E_C, or equivalently, if N_D is very large, W is very small. Therefore, tunnelling of electrons between the semiconductor and metal very efficiently occurs. In such a case, the contact is considered as virtually ohmic.

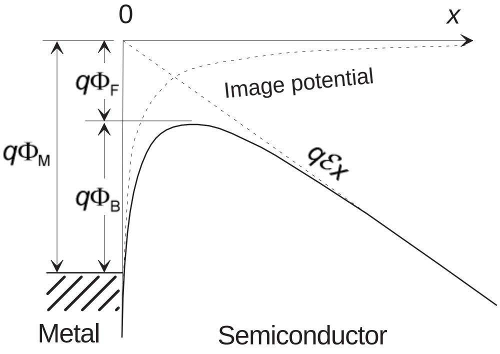

Figure 2.14: Energy-band diagram between a metal surface and vacuum.

Image Force Effect

The actual Schottky barrier height is usually lowered by the amount of potential energy induced by the image force effect when an electric field is applied at the metal/ semiconductor interface. Assuming that an electron is at a distance x (see Fig. 2.14) from the metal, a positive charge may be induced on the metal surface. The attractive force between the electron and the induced positive charge is equivalent to the force that would exist between the electron and an equal positive charge located at $-x$. This positive charge is referred to as the image charge. The image force F is given by

$$F = \frac{-q^2}{4\pi(2x)^2\epsilon_0} = \frac{-q^2}{16\pi\epsilon_0 x^2}, \tag{2.62}$$

where ϵ_0 is the permittivity of free space. When an external field $\mathcal{E}$ is applied, the total potential energy $E_{\text{total}}(x)$ is given by the sum

$$E_{\text{total}}(x) = \frac{q^2}{16\pi\epsilon_0 x^2} + q\mathcal{E}x. \tag{2.63}$$

The ideal Schottky barrier height is thus reduced by the image force factor Φ_{F}, which can be deduced from the condition $\mathrm{d}E_{\text{total}}/\mathrm{d}x = 0$, leading to a form

$$\Phi_{\text{F}} = \sqrt{\frac{q\mathcal{E}}{4\pi\epsilon_0}}. \tag{2.64}$$

Thermionic Emission Theory

Current transport in metal–semiconductor contacts is mainly due to the majority carriers. J–V characteristics of the Schottky junctions with high-mobility semiconductors can in most cases be described by the thermionic emission theory. The model supposes that all the energy for electrons in the conduction band is kinetic energy: The free-electron approximation is used.

The current density $J_{\mathrm{S}\to\mathrm{M}}$ from the semiconductor to the metal is given by density of electrons traversing in the x direction and having energy sufficient to overcome the potential barrier Φ_{B}:

$$J_{\mathrm{S}\to\mathrm{M}} = \int\limits_{E_F+q\Phi_{\mathrm{B}}}^{\infty} q v_x \mathrm{d}n, \tag{2.65}$$

where $E_F + q\Phi_{\mathrm{B}}$ is the minimum energy required for a thermionic emission into the metal, and v_x is the projection of the carrier velocity $\boldsymbol{v}$ along the transport direction. The free electron energy in the conduction band is given by

$$\frac{1}{2}m^*\boldsymbol{v}^2 = E - E_C, \tag{2.66}$$

and the minimum kinetic energy for the electron transport through a jump across the barrier is also given in terms of V_{bi}:

$$\frac{1}{2}m^* v_x^2 = q(V_{bi} - V), \tag{2.67}$$

where m^* is the effective electron mass of the semiconductor. The electron density in an incremental energy range is in general given by [33]

$$\begin{aligned} \mathrm{d}n &= N(E)f(E)dE \\ &= \frac{4\pi(2m^*)^{3/2}}{h^3}\sqrt{E-E_C}\exp\left(\frac{E_F-E}{k_BT}\right), \end{aligned} \tag{2.68}$$

where $N(E)$ is the density of states, $f(E)$ is the distribution function, and h is the Planck constant. Calculation of Eq. (2.65) then yields

$$J_{\mathrm{S}\to\mathrm{M}} = A^*T^2\exp\left(-\frac{q\Phi_{\mathrm{B}}}{k_BT}\right)\left[\exp\left(\frac{qV}{k_BT}\right)-1\right], \tag{2.69}$$

with A^* being the effective Richardson constant.

The theory involves the assumptions that (1) the barrier height $q\Phi_{\mathrm{B}}$ is much larger than k_BT, (2) thermal equilibrium is established at the plane that determines emission, and (3) the existence of a net current flow does not affect this equilibrium. Under these conditions, it is possible to superimpose two current fluxes—one from metal to semiconductor, the other from semiconductor to metal, each with a different quasi-Fermi energy. Because of these assumptions, the shape of the barrier profile is of no importance and the current flow depends solely on the barrier height.

Drift–Diffusion Theory

The drift–diffusion theory is applicable to low-mobility semiconductors since the effect of electron collisions within a depletion region is included in the derivation. The current in a depletion layer in general depends on electric field as well as carrier concentration gradient.

The local field $\partial U(x)/\partial x$ plays an important role in this model to determine the J–V characteristics, while it is not taken into account for the derivation of the Shockley equation.
Let us again consider a Schottky metal–semiconductor junction (n-type). The current density in the depletion layer consists of drift and diffusion currents:

$$J_d = q\left[-n(x)\,\mu_n\,\frac{\partial U(x)}{\partial x} + D_n\frac{\partial n(x)}{\partial x}\right], \tag{2.70}$$

where $n(x)$ is the local electron concentration and μ_n is the electron mobility. Equation (2.70) can be manipulated using the conventional Einstein relation

$$\frac{D_n}{\mu_n} = \frac{k_BT}{q}, \tag{2.71}$$

and using an electrochemical potential factor $\exp(qU/k_BT)$:

$$J_d = k_BT\mu_n\left[-\frac{q\,n(x)}{k_BT}\frac{\partial U(x)}{\partial x} + \frac{\partial n(x)}{\partial x}\right] \tag{2.72}$$

or

$$= k_BT\mu_n\frac{\partial}{\partial x}\left\{n(x)\exp\left[-\frac{qU(x)}{k_BT}\right]\right\}\exp\left[\frac{qU(x)}{k_BT}\right]. \tag{2.73}$$

Note that, if the variation of n exactly corresponds to $\exp(qU/k_BT)$, Eq. (2.72) leads to $J_d = 0$: It is at thermal equilibrium.
Under nonequilibrium steady state, the total current density is independent of x, therefore Eq. (2.73) can be integrated over the depletion layer [33] as

$$J_d\int_0^W \exp\left[-\frac{qU(x)}{k_BT}\right]\mathrm{d}x = k_BT\mu_n\left\{n(x)\exp\left[-\frac{qU(x)}{k_BT}\right]\right\}_0^W. \tag{2.74}$$

Integration of $\exp(-qU/k_BT)$ can be done by assuming the parabolic potential for $qU(x)$ [Eq. (2.60)]. The boundary conditions at the metal/ semiconductor interface ($x = 0$) and at the end of the depletion layer ($x = W$) can be obtained by the Boltzmann approximation

$$n(0) = N_C\exp\left(-\frac{q\Phi_\mathrm{B}}{k_BT}\right) \tag{2.75}$$

$$n(W) = N_C\exp\left(-\frac{E_C - E_F}{k_BT}\right). \tag{2.76}$$

For the final expression, it is convenient to define the electric field at the metal/ semiconductor interface, which is derived from Eq. (2.61) as

$$\mathcal{E}_0 = \sqrt{\frac{2q(V_{bi} - V)N_D}{\epsilon}}. \tag{2.77}$$

Equation (2.74) is eventually reduced to a simple form

$$J_d = q\mu_n\mathcal{E}_0N_C\exp\left(-\frac{q\Phi_\mathrm{B}}{k_BT}\right)\left[\exp\left(\frac{qV}{k_BT}\right) - 1\right]. \tag{2.78}$$

The exponent $-q\Phi_{\mathrm{B}}$ originates in the boundary condition of the electrochemical potential at the metal/ semiconductor interface.
The drift–diffusion theory is based on the assumptions also that the barrier height is much larger than $k_B T$, and that the carrier concentrations at the boundaries of the depletion layer ($x = 0$ and $x = W$) are determined from their equilibrium values. For the latter condition, the semiconductor must be nondegenerate.

2.3.3 Space Charge Limited Current

The method of space-charge-limited current (SCLC) is commonly known and can be used for studying the density of localized charge trap states in insulators or low-mobility semiconductors. Much work and the development of the physical interpretation of the SCLC mechanism were done by Rose and Lampert [34], and summarized by Nešpurek *et al.* [35] The necessary condition for single-carrier (either electron only or hole only) SCLC is that at least one of the two contacts of the sample must be ohmic. A characteristic feature of the single-carrier injection SCLC is a superlinear dependence of the current density J on the applied voltage V as well as on the thickness L of the sample.
We first consider the J–V characteristics for the simplest situation in an insulator with a negligible concentration of free carriers. The current density can be written as

$$J = \rho v = \frac{Q}{L} v, \tag{2.79}$$

where ρ is the injected charge concentration, v is the drift velocity, and Q is the total injected charge per unit area. No diffusion current is here assumed, which may exist at the vicinity of the contacts, but is in general not sizable compared to the drift current.
From the view point of electrostatics, the current injection is analogous to that in a capacitor with its geometric capacitance C_0; then, $Q = C_0 V = (\epsilon/L)V$, where ϵ is the permittivity of the material. More precisely, the charge distribution in an insulator is actually nonuniform, having larger concentration near the cathode-side. Therefore, the average distance of the injected charges from the anode is somewhat smaller than the nominal thickness L. However, the deviation of the real capacitance from the geometric one is usually negligibly small for an ideal insulator. For instance, the Poisson distribution with the drift field $\mathcal{E} \simeq V/L$ is

$$\frac{\partial \mathcal{E}(x)}{\partial x} = \frac{\rho(x)}{\epsilon} = \frac{qn(x)}{\epsilon}, \tag{2.80}$$

which yields merely 9/8 for the deviation factor, leading to an ideal SCLC current density

$$J \simeq \frac{C_0}{L} v = \frac{\epsilon V}{L^2} v \simeq (9/8)\epsilon\mu \frac{V^2}{L^3}, \tag{2.81}$$

where μ is the carrier mobility in the sample.

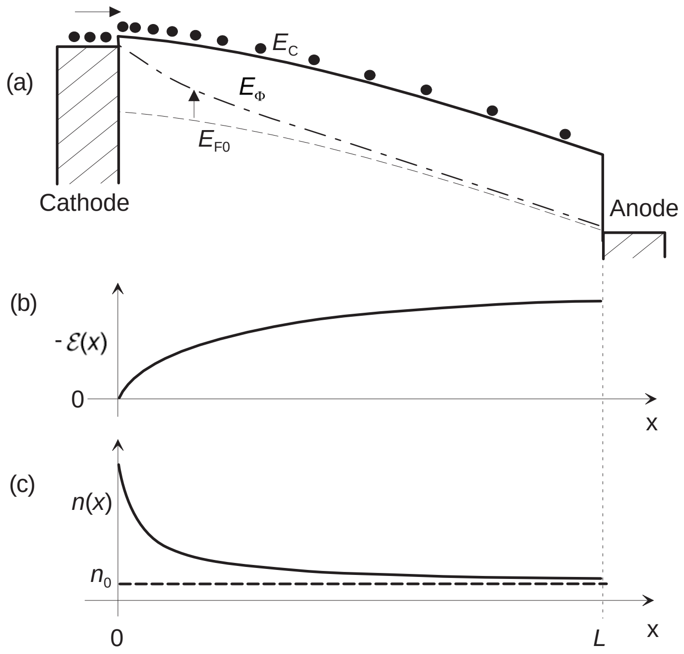

Figure 2.15: Space-charge-limited condition in a sample with thickness L. The electrons are injected from the cathode (ohmic contact), then drift towards the anode due to the applied bias. (a) Energy-band diagram. E_{F0} is the Fermi energy at thermal equilibrium and E_Φ is the quasi-Fermi level that is to be raised by the injected electron concentration. (b) Electric field profile $\mathcal{E}(x)$. (c) Electron concentration profile $n(x)$. n_0 is the thermal equilibrium concentration.

Next, we consider the case with a presence of free carrier concentration n_0 in thermal equilibrium. At low bias voltages, an ohmic current by the drift field,

$$J = qn_0\mu\frac{V}{L}, \tag{2.82}$$

will be observed. With increasing, but still small voltage, no significant departure from the ohmic current (2.82) can be expected: The ohmic law holds as far as the average injected electron concentration $\langle n\rangle$ is smaller than n_0. The onset of SCLC, i.e., the superlinear dependence of J on V, occurs when $\langle n\rangle$ becomes comparative to n_0. This condition is given with the threshold bias voltage V_{th} as

$$qn_0 = \frac{Q}{L} \simeq C_0\frac{V_{th}}{L}, \tag{2.83}$$

or,

$$V_{th} \simeq \frac{qn_0L^2}{\epsilon}. \tag{2.84}$$

A presence of carrier trapping sites in real semiconductors generally results in localization of the carriers and therefore a reduced current at low injection levels. On the other hand, the amount of injected charges, $Q \simeq C_0V$, is just a function of the bias voltage and does not change no matter the excess charges are to be free or trapped; i.e.,

$$C_0\frac{V}{L} \simeq q(n_f + n_t), \tag{2.85}$$

where n_f and n_t are the free and trapped, respectively, electron concentration. Thus, Eq. (2.81) is mended for the real case with a presence of trap sites:

$$J \simeq \theta \epsilon \mu \frac{V^2}{L^3}, \tag{2.86}$$

where $\theta = n_f/(n_f + n_t)$ is the fraction of carrier concentration contributing to the drift current. Considering shallow traps with a discrete level E_t and the quasi-Fermi level E_Φ lying below E_t, we can obtain forms for the carrier concentrations according to the Boltzmann approximation:

$$n_f = N_C \exp\left(-\frac{E_C - E_\Phi}{k_B T}\right) \tag{2.87}$$

$$n_t = N_t \exp\left(-\frac{E_t - E_\Phi}{k_B T}\right), \tag{2.88}$$

where N_C is the effective density of states in the conduction band, E_C is the energy of the conduction band edge, and N_t is the total trap concentration. When $n_f \ll n_t$ and $(E_t - E_\Phi)/k_B T > 1$, θ can be simply estimated as

$$\theta = \frac{N_C}{N_t} \exp\left(-\frac{E_C - E_t}{k_B T}\right). \tag{2.89}$$

In real thin-film samples, however, it is often difficult to observe a current J linearly depending on V^2 like in Eq. (2.86). The discrete trap model is thus in most cases insufficient to describe the SCLC characteristics in disordered systems. Apart from the discrete trap level model, one can, e.g., assume an exponential distribution of trap states with the characteristic energy $k_B T_0$, which has defined in Eq. (2.33) in Section 2.2. Equation (2.88) for the trapped electron concentration is then replaced by

$$n_t = N_t \exp\left(-\frac{E_C - E_\Phi}{k_B T_0}\right). \tag{2.90}$$

Combination of Eqs. (2.87) and (2.90) gives the SCLC current for the exponential trap approximation:

$$J \simeq q \mu N_C \left(\frac{\epsilon}{q N_t}\right)^m \frac{V^{(m+1)}}{L^{(2m+1)}}, \text{ with } m = \frac{T_0}{T}. \tag{2.91}$$

2.3.4 The p-i-n Junction

The *p-i-n* diode, often made of amorphous silicon, is derived from the *p-n* junction by inserting an undoped zone (i =“intrinsic”) of width W between the *p*- and *n*-layers. To give a physical interpretation of *J–V* characteristics in the *p-i-n* junctions, we can tentatively assume a uniform electric field in the *i*-layer. It may result in a diode equation similar to the

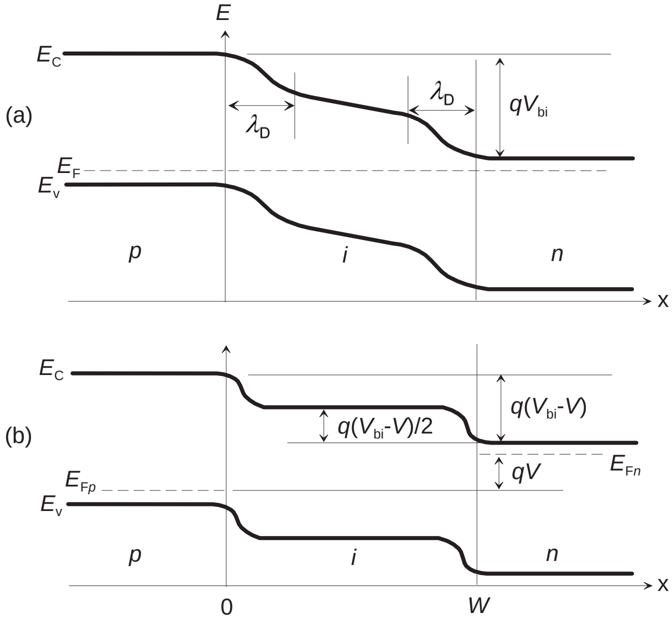

Figure 2.16: (a) Band profile in a *p*-*i*-*n* junction at thermal equilibrium with the Fermi level E_F. The Debye length λ_D is considered to be large, and in many cases indeed larger than the *i*-layer width W. (b) Band profile with a forward bias V; a flat band is formed in the *i*-layer. (After [37])

one derived by the drift–diffusion theory, but with an averaged field supported by the thick *i*-layer. However, such a simple assumption is, in many cases for amorphous silicon, inadequate for a detailed description of the device physics. For example, a realistic description of the amorphous silicon *p*-*i*-*n* characteristics can be obtained only if density of gap states and recombination are correctly treated [36].

Lacking an exact analytic solution of the band bending in the *i*-layer, we here attempt to qualitatively understand the energy scheme of the *p*-*i*-*n* junctions at equilibrium and under forward bias condition. Within the potential bending $U(x)$ of the intrinsic region, the electron and hole concentrations are given by

$$n(x) = n_i \exp\left[\frac{qU(x)}{k_B T}\right] \tag{2.92}$$

$$p(x) = n_i \exp\left[\frac{-qU(x)}{k_B T}\right], \tag{2.93}$$

where n_i denotes the intrinsic concentration of electrons and holes: At equilibrium, the total free carrier concentration amounts to $2n_i$.

For a small potential bending, we obtain the approximate Poisson equation

$$\frac{\mathrm{d}^2 U(x)}{\mathrm{d}x^2} = \frac{2n_i q^2}{\epsilon\, k_B T} U(x), \tag{2.94}$$

and its general solution leads to the Debye length

$$\lambda_D = \sqrt{\frac{\epsilon\, k_B T}{2n_i q^2}}\ . \tag{2.95}$$

This length characterizes the screening effect on the semiconductor, i.e., the rapid spatial attenuation by an applied electrostatic perturbation. The smaller the carrier concentration, the larger is the screening length. When there is no carrier injection, λ_D is generally large and the corresponding band bending is small. A schematic illustration of the band profile in thermal equilibrium is shown in Fig. 2.16 (a), where the widths of the depleted regions in the p- and n-layers are neglected.

If a large amount of carriers, much more than $2n_i$, are injected with a forward bias, the screening length in Eq. (2.95) becomes smaller. Accordingly, the space charges in the i-layer concentrate at the edges and most of the region in the i-layer becomes neutral in terms of chemical potential: $n = p$ and the electric field $\mathcal{E}$ is constant. By consideration of charge neutrality, an assumption of nonzero $\mathcal{E}$ turns out to be contradictory to the condition $n = p$; the band profile is actually flat at the center of i-layer [see Fig. 2.16 (b)]. Let us assume for simplicity that $p_p = n_n$ as the boundary conditions: Hole and electron concentrations in the p- and n-layer, respectively, are equal. Then, the injected two carrier concentrations in the i-layer are also equal, leading to

$$\begin{aligned} n = p &= n_n \exp\left[-\frac{q(V_{bi}-V)}{2k_BT}\right], \\ &= n_i \exp\left(\frac{qV}{2k_BT}\right). \end{aligned} \tag{2.96}$$

Note that, if there is no recombination in the i-layer and carriers eventually reach the other sides across the two potential slopes, n and p must be equivalent to $n_p + \Delta n(0)$ and $p_n + \Delta p(0)$, respectively, of the p-n diode. This leads to the ideal Shockley equation represented by Eqs. (2.56) and (2.57). However, when the current is due to recombination of injected carriers in the i-layer, we have instead

$$J \propto \exp\left(\frac{-E_g}{Ak_BT}\right)\left[\exp\left(\frac{qV}{Ak_BT}\right) - 1\right], \tag{2.97}$$

where $E_g = E_C - E_V$ is the energy gap and A is the ideality factor. The ideality factor in general varies within the range 1–2, and the value of 2 appears when the capture cross sections for electrons and holes are of the same order.

2.4 Optoelectronic Applications

A photovoltaic process begins with the generation of an excited state, and ends with the photon energy converted into electrical energy. On the other hand, excited states and concomitant charged pairs which have not been able to contribute to the electrical current are subject to recombination. Recombination via an intermediate charge-transfer exciton is a characteristic feature of organic solids. Such geminate pair recombination has great influence on the device performance.

Besides the photon absorption process, an excited state in organic solids can also be created by electrical charge injection in the course of electroluminescence. The radiative and nonradiative recombination of the excitons originated from the carrier injection can be treated by essentially the same physical mechanism as the one for the photo-induced excitons.

In this Section, we first present models for photogenaration and recombination processes typical to organic solids. Then, we also deal with physics of optoelectronic devices such as organic solar cells and organic light-emitting diodes.

2.4.1 Photogeneration and Recombination

When light is shone on a molecular solid, a photoelectric effect may be observed. Owing to the relatively low dielectric permittivity, light absorption in organic solids generally does not lead to creation of free electron–hole pairs, but excitons. In the discussion of excitonic properties, the multi-step autoionization model [11] is commonly recognized as the dominant mechanism of photogeneration in organic materials. A schematic diagram of the multi-step process is shown in Fig. 2.17.

The first step is photon absorption and formation of a neutral Frenkel exciton state. In the second step, autoionization of the excited molecular state takes place with quantum efficiency $\eta_0(h\nu)$, creating a positively charged parent ion and a hot electron with excess kinetic energy. In the third step, the hot quasifree electron undergoes intermolecular relaxation in order to lose its initial excess energy by means of inelastic scattering with phonons. Then, the electron becomes *thermalized* at a mean thermalization length r_{th} to form an intermediate charge-transfer (CT) state of bound charge carriers. Due to the thermalization process, the CT exciton gains a thermal energy K_{th} compared to the Frenkel exciton energy: In other words, the binding energy U_{CT} of the CT pair is reduced to a coulombic energy determined by r_{th}

$$-U_{\mathrm{Frenkel}} + K_{th} = -U_{\mathrm{CT}} = \frac{q^2}{4\pi\epsilon r_{th}}, \tag{2.98}$$

where $U_{Frenkel}$ is the Frenkel exciton binding energy, and ϵ is the permittivity of organic solid.

The above mentioned intermediate state is termed “charge pair (CP) state” in some literature (e.g., [11]) and is distinguished from the nonrelaxed CT state produced in direct optical transitions. We use the term “CT state” in this thesis to refer also to the pair produced in

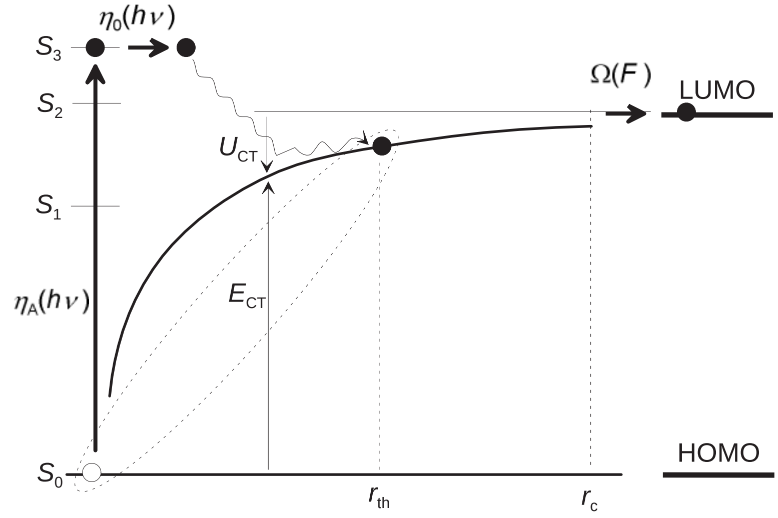

Figure 2.17: Schematic diagram of multi-step photogeneration model starting from neutral ground (S_0) and excited (S_1,S_2,S_3) states: η_0, autoionization efficiency; E_{CT}, CT state energy; U_{CT}, CT exciton binding energy; Ω, dissociation probability; r_{th}, thermalization length; r_c, critical capture radius.

the course of thermalization.

Field and Temperature Dependent Dissociation

At the final stage of photogeneration, free carriers are created via dissociation of the CT state with the probability Ω, which can be understood in the framework of a modified Onsager theory [38, 39]. The model allows one to describe the final dissociation stage of photogeneration in terms of thermal dissociation of the CT states as a result of Brownian diffusion of the charge carriers under the influence of mutual coulombic and external electric fields.

The multi-step model implies that either an additional activation energy or an external electric field is necessary for the dissociation of bound CT states. Such an activation energy of intrinsic photogeneration E_{act}^{ph} is determined by the coulombic binding energy U_{CT}; i.e., $E_{act}^{\mathrm{ph}} = -U_{\mathrm{CT}}$. A critical coulombic capture radius r_c is defined for an electron moving with thermal energy $k_B T$ so that

$$\frac{q^2}{4\pi\epsilon r_c} = k_B T. \tag{2.99}$$

Qualitatively, it can be understood that the dissociation of a CT state occurs when the activation energy is comparably low; i.e., $-U_{\mathrm{CT}} < k_B T$ or equivalently, $r_{th} > r_c$. Besides, it was shown by Silinsh *et al.* [40] that r_{th} is dependent not only on photon energy $h\nu$, but also on electric field $\mathcal{E}$. Thus, the CT state dissociation probability Ω is essentially a function of

$h\nu$, $\mathcal{E}$ and T. The Onsager model predicts that at a low field

$$\Omega(r_{th}, \mathcal{E}, T) \propto q\mathcal{E} \exp\left(-\frac{r_c}{r_{th}}\right) = q\mathcal{E} \exp\left(-\frac{q^2}{r_{th} 4\pi\epsilon k_B T}\right), \tag{2.100}$$

with the probability being a linear function of $\mathcal{E}$. At higher fields, however, it ceases to be linear and eventually saturates.

The quantum efficiency η_D of electron-hole dissociation in the multi-step photogeneration is then a product of two probabilities: CT state photogeneration quantum yield $\eta_0(h\nu)$ and CT state dissociation probability Ω, i.e.,

$$\eta_D(h\nu, \mathcal{E}, T) = \eta_0(h\nu) \cdot \Omega[r_{th}(h\nu, \mathcal{E}, T), \mathcal{E}, T]. \tag{2.101}$$

Recombination Process

The aforementioned multi-step generation process infers that an intermediate event may also exist during the reverse process of recombination. The probability of geminate recombination of a CT pair to form a Frenkel exciton, $(1-\Omega)$ is indeed substantial since the positive parent ion and the emitted electron in a CT state are still close to each other. The yield of free-carrier generation from the ionization events is thus generally very low.

On the other hand, the reversible step process also implies that recombination of a free electron and hole does not directly lead to loss of the charged particles: Instead, a bound CT state may be formed again. The probability of this intermediate process for bimolecular recombination, η_γ, can be determined by a recombination time τ_r of the carriers and a transit time τ_t for carrier collection at electrodes as

$$\eta_\gamma = \frac{\tau_t}{\tau_t + \tau_r}. \tag{2.102}$$

Then, the harvesting efficiency of free charge carriers, i.e., the internal quantum efficiency of photogenerated carriers at electrodes, is defined as

$$\eta_{int}^{\mathrm{ph}} = \eta_D(1 - \eta_\gamma). \tag{2.103}$$

The overall process of photoexcitation, carrier dissociation, and recombination is schematically summarized in Fig. 2.18.

Langevin Recombination

If oppositely charged free carriers are statistically independent of each other, the carrier recombination is a random process and is kinetically bimolecular. A requirement for this

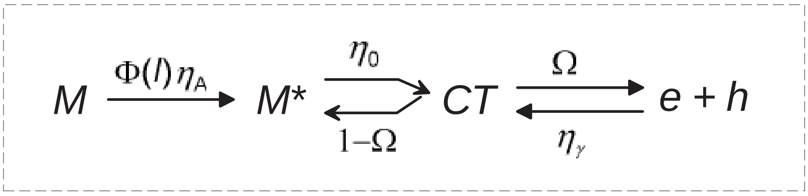

Figure 2.18: Schematic diagram of photoexcitation and dissociation process on a molecule termed "M": $\Phi(I)$, photon flux; η_A, absorption efficiency; η_0, CT state yield; Ω, dissociation probability; η_γ, bimolecular recombination rate.

type of recombination treated by Langevin [41] is that the mean free path ℓ of carriers be less than the capture radius of a carrier by the counter carriers. In most of the organic solids with $\epsilon \simeq 3.5$, the coulombic capture radius r_c is of the order of 100–200 Åat room temperature, while the scattering length (or the hopping distance) of carriers in organic films is, at most, several intermolecular distances. Therefore, usually $\ell < r_c$ and the Langevin requirement is satisfied.

A recombination rate R of carriers can be defined for electrons as $R = n/\tau_n$, where n is the nonequilibrium density of electrons and τ_n is the electron lifetime. The lifetime τ_n is in general determined by the average velocity of the electrons, $\langle v_n \rangle$, together with the capture cross section S_p and density p of the counter carriers (holes):

$$\frac{1}{\tau_n} = \langle v_n \rangle S_p \, p. \tag{2.104}$$

This leads to an expression for the rate

$$R = (np - n_0 p_0) \langle v_n \rangle S_p, \tag{2.105}$$

where n_0 and p_0 are the densities of electrons and holes, respectively, at thermal equilibrium. The Langevin model replaces the recombination coefficient $\langle v_n \rangle S_p$ in Eq. (2.105) by the so-called Langevin constant γ_{eh}. For pristine ambipolar materials, γ_{eh} is given by

$$\gamma_{eh} = \frac{q}{\epsilon}(\mu_e + \mu_h), \tag{2.106}$$

where μ_e and μ_h are the mobilities of electrons and holes, respectively. The bimolecular recombination rate can be then approximated as

$$R = \gamma_{eh}(np - n_0 p_0) \approx \frac{q n^2 (\mu_e + \mu_h)}{\epsilon}, \tag{2.107}$$

in which we assumed $n \simeq p$ and $np \gg n_0 p_0$ for the last expression. Thus, R is proportional to the square of carrier density.

2.4.2 Organic Solar Cells

Due to the potential for low-cost solar energy conversion, organic solar cells (OSCs) have been attracting considerable attention since a 0.95 % power efficient thin-film organic cell based with a single donor-acceptor heterojunction was reported by Tang in 1986 [42]. After a considerable period with few improvements over this demonstration, the pace of advances has been particulary rapid in the last decade, e.g., with developments in vacuum deposited small molecule based cells leading to solar power conversion efficiencies of up to 5.7 % [43] under AM1.5 G 100 mW/cm^2 solar illumination. Here, we will briefly summarize the definition of the solar parameters and efficiencies.

Solar Parameters and Efficiencies

Photovoltaic cells are characterized under standard illumination conditions (AM1.5 spectral illumination). A power conversion efficiency of a cell depends on three parameters: (1) the short-circuit current density J_{SC}, (2) the open-circuit voltage V_{OC}, and (3) the fill factor FF. These quantities are correlated in the form

$$FF = \frac{\max(JV)}{J_{SC}V_{OC}}, \tag{2.108}$$

where $\max(JV)$ represents the maximum power achievable in the J–V curve. The power conversion efficiency η_P is then defined as

$$\eta_P = \frac{FF\, J_{SC}V_{OC}}{P_{inc}}, \tag{2.109}$$

where P_{inc} is the incident optical power density; typically, the AM1.5 solar spectrum is used at an intensity of $P_{inc} = 100\,\mathrm{mW/cm^2}$.

An OSC external quantum efficiency $\eta_{ext}^{\mathrm{sol}}$ is defined as the number of carriers flowing in the external circuit per incident photon on the OSC, which is the product of (1) photon absorption efficiency η_A and (2) internal quantum efficiency $\eta_{int}^{\mathrm{sol}}$. An OSC internal quantum efficiency is defined as the ratio of the number of carriers collected at an electrode to the number of photons absorbed in the device, in the same manner as in Eq. (2.103).

For electrical detection, the tightly bound exciton must be dissociated into its constituents: electron and hole. Such a process can be induced by the built-in electric field, but the efficiency at electric fields typically found in organic devices ($\mathcal{E} \sim 10^6\,\mathrm{V/cm}$) is low ($\eta_D <$ 10 %).

Once an exciton dissociates into a free electron and hole, their collection efficiency, $(1-\eta_\gamma)$, at the opposing electrodes is high due to the built-in field present in most of OSC. In such a case, the external quantum efficiency can be written as

$$\begin{aligned} \eta_{ext}^{\mathrm{sol}} &= \eta_A \cdot \eta_{int}^{\mathrm{sol}} \\ &= \eta_A \cdot \eta_D (1-\eta_\gamma) \approx \eta_A \cdot \eta_D. \end{aligned} \tag{2.110}$$

For sufficiently thick (i.e., thicker than the optical absorption length, typically $\sim$ 1000 Å) organic layers, the majority of photons are absorbed, leading to an absorption efficiency

$\eta_A \sim 100\,\%$. This means that the efficiency of electron–hole dissociation, η_D, is the critical factor to determine the external quantum efficiency $\eta_{ext}^{\mathrm{sol}}$. The efficiencies and the solar parameters are connected to each other in the manner that the overlapping of $\eta_{ext}^{\mathrm{sol}}$ with the solar spectrum $S(\lambda)$ gives the short-circuit current density J_{SC}:

$$J_{SC} = q \int \eta_{ext}^{\mathrm{sol}}(\lambda) S(\lambda) \mathrm{d}\lambda. \tag{2.111}$$

2.4.3 Organic Light Emitting Diodes

Electroluminescence in organic device was discovered in the 1960s when blue light was emitted from crystalline anthracene with application of a high voltage of around 400 V. Modern technology in organic electroluminescence was first developed in 1987 by Tang and VanSlyke [44] using a hetero-structure: Two kinds of small molecular films with different charge transport properties were utilized. The structure enabled efficient recombination of carriers in the device, and the external quantum efficiency reached 1 %. Also, a brightness of more than 1000 cd/m^2 and a luminous power efficiency of 1.5 lm/W were achieved at about 10 V. This is nowadays referred to as the first realization of an organic light emitting diode (OLED).

Principles

Figure 2.19 shows the basic principle of the emission mechanism in a hetero-OLED structure. The thickness of the organic layers is usually of the order of a few hundred nanometers, sandwiched by an anode and a cathode. Holes are injected from the anode into the HOMO and electrons from the cathode into the LUMO of the respective organic layers. Drift currents of the carriers occur when a bias field is applied.

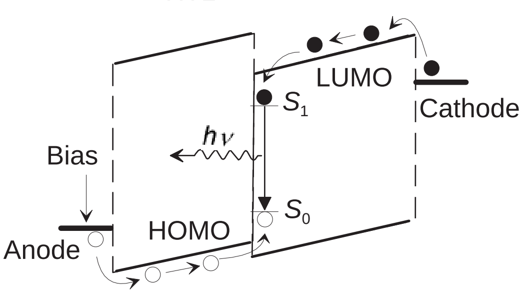

Figure 2.19: Schematic view of a basic OLED with double layer structure. Recombination of electrons (•) and holes (∘) effectively takes place in the ETL at the vicinity of the HTL. The recombination leads to the radiation $h\nu$ that corresponds with the energy of an exciton ($S_1 - S_0$).

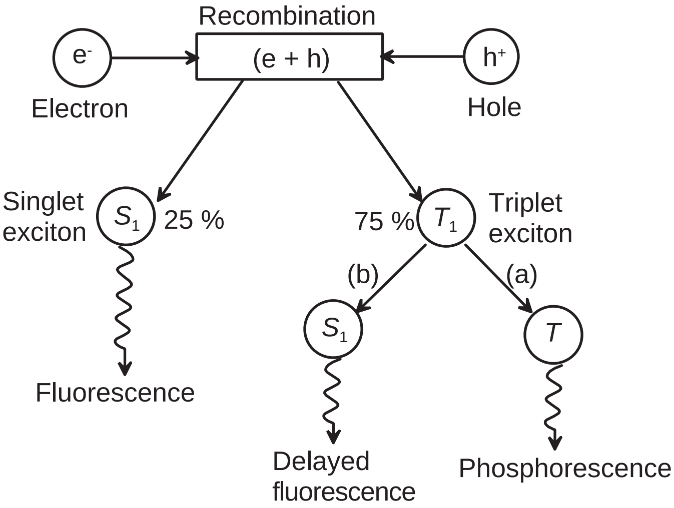

Figure 2.20: Simplified decay scheme of excitons after recombination of carriers. S_1 and T_1 denote singlet and triplet excitons, respectively. There are two processes for radiative decay of triplet excitons: (a) prompt phosphorescence; (b) delayed fluorescence via triplet-triplet annihilation. (After [16])

Some of the carriers may recombine at a molecular site via a CT pair state to form an molecular exciton, and eventually it may decay with an emission of the exciton energy. Other carriers which have not recombined will merely contribute to the DC current. In the hetero-structure, recombination of the carriers very efficiently takes place in the vicinity of the interface between the electron transport layer (ETL) and hole transport layer (HTL) due to a presence of carrier-blocking barriers.

Figure 2.20 shows the process of radiative decay through recombination of charge carriers. According to spin statics, the generation rate of singlet states to triplet states is 1:3 through the recombination. Therefore, as far as no strong perturbation takes place, at most only 25 % of electron–hole pairs can yield photons in a fluorescent emitter. However, it has been pointed out [16] that nearly 40 % of singlet exciton generation may be possible, considering a triplet-triplet collision process that leads to a new singlet exciton.

In contrast, an exciton generation efficiency of 75 % is in principle available in a phosphorescent emitter. Furthermore, if the transition of singlet–triplet states (intersystem crossing) efficiently takes place, nearly 100 % of e–h pairs are able to contribute to emission.

OLED Efficiencies

The commonly accepted definition for an external quantum efficiency of an OLED, η^{led}_{ext}, is the ratio of the number of photons emitted by the OLED into the viewing direction to the number of electrons injected. An internal quantum efficiency η^{led}_{int} is the ratio of the total number of photons generated within the structure to the number of electrons injected. The definitions imply that the internal and external efficiencies differ from each other by a fraction η_c of light coupled out of the structure into the viewing direction.

The internal quantum efficiency may be further divided with respect to three different loss mechanisms: the charge balance factor γ_{cb}, exciton generation rate η_r of spin statics, and quantum yield ϕ_p of radiative decay from the excited states; i.e.,

$$\begin{aligned} \eta_{ext}^{\mathrm{led}}(\lambda) &= \eta_{int}^{\mathrm{led}}(\lambda)\eta_c(\lambda) \\ &= \gamma_{cb}\,\eta_r\,\phi_p\,\eta_c\ . \end{aligned} \tag{2.112}$$

For display applications, $\eta_{ext}^{\mathrm{led}}$ is typically quoted independently of the emission wavelength. Given an emission spectrum $P(\lambda)$, which is normalized with respect to the OLED power, and an OLED current I_{led}, the external OLED quantum efficiency can be written as

$$\eta_{ext}^{\mathrm{led}} = \frac{q\int\lambda P(\lambda)\mathrm{d}\lambda}{h\,c\,\eta_c I_{led}}, \tag{2.113}$$

where h is the Planck constant and c is the speed of light. Here, the wavelength dependence of η_c is considered to be small.

The current efficiency η_L measured in candelas per ampere [cd/A] is convenient for quantifying the properties of an OLED for display applications. In many aspects, η_L is equivalent to $\eta_{ext}^{\mathrm{led}}$ with an exception that η_L weights all incident photons with respect the photopic response of the eye, while $\eta_{ext}^{\mathrm{led}}$ treats all photons equally. We can then define η_L as

$$\eta_L = \frac{A_d\,L_m}{I_{led}}, \tag{2.114}$$

where L_m is the luminance of the OLED in [cd/m^2], and A_d is the device area.

A more frequently used display efficiency unit is the luminous power efficiency η_{LP} in [lm/W], which is the ratio of luminous power L_p emitted in the forward direction to the total electric power required for driving the OLED at a particular voltage V; i.e., $\eta_{LP} = L_p/I_{led}V$. Following the spectrally resolved formalism in Eq. (2.113), we can calculate η_{LP} using the photopic response of the eye:

$$\eta_{LP} = \frac{\phi_0\int g(\lambda)P(\lambda)\mathrm{d}\lambda}{\eta_c I_{led} V}. \tag{2.115}$$

Here, the normalized photopic response is described by a spectral shape $g(\lambda)$ with the peak value $\phi_0 = 683\,\mathrm{lm/W}$ at $\lambda = 555\,\mathrm{nm}$.

3 Experimental

We introduce in the first Section of this Chapter characteristic features of molecular compounds used in this study. Special emphasis is placed on the features of strongly charge donating molecules, such as cationic acrydine-dyes or neutralized pyridyl-complexes. The application for electrical doping is the key to make these organic compounds very attractive subjects for fundamental investigations. The second Section is intended to discuss the principles of measurements which have been employed to elucidate the energetics and transport properties of doped organic thin films, including some mathematical expressions required for analysis of the experimental data.

3.1 Materials

3.1.1 Molecular Doping

An electrically doped organic thin film can be obtained by co-evaporation of matrix compounds and dopant molecules. Some of the small molecular dopants, such as benzoquinoline or quinodimethene derivatives [45], have been studied as acceptors in the 1960s, and tetrathiafulvalene derivatives as donors [46] in the 1980s. In the last decade, doping of organic semiconductors with more efficient dopants has been reported [3, 4], and the charge transport properties as well as the electronic structure in doped organic films have been investigated in detail, utilizing thermovoltage measurements [3, 47], field-effect measurements [30], and photoelectron spectroscopy [5, 48].

For a qualitative understanding, the energetics in the doped organic system can be discussed as follows: For p-type doping, it is necessary to find an acceptor molecule whose LUMO lies energetically near or below the HOMO of the organic semiconductor matrix; for n-type doping, the HOMO of the donor molecule has to be energetically near or above the LUMO of the matrix (see Fig. 3.1).

If the charge transfer between the dopant and matrix molecules is efficient, the situation can be viewed like the classical semiconductor analogy: The dopant molecules are ionized and a large carrier density is introduced in the matrix film. Exceptionally high dark conductivities up to 1 S/cm [49] can be thus found in organic films with an appropriate combination of matrix and dopant molecules.

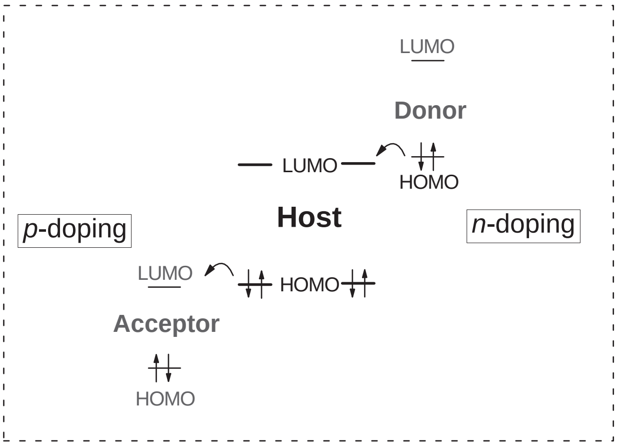

Figure 3.1: Conceptional view of charge transfer between matrix and dopant molecules.

Controlled Co-evaporation

Co-evaporation of organic materials is performed in a vacuum chamber. The matrix and dopant are evaporated from the individual crucibles by independently controlling the temperature of the both sources. The desired doping ratio of the dopant to the matrix can be achieved by monitoring the thickness monitors and by tuning the temperature of the sources. The schematics of the setup for co-evaporation is shown in Fig. 3.2.

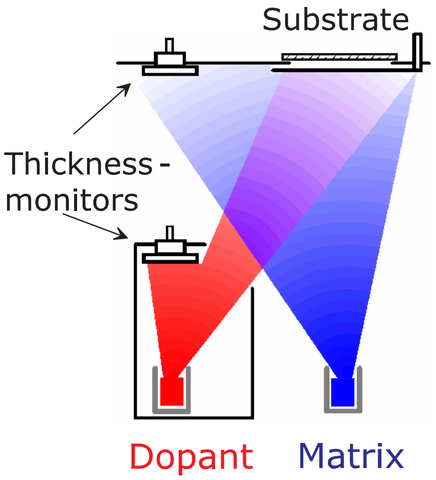

Figure 3.2: Setup for co-evaporation of matrix and dopant.

3.1.2 Matrices and Dopants

C_{60} and AOB

Fullerene C_{60} is a well-known organic semiconductor having an extended π-electron system with high electron affinity. Topologically, the C_{60} molecule is a truncated icosahedron, which consists of 12 pentagons and 20 hexagons, with a carbon atom at each of the identical vertices as shown in Fig. 3.3 (a). The truncated icosahedron has 120 symmetry operations, and is the closest to spherical among all regular polyhedra. C_{60} and other fullerenes are often utilized as an acceptor matrix for organic solar cells because of their excellent exciton and carrier transport properties. C_{60} films are also promising candidates for n-type organic thin-film transistors.

A pure C_{60} crystal has an fcc close-packed structure above $\sim 250\,\mathrm{K}$. Below that temperature, molecular rotations are partially locked. As a result, the unit lattice structure becomes a simple cubic [50]. Because of the large diameter ($\sim 7\,\text{Å}$) of C_{60} molecules, the interstitial cavities are large enough to accommodate several species of atoms without destroying the basic C_{60} lattice. Intercalation of C_{60} lattice with alkali and alkaline-earth metals was developed in the 1990s, leading to the observation of superconductivity [51].

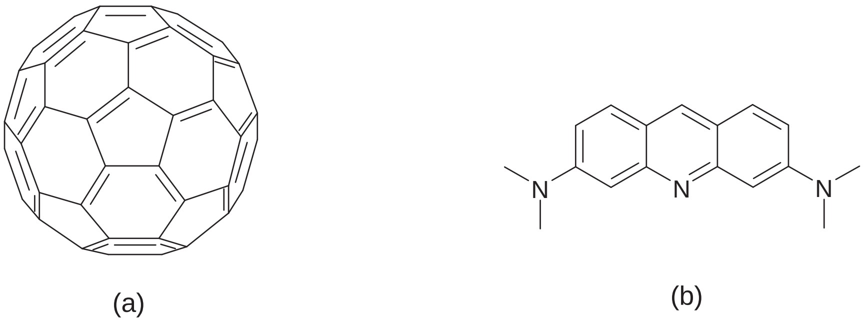

Figure 3.3: Chemical structure of (a) C_{60} and (b) AOB.

Acridine orange and its derivatives are well-known biologic and fluorescent dyes. Bernanose *et al.* [52] observed electroluminescence from crystalline acridine orange in the early 1950s with application of a high AC field.

Recently, Li *et al.* [8] have demonstrated that doping of C_{60} with 3,6-bis(dimethylamino)acridine [acridine orange base (AOB), see Fig. 3.3 (b)] enables efficient charge transfer from the donor to the matrix, strongly increasing the bulk conductivity in the films. By cyclic voltammograms, LUMO and HOMO energies of AOB can be roughly estimated as 3.5 and 5.5 eV, respectively, from the vacuum level. Since the LUMO energy of C_{60} is located around 3.8 eV [53], the electron transfer to the matrix should occur via an excited state of AOB followed by a protonation of the donor molecule, leading to a cationic product similar to AOBH^{+}. Thus, the excitation of AOB assisted by light or heating and the subsequent irreversible redox process are the necessary conditions for the efficient n-doping of C_{60}.

ZnPc

Phthalocyanines are macrocyclic compounds derived from four pyrrole-like subunits, in which at least one of the lone electron pairs residing on the central nitrogen atoms is shared with a metal ion acting as a Lewis acid. For these class of compounds, electronic transitions dominantly take place between ligand-centered orbitals. A number of intense peaks in the absorption spectrum appear in the UV and visible range, which are assigned to transitions between bonding and antibonding orbitals ($\pi\pi^*$ states). In addition, the nonbonding orbitals located in the azomethine groups bridging the pyrrole units give rise to $n\pi^*$ electronic transitions which are associated with the broadening of the absorption bands around 400 nm (B band) and 600–700 nm (Q band) [54].

Besides their outstanding optical properties, phthalocyanines have other beneficial features for film preparation. For instance, they are easily crystallized and sublimed; therefore, materials with high purity can be obtained. Also, they have a remarkable thermal and chemical stability. The complexes do not decompose until 900 °C in vacuum, and acids or bases usually do not affect them.

Figure 3.4 shows the molecular structure of zinc-phthalocyanine (ZnPc). In most metallophthalocyanines such as ZnPc, the macrocyclic ring is planar to within 0.3 Å. The symmetry of the molecule is approximately D_{4h}. An out-of-plane metal complex may be formed when the size of the metallic ion greatly exceeds the size of the cavity available, which may influence on the molecular stacking. Maennig *et al.* [30] have reported, using the electron diffraction method, that ZnPc thin films have an amorphous phase when the vapor deposition is performed at low temperature (-150 °C), whilst ZnPc films prepared at room temperature show a polycrystalline phase. The α-form of molecular stacking is known to be stable up to $\simeq$ 200 °C in phthalocyanines.

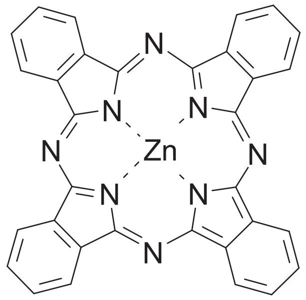

Figure 3.4: Chemical structure of ZnPc.

Pentacene

Aromatic hydrocarbons, especially linear polyacenes, have served as basic model compounds for research since relatively accurate theoretical predictions are available, provided by the physicochemical properties of each benzene ring.

Pentacene (see Fig. 3.5) is planar and has D_{2h} symmetry. The trigonal planar configuration is due to sp^2 hybridization of three of the valence electrons on a carbon atom, which are localized in the *xy* plane of the molecule. The forth of the carbon valence electrons retains $2p_z$, directed at right angle to the xy plane. Conjugation of the 22 coplanar $2p_z$ orbitals in a pentacene molecule then leads to delocalized π electron orbitals. These π orbitals play a dominant role in optical and electronic behaviour of pentacene.

Strong absorption in a pentacene film occurs in the visible range at wavelengths of 500–700 nm. An intense peak around 670 nm stems from the lowest singlet excitonic state [55]. Due to the outstanding photoconductivity, pentacene can be used for development of organic photovoltaic devices, often combined with C_{60} [56–58]. Furthermore, pentacene is a promising candidate for the use in organic thin-film transistors due to a high hole mobility up to $5.5\,\mathrm{cm}^2/(\mathrm{Vs})$ in thin films [59], and $35\,\mathrm{cm}^2/(\mathrm{Vs})$ in single crystals [60], which are indeed values comparable with those in amorphous silicon. Thus, pentacene is one of the most thoroughly investigated organic molecules with a large application potential.

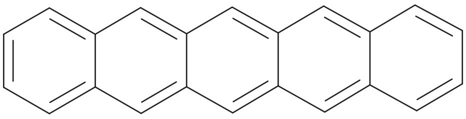

Figure 3.5: Chemical structure of pentacene.

F_4-TCNQ

The strong one-electron acceptor 7,7,8,8-tetracyanoquinodimethane (TCNQ) and its derivatives have been studied extensively because of the unique properties of their complexes. For example, a charge-transfer complex between TCNQ and an electron donor tetrathiafulvalene (TTF) exhibits a metallic conduction with exceptionally high conductivity, as well as superconductivity [61]. Furthermore, metal complexes of TCNQ show electrical bistability [62], which makes them potential candidates for memory devices.

More recently, the fluorinated TCNQ analog 2,3,5,6-tetrafluoro-tetracyano-quinodimethane (F_4-TCNQ), in which four hydrogens in the paraquinones are substituted by fluorines, has received considerable attention due to its application in molecular p-doping [3, 5, 48]. The peripheral electronegative fluorines make the electron affinity of F_4-TCNQ higher than that of TCNQ (4.5 eV), being around 4.9 eV from the vacuum level. The molecular structure of F_4-TCNQ is shown in Fig. 3.6.

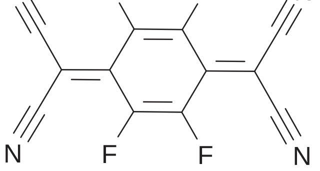

Figure 3.6: Chemical structure of F_4-TCNQ.

3.1.3 Ruthenium-Pyridyl Complexes

Ruthenium pyridyl complexes posses several interesting chemical and spectral properties. For example, their strong visible absorption, arising from a metal-to-ligand charge transfer transition, produces a long-lived triplet excited state. Also, in terms of redox chemistry, ruthenium is inert to any ligand substitution; therefore, various redox studies are possible both for the ground and excited states without the complexity of ligand exchange reactions. Thus, the ruthenium complexes have been widely used as a sensitizer for photoluminescence, and to study the photochemistry of other transition metals in aqueous solutions. Especially, ruthenium bipyridine and terpyridine complexes are known as the most efficient sensitizing dyes for the Grätzel solar cells [63, 64]. The latter is called "the black dye" (BD) due to the extensive absorbability ranging from the visible to near-infrared region up to 920 nm.

Oxidation States of Ruthenium Complex

Transition metals are unique in the sense that they can possess variable oxidation numbers. Various oxidized or reduced states are therefore in principle attainable employing electrochemical treatments. Figure 3.7 shows a formation of bis(2,2':6',2"-terpyridine)ruthenium(II), $[Ru(terpy)_2]^{2+}$, and its electron configuration by means of the valence bond theory. As seen in Fig. 3.8 (a), $Ru(terpy)_2$ is a complex whose six ligand nitrogens in the pyrydines surrounding the ionic metal ruthenium(II) form three chelate rings. The ligand nitrogen lone pairs in the complexant contribute twelve electrons to the molecular orbitals. The d_2sp_3-hybrid orbitals are responsible for the formation of the covalent bonds. A closed shell configuration is formed by the six electrons of Ru^{2+} and the twelve electrons from the donor complexant. Therefore, a cationic form $[Ru(terpy)_2]^{2+}$ is the most favorable valence state among a various oxidation numbers of the transition metal complex.

Bloom *et al.* [9] have demonstrated that the doubly reduced (starting from the common

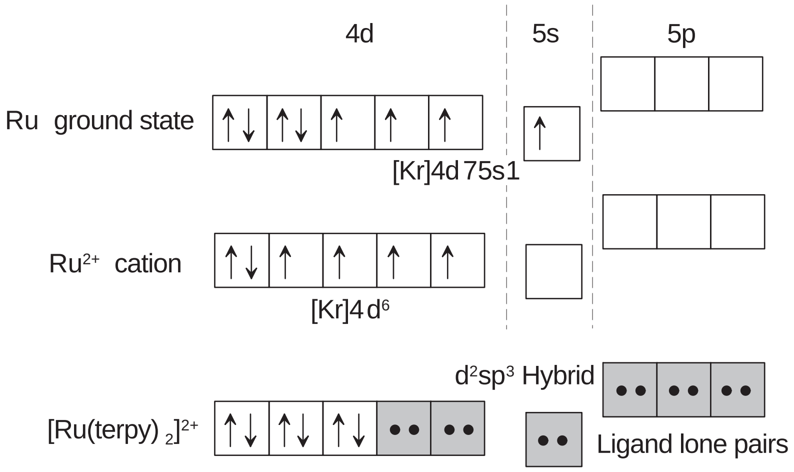

Figure 3.7: Formation of an electron configuration of $[Ru(terpy)_2]^{2+}$ via a cation Ru^{2+}.

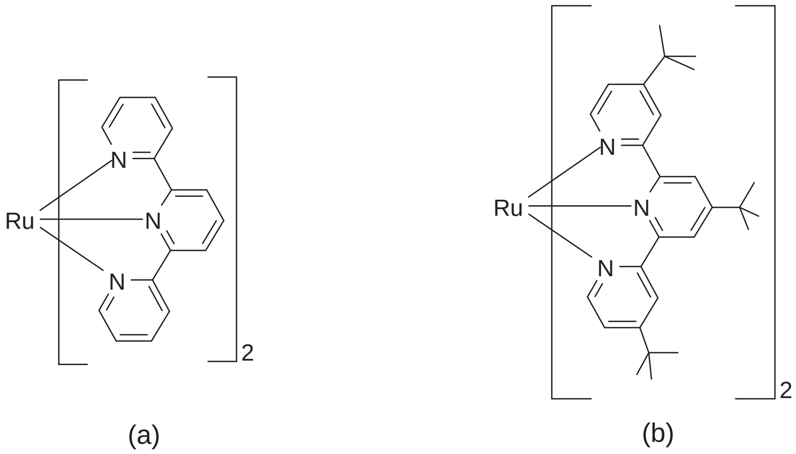

Figure 3.8: Chemical structure of (a) Ru(terpy)$_2$ and (b) Ru(t-but-trpy)$_2$.

2^+ oxidation state) form of [Ru(terpy)$_2$]^0 is a promising electron-injecting cathode material in organic light-emitting diodes because of the remarkably low oxidation potential ($1^+/0$) located around 3.3 eV from the vacuum level. Substitution of electron-donating alkyl groups for the methines leads to the terpyridine analog, bis(4,4',4"-tri-tert-butyl-2,2':6',2"-terpyridine)ruthenium [Ru(t-but-trpy)$_2$, see Fig. 3.8 (b)]. With this substitution, the oxidation potential is further lowered by 0.1–0.2 eV [65] from the unsubstituted one.

Molecular Orbitals of Ruthenium Complex

The aforementioned valence bond model is actually insufficient to correctly describe the molecular orbitals of the transition metal complexes. Due to perturbation by the nonspherical ligand field, the degeneracy of the d orbitals is lifted. Then, coupling of the d orbitals and ligand-orbitals should follow the symmetry-adopted linear combinations. For example, the field of bis-terpyridine ligands, which is of the type D_{2d} symmetry, only allows interaction for the donating π orbitals with the metal d_{z2} or p_z orbitals, and the d_{xy} orbital tends to be nonbonding [66]. Spectroscopically sizable charge transfer thus mainly takes place between the antibonding π^* orbitals and d_{zx} or d_{yz} orbitals.

The discussion about the exact molecular orbital structure is, however, beyond the scope of our study. We here only aim to reason why [Ru(terpy)$_2$]^0 and [Ru(t-but-trpy)$_2$]^0 are such strong donors. For this purpose, we refer to the systematic work in the 1980s by Morris and DeArmond *et al.* [67], in which the electronic and spectroscopic properties of electrochemically reduced transition metal complexes have been discussed.

Figure 3.9 shows the redox orbital scheme of tris(2,2'-bipyridine)ruthenium ([Ru(bpy)$_3$]^0) proposed by Morris *et al.* Although the symmetry perturbation of [Ru(bpy)$_3$]^0 ligands is of the type C_2, the picture can provide qualitative insight to understand the occupation of the reductant electrons in the metal-ligand orbitals. The reductant electrons of the ruthenium complexes occupy the π^* orbitals [see Fig. 3.9 (b)], which are supposed to be the LUMO of

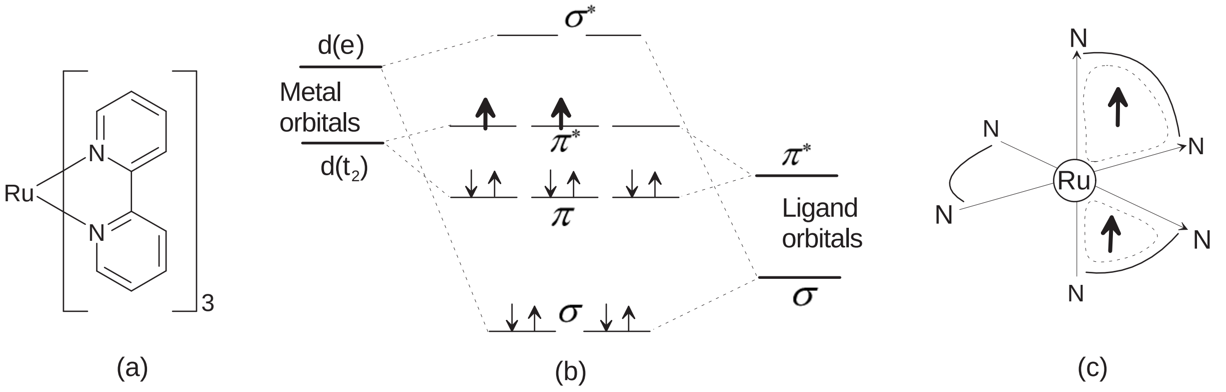

Figure 3.9: (a) Chemical structure of $[Ru(bpy)_3]^0$. (b) Suggested molecular orbital diagram. The configuration shown is the one expected for the doubly reduced reduction products where the π^* orbitals are single ring localized. (C) Model of singly localized reductant electrons on each chelate ring of $Ru(bpy)_3$ ligands. After [67].

the cationic complex ($[Ru(terpy)_2]^{2+}$ or $[Ru(bpy)_3]^{2+}$) in the ground state. This results in the remarkably low ionization potentials for the doubly reduced complexes.

It has been also addressed by means of electron spin resonance spectroscopy (ESR) that the reductant electrons seem to be located at a single chelate ring in the oligo-pyridine [Fig. 3.9 (c)], and that the ligand field is relatively weak so that the redox orbitals can still retain the character of *d* orbitals in the solid state. The spatial distributions of the reductant π^* orbitals are thus, in any event, located around the chelate rings near the center of the molecule, and are not spread over the entire molecular space.

3.2 Principles of Measurements

3.2.1 Field-Effect Measurements

MIS-diode

The field-effect transistor device is an extension of the metal–insulator–semiconductor (MIS) diode. The features of MIS-diodes are determined by the surface state of the semiconductor at the dielectric interface. We use in this Subsection the convention that the voltage V is positive when the metal is positively biased, and V is negative when the metal is negatively biased.

When an ideal MIS diode is biased, several cases occur at the interface. Here, we consider an n-type semiconductor. When a small negative voltage ($V < 0$) is applied to the metal plate, the valence band edge E_V of the semiconductor bends upward and comes closer to the Fermi level E_F, while the conduction band edge E_C is moved far from E_F. Since the majority carrier density depends on the energetic distance $E_C - E_F$, the band bending in this case causes a *depletion* of charge carriers in the region near the interface.

With a larger negative bias, further band bending results in a crossing of E_F over the intrinsic Fermi level E_i in the interface region, leading to a conducting path for minority carriers (holes): This is referred to as *inversion* [Fig. 3.10 (a)].

On the other hand, when a positive voltage is applied, the band profile bends downward in the interface region [Fig. 3.10 (b)]. Under such a condition, the number of electrons in the interface region is much larger than that of the bulk-equilibrium status: The majority carriers *accumulate* in the interface region.

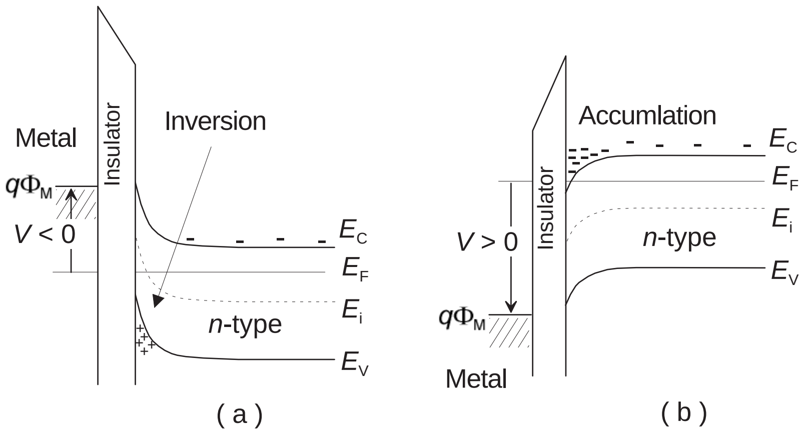

Figure 3.10: Energy-band diagram for an n-type MIS diode. (a) Inversion with a large negative bias. (b) Accumulation with a positive bias.

Theory of Field-Effect Transistors

The field-effect mobility μ_{FE} is a fundamental quantity for carrier transport in semiconductors. A measurement using the field-effect transistor (FET) gives the effective carrier mobility in the semiconductor. We first explain the principle of FET using the metal-oxide-semiconductor field-effect transistor (MOSFET) as an example. Figure 3.11 (a) shows the model of an n-channel MOSFET consisting of a p-type semiconductor. An electric field applied by a positive gate voltage V_G induces surface charges at the dielectric interface. As a result, an n-channel is formed due to inversion of the p-type semiconductor.

The electric field in a MOSFET comprises the normal component to the gate surface (trans-field) and the parallel component along the drain-source direction (channel field). When the gate voltage V_G is much larger than the drain voltage V_D, the FET characteristics can be reduced to a 1-D problem. The drain-source current I_D is then approximated as [33]

$$I_D \simeq \frac{Z}{L}\mu_{FE}C_i\left[(V_G - V_{th})V_D - \frac{V_D^2}{2}\right], \tag{3.1}$$

where Z is the width of the drain-source contacts, L is the channel length, and C_i is the capacitance per unit area of the insulator. The threshold voltage V_{th} is required to switch-on the trans-characteristics, i.e., to make the inversion channel.

When V_D is considerably higher, a large depletion region will be formed near the drain electrode in the semiconductor layer. An increase of the depletion region causes a gradient of the trans-field through the channel, and finally, the channel is pinched off: I_D becomes saturated and independent of V_D. The squared term V_D^2 in Eq. (3.1) describes the saturation of drain-source current.

On the other hand, for a small V_D, the first term in the square brackets dominates in Eq. (3.1): I_D increases linearly with respect to V_D and V_G. In this linear regime, the channel

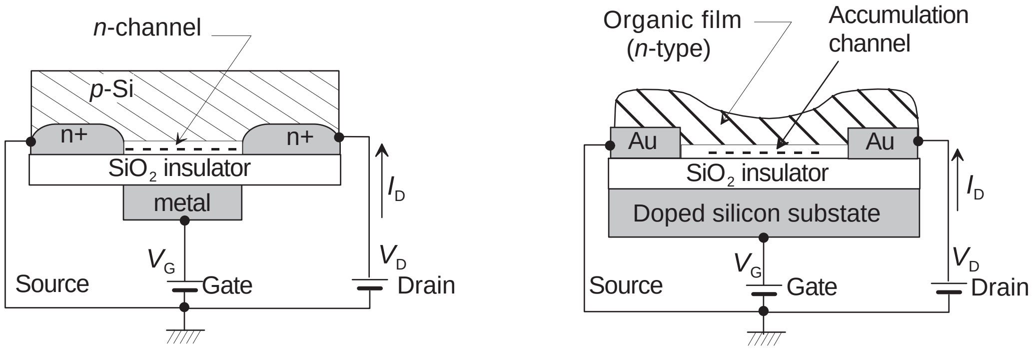

(a) (b)

Figure 3.11: Schematic view of FET structures. (a) A typical n-channel MOSFET. (b) A bottom-contact OFET structure used in this study.

conductance g_D and the trans-conductance g_m are given by

$$g_D \equiv \left.\frac{\partial I_D}{\partial V_D}\right|_{V_G=\text{const}} = \frac{Z}{L}\mu_{FE}C_i(V_G - V_{th}) \ , \tag{3.2}$$

$$g_m \equiv \left.\frac{\partial I_D}{\partial V_G}\right|_{V_D=\text{const}} = \frac{Z}{L}\mu_{FE}C_iV_D \ . \tag{3.3}$$

Thus, the mobility μ_{FE} can be calculated from the slope of the I_D–V_G and I_D–V_D characteristics.

OFET

Figure 3.11 (b) shows the schematic view of an organic field-effect transistor (OFET) sample employed in our measurements, in which a highly doped silicon substrate is utilized for the gate contact. In contrast to the n-channel MOSFET, the organic thin film is an n-type semiconductor. Here, the n-channel conduction occurs due to an accumulation of majority carriers (electrons) with a positive voltage applied [see Fig. 3.10 (b)].
If the bulk conductivity of the organic layer is high enough, i.e., when it is n-doped, the potential bending at the vicinity of the dielectric interface is small and sharp since the Fermi energy is close to the charge transport level. Therefore, the accumulation channel should immediately form as soon as a small gate bias is applied. A consideration of the flat-band condition is thus of no significance. Similarly, the drain-source current I_D is not controlled by depletion: Injection of charge carriers from the metal contacts is so efficient that I_D–V_D characteristics are virtually ohmic. The n-doped OFET characteristics have thus no threshold, and do not exhibit saturation. For evaluation of μ_{FE} under these conditions, Eqs. (3.1), (3.2), and (3.3) can be combined and simplified, yielding a form

$$\mu_{FE} = \frac{L}{Z\,C_i}\frac{\partial I_D}{\partial V_G \partial V_D} \, . \tag{3.4}$$

3.2.2 Seebeck Measurements

The thermoelectric power (Seebeck coefficient) S_Q is the average entropy per unit charge q transported along with a charge carrier. In terms of thermodynamics, a change in entropy will be introduced to a system when a charge carrier is added to it. This amount of entropy is transported with the carrier as it passes through the material. For a free carrier, the Seebeck coefficient is associated with energy E of the carrier as

$$S_Q(E) = \frac{|E - \xi|}{qT}, \tag{3.5}$$

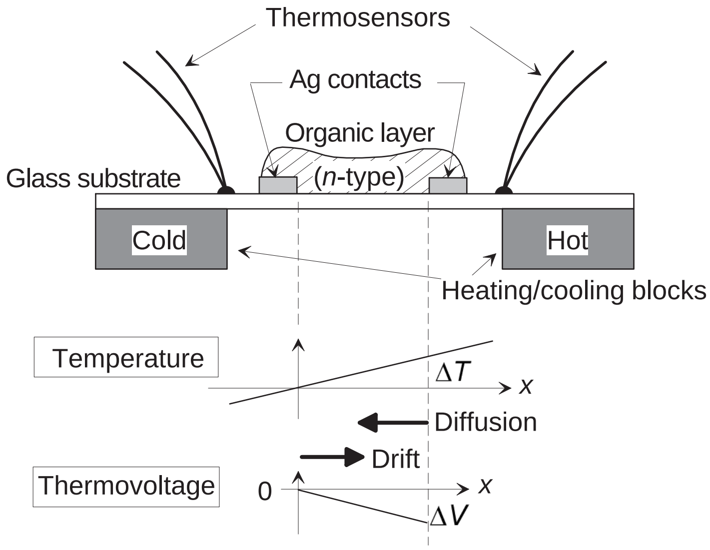

Figure 3.12: Schematic view of a Seebeck measurement sample used in this study. The organic layer is in this case of n-type. The temperature differential ΔT is obtained assuming a linear temperature gradient on the substrate. Note that for p-type semiconductors the thermovoltage is positive.

where T is the temperature and ξ is the chemical potential. Each carrier contributes to S_Q in proportion to its relative contribution to the total conduction. The net Seebeck coefficient is then an average of this quantity weighted by the differential conductivity $\sigma(E)$. The weighting factor for carriers in the interval $\mathrm{d}E$ at energy E is $\sigma(E)\mathrm{d}E/\sigma$, yielding [68]

$$S_Q = \frac{\int S_Q(E)\sigma(E)\mathrm{d}E}{\int \sigma(E)\mathrm{d}E}. \tag{3.6}$$

Figure 3.12 shows a typical Seebeck measurement sample employed in this study. The principle of the Seebeck measurement can be also qualitatively explained in terms of the conventional drift–diffusion model. Let us imagine a semiconductor film with a temperature gradient along the x direction in Fig. 3.12. From a semiclassical point of view, charge carriers at the hot side gain kinetic energy, or for nondegenerate semiconductors, a positional gradient of the carrier density will be introduced. The charge carriers then diffuse from the hot end to the cold end, and the carriers eventually concentrate on the cold end. This unbalanced charge density creates a built-in electric field inside the sample. Equilibrium is reached when the drift current generated by the field cancels the flow due to the thermal diffusion.

In practice, the Seebeck coefficient S_Q is obtained by measuring the open-circuit voltage ΔV developed across the material between two contacts, with respect to an imposed temperature differential ΔT:

$$S_Q = \frac{\Delta V}{\Delta T}. \tag{3.7}$$

Note that the sign of the Seebeck coefficient depends on the charge type of the majority carriers.

It is often convenient to discuss the thermodynamic quantities by means of the Peltier heat, instead of the Seebeck coefficient. The Peltier coefficient Π is the energy carried by the electrons per unit charge, which is defined by the Kelvin relation

$$\Pi \equiv qTS_Q. \tag{3.8}$$

For semiconductors, it is preferable to measure a charge carrier energy relative to the Fermi energy E_F. Then, for free carriers, it can be written as $\Pi(E) = |E - E_F|$. If there is no gap state in the system considered; i.e, if there exsits carrier motion only at energies $E > E_C$ or at $E < E_V$, one obtains the following expressions [69]:

$$S_Q = -\frac{k_B}{q}\left(\frac{E_C - E_F}{k_BT} + A_C\right) \quad \text{for } E > E_C \tag{3.9}$$

$$S_Q = \frac{k_B}{q}\left(\frac{E_F - E_V}{k_BT} + A_V\right) \quad \text{for } E < E_V, \tag{3.10}$$

where terms A_C and A_V account for the fact that the carriers are distributed beyond E_C and below E_V, respectively. These are of order unity ($1 \sim 3$) and usually negligible quantities for nondegenerate semiconductors.

3.2.3 UPS Measurements

Photoelectron spectroscopy utilizes photoionization and energy-dispersive analysis of emitted photoelectrons to study the composition and electronic states at the surface of a specimen. Ultraviolet photoelectron spectroscopy (UPS) refers to a measurement using vacuum UV (10–45 eV) radiation to examine the valence levels of a specimen. For UPS, a He-discharge lamp emitting He–I monochromatic radiation with the energy of 21.2 eV is most frequently used. The principle of measurement is based on a single photon-in/electron-out process. The energy of a photon is given by $E = h\nu$, where h is the Planck constant and ν is the frequency of the radiation. The photon can interact with valence levels of the specimen under investigation, leading to ionization of the molecule or solid by removal of one of these valence electrons.

The process of photoionization can be schematically represented as follows: For the photoemission,

$$M + h\nu \rightarrow M^+ + e^-, \tag{3.11}$$

where M and M^+ is the neutral and ionized state, respectively, of a molecule or solid, and e^- is the emitted electron. Energy conservation requires that

$$E(M) + h\nu = E(M^+) + E(e^-). \tag{3.12}$$

Since the electron energy is present solely as kinetic energy, Eq. (3.12) can be rearranged to give an expression for the kinetic energy E_{kin} of the electron:

$$E_{kin} = h\nu - [E(M^+) - E(M)]. \tag{3.13}$$

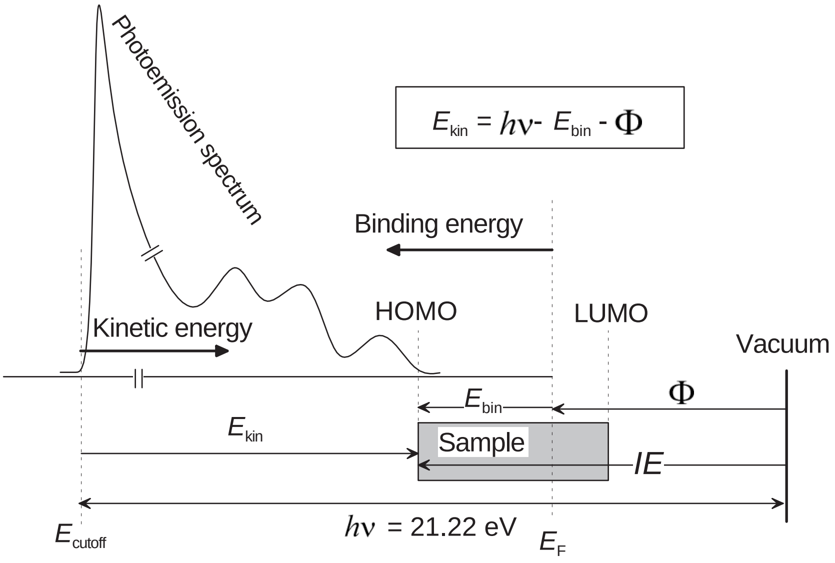

Figure 3.13: Interpretation of energy levels of a sample from a photoemission spectrum. Knowing the Fermi levels of the analyzer and the substrate, the binding energy $E_{bin} = E_F -$ HOMO can be determined. In order to determine the work function Φ or the ionization energy *IE* of the sample, the onset of the kinetic energy E_{cutoff} has to be well defined.

The term in the brackets, which represents the energetic difference between the ionized and neutral atoms, is generally called the binding energy E_{bin} for an electron in the specimen. In a real experiment, the energy levels should be referred to the vacuum level. This requires the introduction of the work function Φ of the substrate into Eq. (3.13), leading to the commonly quoted equation:

$$E_{kin} = h\nu - E_{bin} - \Phi. \tag{3.14}$$

The kinetic energy distribution of the emitted photoelectrons, i.e., the number of emitted photoelectrons as a function of kinetic energy, can be measured using an appropriate analyzer for electron energies.

3.3 Preparations and Methods

Materials

Fullerene C_{60} is provided from the Kurchatov Institute (Moscow, Russia). The matrix material pentacene is synthesized by a method based on reduction of pentacene-6,13-dion as the starting compound (Institute for Organic and Macromolecular Chemistry, University of Bremen). Information on the molecular orbitals for the matrix is also provided by semiempirical PM3 calculations with Hyperchem. Another matrix material ZnPc is purchased (Aldrich). For a phosphorescent molecule, an iridium complex TER004 is provided from Covion Organic Semiconductors GmbH (Frankfurt am Main, Germany).

The donor compound $[\mathrm{Ru(t\text{-}but\text{-}trpy)_2}]^0$ is synthesized in an electrochemical cell (Chemistry Department, Colorado State University) and kept either in vacuum or in a purified nitrogen atmosphere. The cationic dye AOB is purchased (Aldrich). For a stronger doping, a donor compound NDN1 is provided from Novaled AG (Dresden, Germany). The acceptor compound F_4-TCNQ is purchased (Acros Organics).

For a hole transport buffer layer, N,N,N',N'-Tetrakis(4-methoxyphenyl)-benzidine (MeO-TPD) and 4,4',4"-tris(2-naththylphenylamino)-triphenylamin (TNATA) are purchased (Syntec GmbH) and used to ensure a smooth interlayer between indium tin oxide (ITO) and pentacene layers. The HOMO of TNATA lies at nearly the same level [70] as that of pentacene.

Co-evaporation

All compounds except $[\mathrm{Ru(t\text{-}but\text{-}trpy)_2}]^0$ are purified at least twice by vacuum gradient sublimation. Thermal evaporation of the doped and undoped organic layers are performed in ultrahigh-vacuum chambers (pressure $< 10^{-5}\,\mathrm{Pa}$), controlling the doping rate and layer thickness by quartz-oscillator sensors.

OFET Samples

Heavily doped Si-wafers covered with a 90 nm oxide layer (capacitance $C_i = 36.8\,\mathrm{nF/cm^2}$) are utilized as the bottom-gate of the field-effect substrates. Gold interdigitated source-drain contacts, having a typical channel length $L = 20\,\mu\mathrm{m}$ and width $Z = 150\,\mathrm{mm}$, are patterned on the insulator (Fraunhofer Institut für Photonische Mikrosysteme, Dresden). The substrates are cleaned by ultrasonic treatment in acetone and ethanol followed by oxygen RF-plasma treatment.

For each sample, 50 nm of C_{60} layer doped with AOB is thermally co-evaporated onto each substrate. During the deposition, each sample is illuminated by a halogen lamp (220 W), and the substrate temperature is kept at 70 °C. For the effects of heating and illumination on the samples, readers are referred to Ref. [8].

Field-effect measurements are carried out *in situ* and in dark condition after the sample preparation. The gate bias V_G is typically swept from 0.2 V to 8 V, while the source-drain voltage V_D is varied typically between 0.01 V and 0.05 V. Since V_G is always much larger than V_D, the gradual channel approximation holds.

Thermovoltage Samples

Quartz glass substrates are cleaned by ultrasonic treatment in acetone and ethanol, and two vapor deposited silver contacts with a distance of 5.0 mm are prepared onto each substrate for thermovoltage measurements. A linearly graded temperature distribution (1 K/mm) across the contacts is provided by two isolated copper plates for heating and cooling of the substrates. The thermovoltage is measured *in situ* in an ultrahigh-vacuum chamber after co-evaporation of the matrix and dopants.

UPS measurements

The ultra violet photoelectron spectroscopy (UPS) is performed with a hemispherical energy analyzer (SPECS PHOIBOS100). The UV light source is a helium arc lamp that provides a He (I) line at 21.22 eV. A gold foil is repeatedly cleaned by argon sputtering and then used as the common substrate for all the UPS measurements performed *in situ*.

Homojunction Samples

For homojunction devices, ITO-coated glass sheets (Thin Film Device Inc., sheet resistance $< 80\,\Omega/\Box$) are used as the substrates. All substrates are cleaned before the vacuum process by an ultrasonic treatment in acetone and ethanol and by rf-plasma treatment. Preparation of each layer is sequentially processed in ultrahigh-vacuum chambers The *J*–*V* characteristics are recorded either *in situ* or in purified nitrogen atmosphere.

Equipments

All DC electrical data in this work are recorded with a source measure unit (Keithley SMU236). Impedance measurements are performed with an LCR meter (HP 4284A). For photovoltaic studies of homojunctions, a sun simulator (Hoenle SOL1200) and a xenon lamp (ILC technology R150) are used as light sources for sample illumination. The light intensities are determined by an outdoor reference cell provided by the Fraunhofer Institut für Solare Energiesysteme (Freiburg, Germany). The absorption spectrum of a pentacene film is measured with a UV-vis-NIR photometer (Shimadzu UV-3100). Selective excitation of a homojunction sample is performed utilizing a set of xenon lamp and monochromator of a spectrofluorometer (SPECS FluoroMax).

4 Carrier Transport in Doped Organic Thin Films

Charge transport mechanisms in organic semiconductors are of great importance since they are the basis for a new class of electronic and optoelectronic devices. Therefore, before discussion of device physics, we here discuss the fundamental quantity of carrier transport in semiconductors: Field-effect mobility. Carrier transport in organic films is usually dominated by hopping processes, and the field-effect mobility is gate bias dependent. We demonstrate that the mobilities in n-doped C_{60} films have no gate bias dependence and show a temperature dependence analogous to inorganic semiconductors. In contrast to the previous studies for organic films, the mobilities are not controlled by a trap-filling mechanism, but better characterized by impurity scattering typically observed in inorganic semiconductors.

4.1 Field-Effect Mobility in C_{60} Thin Films

In typical inorganic semiconductors, carriers move in bands with room temperature mobilities of approximately $10^3\,\mathrm{cm}^2/(\mathrm{Vs})$. The carrier mobility in general tends to decrease at high temperatures due to phonon scattering, and strongly increases with decreasing temperature. The increase of mobility is usually masked at very low temperatures by the influence of ionized impurity scattering due to the dopant atoms. With increasing dopant density, the mobility further decreases. Such band transport can be also expected for organic semiconductors with mobility typically larger than $1\,\mathrm{cm}^2/(\mathrm{Vs})$ [18,19]. A strong increase of mobility with decreasing temperature, being characteristic for band transport, has indeed been observed [1,60,71] in molecular single crystals.

In contrast to crystals, organic thin films are generally characterized by temperature-activated hopping transport, which leads to low mobilities and a strong influence of disorder. In those systems, very different carrier transport properties are usually observed: The mobilities are thermally activated and increase with increasing temperature, i.e., opposite to the behavior of crystals. These observations have been explained by hopping transport due to structural and energetic disorder [28,29,72,73].

For our studies, we have chosen fullerene C_{60} as the matrix and an organic dye AOB as the molecular dopant. Although intercalation of C_{60} with alkali and alkaline-earth metals was developed and studied in detail in the 1990s [51], the semiconducting properties in n-doped C_{60} films have been so far scarcely discussed. In order to study the fundamental transport properties of doped C_{60} films, we have performed field-effect measurements. Comparatively high field-effect mobilities (above $1\,\mathrm{cm}^2/\mathrm{Vs}$) in undoped C_{60} films have already been reported in the literature [74–76]. In the following Subsection, we first discuss the results of our field-effect measurements for undoped C_{60} films. Characteristics of doped C_{60} field-effect samples are discussed in the second Subsection.

4.1.1 Characteristics of Undoped C_{60} Field-Effect Sample

Figure 4.1 shows the channel characteristics (I_D–V_D) of typical undoped C_{60} field-effect samples. Normally, undoped C_{60} films form a small depletion layer at the vicinity of dielectric oxides, and also at the source–drain contact interfaces. Therefore, with zero gate bias, the I_D–V_D characteristics have a small threshold, and the current I_D is generally very low. With a gate bias V_G applied, an accumulation of induced electrons occurs at the dielectric interface, and I_D is strongly increased depending on V_G. However, when V_D becomes considerably larger than V_G, a depletion of C_{60} is again formed at the drain contact interface; thus, saturation of I_D with regard to V_D occurs [see Fig. 4.1 (a)].

On the other hand, in a small V_D region above the threshold, the C_{60} channel characteristics can be adequately approximated by a linear response [see Fig. 4.1 (b)]. Evaluation of the field-effect mobility μ_{FE}, according to Eq. (3.4) in the linear regime, is thus possible.

Figure 4.2 shows the evaluated μ_{FE} of an undoped C_{60} sample. The mobilities around room temperature are strongly gate bias dependent: A large V_G is required to reach a maximum mobility at each temperature. The mobility is also thermally activated in the measured temperature range up to 395 K. The observations can, e.g., be explained by the influence of trap levels [77], or by the multiple trapping and release model [31] developed to interpret the temperature and gate bias dependence of the field-effect mobility, which are actually in accordance with the aforementioned hopping transport models for organic films.

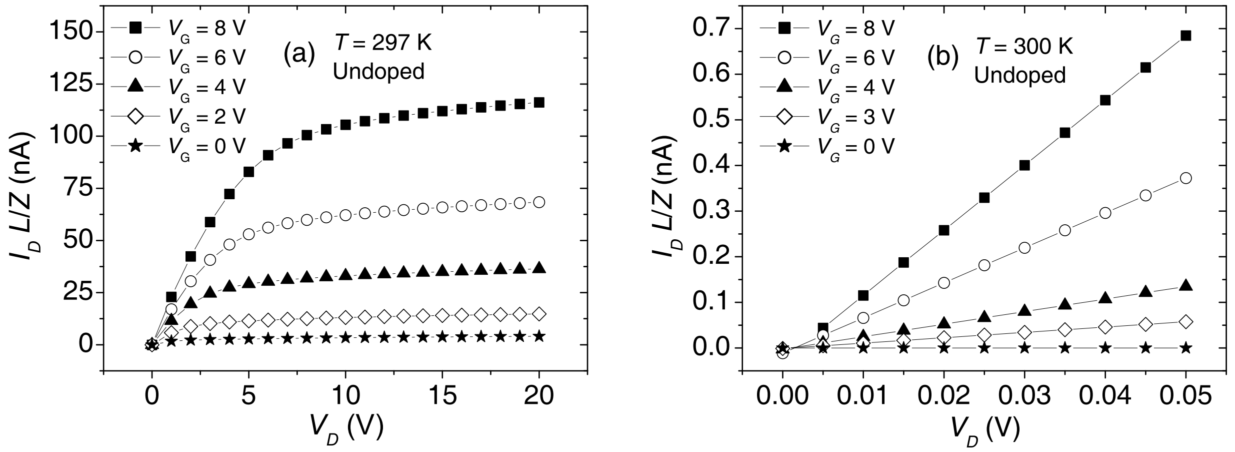

Figure 4.1: Channel characteristics of undoped C_{60} field-effect samples for (a) a large V_D range and (b) a small V_D range with a variety of gate biases applied. The source-drain currents are plotted as the specific current scaled by the channel length L per channel width Z.

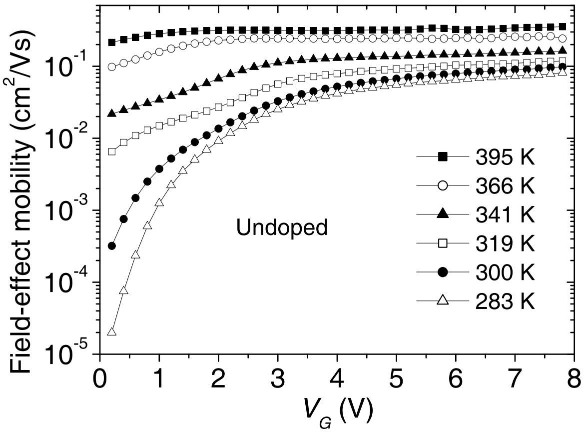

Figure 4.2: Field-effect mobility of an undoped C_{60} sample at several temperatures as a function of gate bias voltage.

It should be noted that the characteristics of n-type field-effect transistors are often influenced by surrounding conditions, such as oxygen content in the atmosphere [78], injection barrier at contacts [74], and the interfacial status of dielectrics [79]. Indeed, we found especially in our undoped C_{60} samples remarkable changes in the threshold voltages and gate bias dependence of the characteristics, depending on the cleaning and heating processes of the substrates. This infers that the electronegativity of the dielectric surface has a serious influence on the initial depletion of C_{60} at the interface. For the reproducibility of measurements, we have strictly maintained the procedure of sample preparation listed in the Chapter 3, not only for the undoped samples, but also for n-doped samples.

4.1.2 Characteristics of Doped C_{60} Field-Effect Sample

A gate bias in an field-effect sample induces charge carriers in the organic film. On the other hand, the charge density can be increased also by doping of extrinsic impurities. For

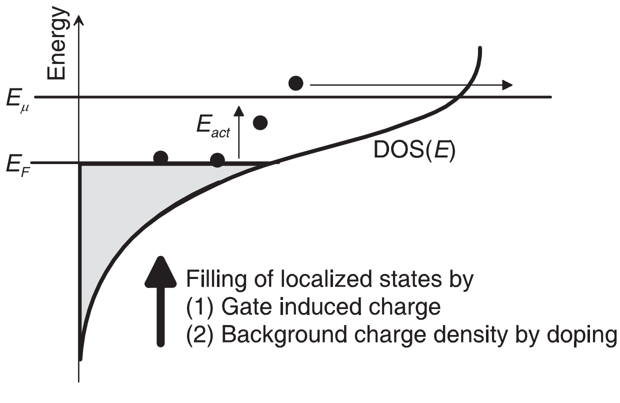

Figure 4.3: Schematic image for charge density dependent mobility in a disordered system: E_μ, carrier transport level; E_{act}, activation energy of mobility; E_F, the Fermi energy.

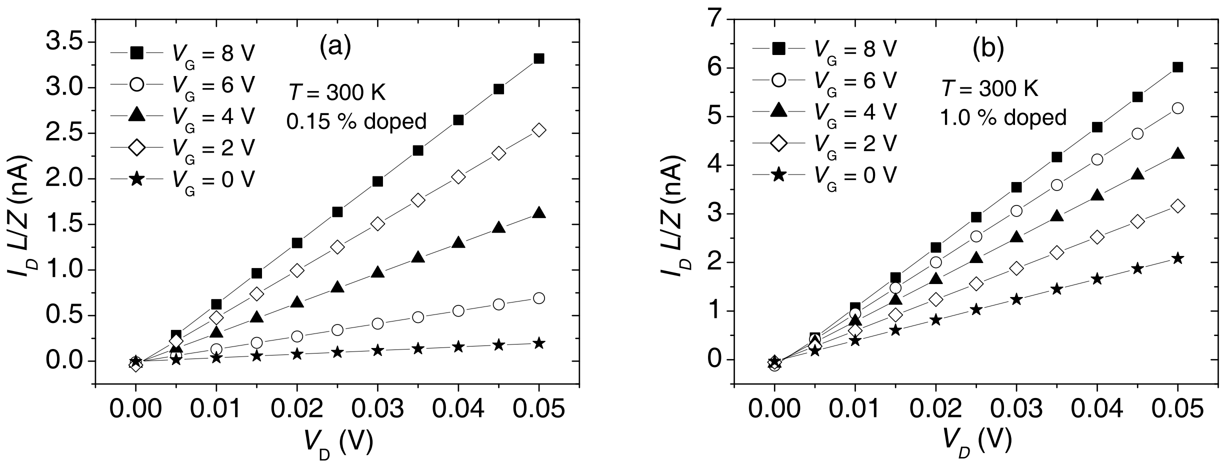

Figure 4.4: Channel characteristics of C_{60} field-effect samples doped with (a) 0.15 mol % of AOB and (b) 1.0 mol % of AOB, with a variety of gate biases applied.

a qualitative understanding, a model of charge density dependent mobility in a disordered system is schematically shown in Fig. 4.3. An increase of the charge density by (1) gate bias or (2) doping results in a filling of the localized tail states in the DOS distribution, leading to a reduction of the activation energy E_{act}, and hence, an enhancement of the effective mobility at the carrier transport level E_{μ}.

Bulk conductivities of the C_{60} samples doped with AOB are measured with zero gate bias, exceeding 10^{-4} S/cm at 200 K and being of the order on 10^{-2} S/cm at 300 K. The potential bending at the vicinity of the dielectric interface will be small and sharp since the Fermi energy is close to the charge transport level in the C_{60} layer: An accumulation channel should immediately form with a small gate bias applied. The source-drain current I_D is not controlled by a depletion layer: The channel characteristics are in any case ohmic because of the efficient carrier injection. The characteristics have thus no threshold, and do not exhibit saturation. Figure 4.4 shows the typical channel characteristics of doped C_{60} field-effect samples.

Figure 4.5 shows the field-effect mobilities of the doped samples determined in the linear regime as a function of the gate voltage. It is visible that for the weakly doped samples [Fig. 4.5 (a)], the mobility quickly rises with increasing gate voltage, exhibiting that the induced carriers saturate low-mobility states. For higher doping ratio, this effect disappears [Fig. 4.5 (c)], indicating that the chemical doping is sufficient to fill those states.

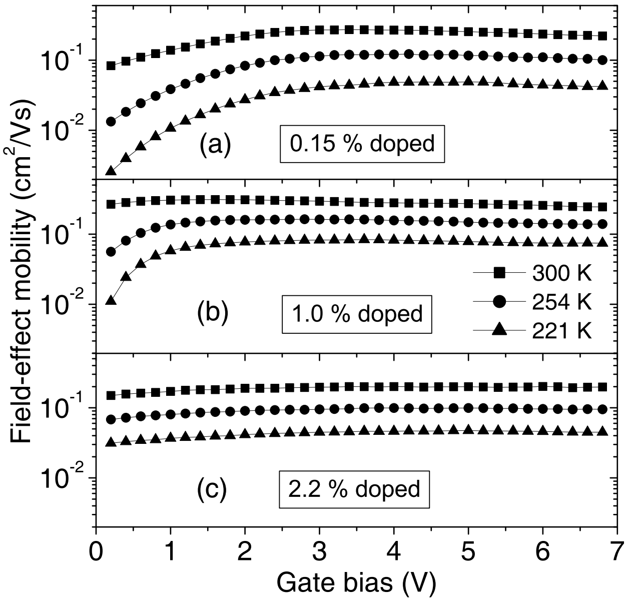

Figure 4.5: Field-effect mobilities of doped C_{60} samples. Obtained μ_{FE} from three samples doped with (a) AOB 0.15 mol %, (b) 1.0 mol %, and (c) 2.2 mol % at different temperatures are shown as a function of gate bias voltage.

4.2 Transport Mechanism in Doped C_{60} Thin Films

4.2.1 Phonon Scattering and Impurity Scattering

For band transport, scattering of electrons by phonons and impurities is the substantial mechanism that impedes coherent motion of charge carriers. At high temperatures, the amplitude of lattice vibrations (the phonon number) is large, and the electron–phonon interaction is significant. In the idealized case of an intrinsic semiconductor, the scattering probability is a function of the square of the amplitude of the phonon wave. As a consequence, the mobility follows a power law for temperature variation [80] as

$$\mu \propto T^{-1.5}. \tag{4.1}$$

Scattering by impurities can be treated in terms of classical mechanics: The Rutherford cross section is proportional to the number of ionized impurity centers, and inversely proportional to the square of the thermal energy of electrons. An increase of doping concentration therefore causes a concomitant decrease of the carrier mobility, and especially at low temperatures, the mobility decreases with decreasing temperature following a relation [81]

$$\mu \propto \frac{T^{1.5}}{N_D}, \tag{4.2}$$

where N_D is the density of the ionized impurities.

It was reported for organic thin films that the temperature dependence of the field-effect mobility can widely vary from hopping-like to temperature-independent behavior [82]. More recently, it was observed that on a picosecond time scale, carriers in pentacene thin films can show bandlike transport before relaxing into more localized states [83]. A discussion of the scattering mechanisms is difficult in both cases since the impurity levels are not controlled. We will discuss in the following Subsections the temperature and doping ratio dependence of C_{60} mobilities.

Dependence of Mobility on Temperature

Figure 4.6 shows the temperature dependence of the mobilities for C_{60} samples with the doping ratio varying from 1 to 7 mol %. There are two remarkable deviations from previous observations in thin-film organic semiconductors: First, unlike the common hopping transport feature, the mobilities decrease with temperature in the range slightly above room temperature; second, the mobilities decrease with increasing doping density, in clear contrast to all previous observations in doped organic semiconductors. The overall temperature dependence of our samples thus very much resembles the behavior of crystalline inorganic semiconductors, such as silicon.

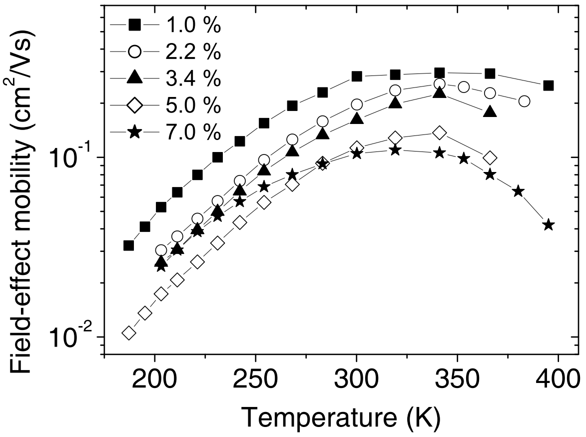

Figure 4.6: Temperature dependence of field-effect mobilities for doped C_{60} samples. AOB doping ratios are varied from 1.0 to 7.0 mol %. Data are taken from the range between $V_G = 2\,\mathrm{V}$ and $6\,\mathrm{V}$, where the mobilities are constant and independent of V_G. The solid lines are guides to the eye.

Dependence of Mobility on Doping Ratio

Next, we attempt to model the data using the well-known Matthiessen rule [17]:

$$\frac{1}{\mu_{FE}} = \frac{1}{\mu_p} + \frac{1}{(c/N_D)\mu_i}. \tag{4.3}$$

Here, we use two mobility constituents, μ_p and μ_i, related to phonon and impurity scattering, respectively. The latter depends on the doping ratio N_D with a proportionality constant c. Figure 4.7 shows the field-effect mobilites at several temperatures as a function of doping ratio. The plots of μ_{FE} versus N_D at temperatures around 200–300 K can be well fitted by the solid lines calculated using Eq. (4.3). Note that in the accumulation channel of an n-doped field-effect sample with gate bias, μ_{FE} should originate from the immediate vicinity of the dielectric interface where the electronic states are virtually degenerate; therefore, the

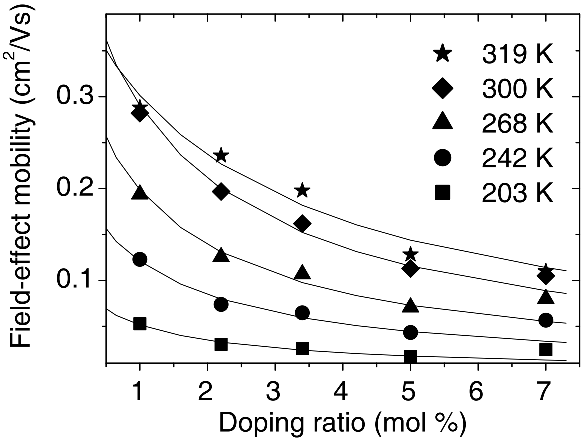

Figure 4.7: Field-effect mobilities of C_{60} samples at several temperatures as a function of AOB doping ratio. The solid lines represent the fitting curves calculated using Eq. (4.3).

donor states are practically considered to be fully ionized. The decrease of mobility with increasing impurity concentration is thus properly described by the method generally used for band transport in crystals.

4.2.2 Thermionic Emission at Grain Boundaries

A more detailed inspection on temperature dependence, however, shows deviations from the established models: The analysis of the fitting parameters, μ_p and μ_i, is summarized in Fig. 4.8 as a function of temperature. The fitting parameter μ_p does not show the negative temperature coefficient $T^{-1.5}$ typical for phonon scattering, and also the slope of μ_i versus T increases more strongly than with the power of 1.5 expected for ionized impurity scattering. Although the power law for the idealized case may not be exactly applicable to organic materials [1], the observed temperature dependence is rather strong, inferring a thermal activation process which prevails the power law at low temperatures. This large activation energy cannot be ascribed to homogeneously distributed trap states or intrinsic disorder only: If so, the mobilities should have been also increased by the gate voltage.

A possible explanation for the activation is the existence of depleted potential barriers at the carrier transport level, which may be introduced by deep interface states typically present at grain boundaries of polycrystalline semiconductors [31, 84, 85]. In such a case, the Debye

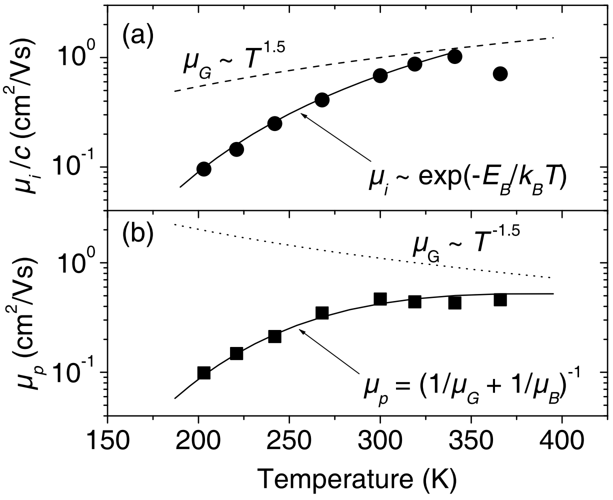

Figure 4.8: Temperature dependence of the fitting parameters deduced from Eq. (4.3). (a) Values obtained for the impurity-dependent parameter μ_i. The dashed line is a reference curve of $T^{1.5}$. The solid line on the data is the fitting curve using Eq. (4.4) because $\mu_i(T)$ is virtually determined by $\mu_B(T)$, which yields $E_B = 0.11\,\mathrm{eV}$ and $\mu_{B0} = 40$. Here, μ_i is normalized with the coefficient $c = 0.0113$ so that the prefactor μ_{B0} matches with that of μ_p. (b) Values obtained for the impurity-independent parameter μ_p. The dotted line represents the phonon scattering mobility μ_G calculated from Eq. (4.5), with $\mu_{G0} = 1.1\,\mathrm{cm^2/(Vs)}$ and $T_0 = 300\,\mathrm{K}$. The solid line is the result of a calculation from Eq. (4.6) with the parameters mentioned above.

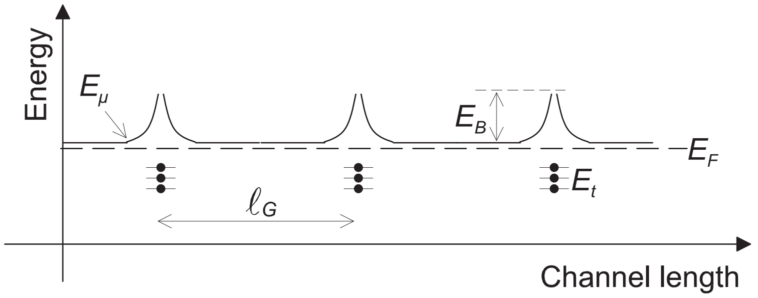

Figure 4.9: Schematics of potential barriers at grain boundaries along an accumulation channel in a polycrystalline semiconductor: E_B, barrier height; ℓ_G, grain size; E_μ, electron transport level; E_F, the Fermi level; E_t, interfacial trap level. The donor level is not represented here for simplicity.

length of potential barriers in our doped C$_{60}$ samples is expected to be very small and of the order of a few intermolecular distances due to the high charge density. Therefore, no overlapping of depletion would take place in the grains, and the channel current between the grains will then undergo thermionic emission at the boundary. Figure 4.9 shows a schematic picture of potential barriers where the thermionic emission of electron current should occur. The mobility at the grain boundary μ_B is defined as

$$\mu_B = \mu_{B0} \exp\left(-\frac{E_B}{k_B T}\right), \tag{4.4}$$

with μ_{B0} being the weakly temperature-dependent prefactor, E_B the barrier height, and k_B the Boltzmann constant. The grain mobility μ_G can be expressed in a form

$$\mu_G = \mu_{G0} \left(\frac{T}{T_0}\right)^{-1.5}, \tag{4.5}$$

where μ_{G0} is a prefactor and T_0 is a characteristic temperature of the system.
Using Eqs. (4.4) and (4.5), the mobility constituents μ_p and μ_i may be rewritten as

$$\frac{1}{\mu_{p/i}} = \frac{1}{\mu_G} + \frac{1}{\mu_B}, \tag{4.6}$$

where μ_G denotes the mobility in the grain. We obtain $E_B = 0.11\,\mathrm{eV}$ from the curves of μ_p and μ_i at low temperatures in Fig. 4.8.
After all, a fit of the μ_p curve with Eq. (4.6) yields the phonon limited grain mobility $\mu_G = 1.1\,\mathrm{cm}^2/(\mathrm{Vs})$ at 300 K, which is at the border generally expected for a bandlike mobility. We note, however, that the obtained μ_G in our field-effect samples may still be restricted by the rough morphology of the dielectric interface since, with elaborate thin-film forming techniques, considerably higher C$_{60}$ field-effect mobilities have been actually reported [75,76].

A puzzling observation is the decrease of μ_i at high temperatures [see Fig. 4.8 (a)], which can not be accounted for by the above discussion: i.e., the limitation of mobility is not due only to phonon scattering, but an influence of the impurity level also exists. At these high temperatures, the experimental data actually show some irregularities that depart from the fit curves from Eq. (4.3). This infers that some other contribution, which is at present unknown and is not linearly related to the doping ratio N_D^{-1}, should be taken into account for a more precise description of the scattering processes.

4.3 Summary: Carrier Transport in Doped C_{60} Films

In summary, we have shown that the strong *n*-dopant AOB can provide sufficient charge carriers for C_{60} organic thin films to realize a highly efficient electron transport. The doped C_{60} layers can show transport properties which strongly differ from previous observations in organic thin films: Similarly to crystalline inorganic semiconductors, the mobility decreases with increasing temperature and with increasing dopant concentrations.

The temperature dependency of the mobility is qualitatively consistent to the impurity and phonon scattering models. The data can be modelled with the Matthiessen's rule generally applied for band transport. However, we also observe deviations which could be explained by band transport in grains separated by grain boundaries.

5 Organic p-i-n Homojunctions

Strong molecular acceptors and donors make a given organic semiconductor either p-type or n-type. We thus realize organic p-i-n homojunctions composed of differently doped vacuum-deposited organic layers. The archetype homojunctions of several organic matrices with different energy gaps are prepared, and all of them show stable and reproducible diode characteristics. In this Chapter, we will discuss the fundamental features of the organic p-i-n homojunctions, such as built-in potential and current–voltage characteristics.

5.1 Homojunction Matrices

The *p*-*n* homojunction is the archetype of semiconductor devices. Inorganic silicon *p*-*n* homojunctions as well as amorphous silicon *p*-*i*-*n* homojunctions have been long used for commercial solar cell applications. The dark and illuminated diode characteristics of the amorphous silicon homojunctions has been already studied extensively in the 1980s [36, 88–90]. In comparison, the fundamental properties of organic semiconductor junctions are still much less understood. Despite some attempts with electrochemical systems [91–94], no detailed study of the junction formation and the diode characteristics has been conducted for organic semiconductors.

Organic semiconductors are usually characterized by a high degree of disorder and concomitant localization of charge carriers. On the other hand, since organic semiconductors retain their electronic structures of closed molecular systems, the number of intrinsic defects in organic thin films is generally much lower than that in inorganic amorphous films having a large number of dangling bonds. It is interesting to clarify whether the characteristics of an organic homojunction follow the standard semiconductor theories represented by Shockley [32]. In the following, we will discuss the energetics and the diode characteristics of the *p*-*i*-*n* homojunctions prepared with different organic matrices.

5.1.1 Homojunction Structure

The organic *p*-*i*-*n* homojunction discussed here is a diode composed of three organic layers of the same matrix, but with different electrical properties: namely, *p*-doped, undoped, and *n*-doped layers. A sequential vacuum deposition of *p*-, *i*-, and *n*-layer leads to a *p*-*i*-*n* homojunction, and the organic layers are sandwiched by metal contacts. The intrinsic interlayer is necessary to achieve a blocking junction since the rather narrow space-charge layers would

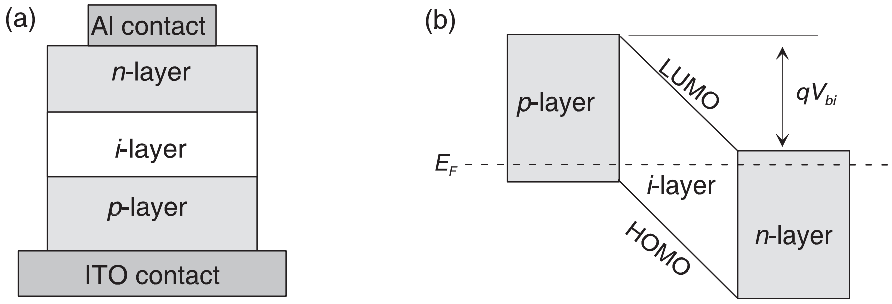

Figure 5.1: (a) Basic structure of an organic *p-i-n* homojunction sandwiched by ITO and Al contacts. (b) Schematic energy diagram of an organic *p-i-n* homojunction at thermal equilibrium, in which the built-in potential qV_{bi} drops across the *i*-layer.

cause tunneling [48]. Figure 5.1 shows the basic structure of the *p-i-n* homojunctions used in this study.

Recently, we have realized ZnPc *p-i-n* homojunctions utilizing the bipolar doping of the matrix with strong donor $[Ru(terpy)_2]^0$ and acceptor F_4-TCNQ. The ZnPc homojunctions show well rectifying diode characteristics with stable and reproducible performance [2]. For this thesis work, we employ further strong donor compounds such as $[Ru(t\text{-}but\text{-}trpy)_2]^0$ or NDN1. Thus, an efficient *n*-doping of a matrix with relatively higher-lying LUMO becomes possible. It is thus also possible to prepare a *p-i-n* homojunction in materials with larger energy gaps.

5.1.2 Bipolar Doping

We first show that several organic matrices can be both *n*- and *p*-doped. As an example, conductivities of ZnPc films doped with the acceptor F_4-TCNQ and the donor $[Ru(t\text{-}but\text{-}trpy)_2]^0$ are shown in Fig. 5.2. Both *p*-doped and *n*-doped samples show comparatively high conductivities which superlinearly increase with increasing doping concentration. This indicates that the carrier transport is dominantly taking place at higher DOS levels due to the charge density introduced by the shallow acceptors and donors [30]. Figure 5.2 also shows the conductivities of *n*-ZnPc doped with $[Ru(terpy)_2]^0$ as comparison. It can be seen that the strong donor $[Ru(t\text{-}but\text{-}trpy)_2]^0$ leads to a conductivity three orders of magnitude higher than for $[Ru(terpy)_2]^0$, which is consistent to the estimation that the alkyl substitution should lift the HOMO of the complex 0.1–0.2 eV higher than the level of the unsubstituted ligand complex.

In addition to ZnPc, we have chosen pentacene as the matrix for the organic homojunction studies because it is one of the most thoroughly investigated organic materials with a large application potential. Also, we have chosen a phosphorescent emitter complex TER004 as the matrix because its electron and hole transport properties are excellent. Table 5.1 shows typical HOMO–LUMO gap values of the matrices seen in literature, which will be verified

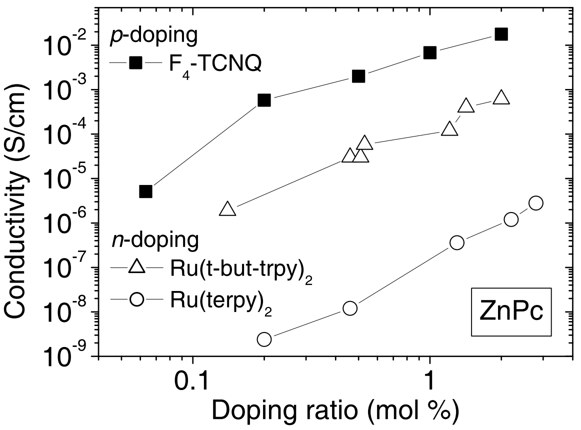

Figure 5.2: Conductivities of p-doped (with F_4-TCNQ) and n-doped (with $[Ru(terpy)_2]^0$ and $[Ru(t\text{-}but\text{-}trpy)_2]^0$) ZnPc films at room temperature as a function of doping ratio. The data for p-ZnPc are extracted from Ref. [30].

in the following discussions.

As already mentioned in Section 3.1 of Chapter 3, the difficulty in the realization of the organic homojunctions lies in the energetics of the matrix, p-dopant, and n-dopant molecules: The charge transfer between the matrix and dopants should be efficient enough that both p-type and n-type conduction can be achieved in the same organic semiconductor matrix. We use F_4-TCNQ for p-doping of the three matrices, and $[Ru(t\text{-}but\text{-}trpy)_2]^0$ for n-doping of ZnPc and pentacene matrices. The even stronger donor molecule NDN1 is particularly needed for n-doping of TER004 because of the relatively large energy gap (higher-lying LUMO).

The high conductivities in the doped layers are obvious from the completely ohmic responses of the current versus voltage. The injection of charge carriers from metal contacts are in any case very efficient, being free from the contact barrier problems. The results of conductivity measurements at room temperature are listed also in Table 5.1. The measurements are carried out *in situ*, and the conductivity values are individually obtained for the n-doped and p-doped samples of ZnPc, pentacene, and TER004.

Table 5.1: HOMO–LUMO gap values for three matrices reported in literature. Conductivities σ at room temperature under an electric field of 40–60 V/cm for p-doped and n-doped matrices with a typical doping ratio of 2–3 mol % are also listed.

Matrix	Energy gap (eV)	σ (S/cm)	
		p-doped	n-doped
ZnPc	1.57 [86]	1×10^{-2}	6×10^{-4}
Pentacene	2.2 [16], 1.97 [55]	6×10^{-4}	7×10^{-5}
TER004	2.61 [87]	4×10^{-6}	2×10^{-4}

Conductivities of undoped samples of the three matrices are also measured, and confirmed to be below the detection limit: i.e., lower than 10^{-10} S/cm. The large differences in conductivity of doped and undoped samples ensure that built-in potential and applied bias voltage drop across the *i*-layer, and virtually no electric field is present in the doped layers.

5.2 Energetics of Organic Homojunctions

For a detailed investigation of diode characteristics, accurate knowledge of energetic values, such as energy gap of the organic matrix or built-in potential of the semiconductor junction, is indispensable. Ultraviolet photoelectron spectroscopy (UPS) is a well known method to study HOMO levels of organic materials. The energy gap of an organic material is often roughly estimated by inverse photoemission spectroscopy, or from an optical absorption spectrum.

We here demonstrate an alternative method to determine the energetics of organic homojunctions: We utilize data achieved from UPS and thermovoltage measurements, which give more realistic energetic values for carrier transport characteristics. The method is especially useful for an energy gap determination of, e.g., a rare-earth metal complex whose singlet absorption edge is not clearly observed due to violation of the selection rule.

5.2.1 Measurements

Thermovoltage Measurements

For the first step to discuss the energetics, we investigate the equilibrium charge carrier statistics in doped organic films by means of thermovoltage measurements. As already discussed in Section 3.2 of Chapter 3, the Seebeck coefficient S_Q generally depends on the Fermi energy E_F and density of states (DOS) distribution of the system. For nondegenerate semiconductors, we assume that the Maxwell-Boltzmann approximation is applicable and that the carrier transport dominantly takes place at a specific energy level E_μ. Therefore, Eqs. (3.9) and (3.10) can be simply expressed as

$$S_Q = \frac{k_B}{q}\left(\frac{E_F - E_\mu}{k_B T}\right), \tag{5.1}$$

where k_B is the Boltzmann constant and T is the temperature. For a highly polarizable material such as pentacene, the energetic interval $|E_F - E_\mu|$ may include the polaronic vibration effect [95], which is of the order just a few $k_B T$ and has no significant influence on the following discussions. Note that for *n*-type semiconductors, S_Q has a negative value. The obtained Seebeck coefficients for *p*-doped and *n*-doped organic films are summarized in Fig. 5.3.

The Seebeck coefficient is indeed positive for *p*-doped films and is negative for *n*-doped ones

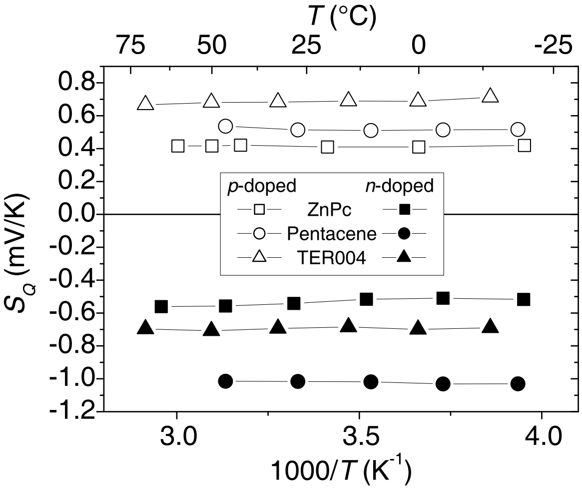

Figure 5.3: Seebeck coefficients S_Q at several temperatures obtained from thermovoltage measurements for p-doped and n-doped matrices with a typical doping ratio of 2–3 mol %. The data for p-ZnPc are extracted from Ref. [30].

as is expected and confirming that the molecular doping induces mobile carrier transport in the HOMO and LUMO, respectively, and not through the dopant states. The energetic distances $|E_F - E_\mu|$ at room temperature calculated from Eq. (5.1) are also listed in Table 5.2.

Table 5.2: Seebeck coefficients S_Q and energetic intervals $|E_F - E_\mu|$ at room temperature for p-doped and n-doped matrices.

Matrix	S_Q (mV/K)		$\lvert E_F - E_\mu\rvert$ (eV)	
	p-doped	n-doped	p-doped	n-doped
ZnPc	0.410 [30]	−0.542	0.120 [30]	0.163
Pentacene	0.514	−1.016	0.154	0.305
TER004	0.683	−0.697	0.208	0.212

UPS Measurements

The HOMO levels and absolute E_F values for the organic matrices can be confirmed by UPS. We perform UPS measurements for p-doped and n-doped thin films with the same doping condition as in the thermovoltage measurements and also for an undoped thin films. The large sample thicknesses (20–25 nm) ensure that the UPS spectra do not originate from the interface dipole regions, but do reflect the bulk electronic structures. Knowing the gold substrate workfunction, we can estimate E_F of each sample from the HOMO-cutoff level in the respective spectrum. As an example, a remarkable HOMO-cutoff shift between two

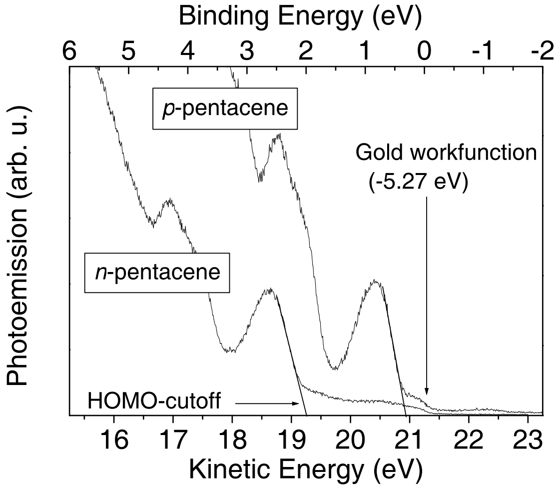

Figure 5.4: UPS spectra from *p*-doped and *n*-doped pentacene films with thicknesses of 20 nm. The abscissae indicate the detected electron kinetic energy and also the binding energy with respect to the substrate workfunction of -5.27 ± 0.05 eV.

spectra of *p*-doped and *n*-doped pentacene films can be seen in Fig. 5.4.

The results of all the measurements for the three matrices are listed in Table 5.3 together with the ionization potentials *IP* calculated from the HOMO cutoff and the high-binding-energy cutoff (HBEC) levels. Since only 2 mol % of doping and the corresponding change in charge density do not significantly alter the spectroscopic property of the bulk, the differences of the *IP* values for doped and undoped samples of the same matrix are attributed to the experimental accuracy in obtaining the HBEC levels. However, the obtained Fermi levels for *p*-doped and *n*-doped samples are definite and convincing values since these levels are well aligned to the common workfunction of the measurements.

Table 5.3: UPS data for doped and undoped matrices. The ionization potentials *IP* are calculated from HOMO-cutoff and HBEC levels. The Fermi energies E_F are estimated from the shift of HOMO-cutoff with regard to the gold workfunction. The data for *p*-ZnPc are extracted from Ref. [5].

Matrix	*IP* (±0.1 eV)			E_F (±0.1 eV)		
	p-doped	undoped	*n*-doped	*p*-doped	undoped	*n*-doped
ZnPc	−5.28 [5]	−5.22	−5.15	−5.10 [5]	−4.38	−3.91
Pentacene	−5.08	−5.03	−5.10	−4.90	−4.40	−3.25
TER004	−5.15	−5.23	−5.15	−5.06	−4.44	−2.82

5.2.2 Built-in Voltage and Energy Gap

A combination of the results from the thermovoltage and UPS measurements allows to describe the complete energetics of a *p*-*i*-*n* homojunction. As an example, a schematic of the energy diagram for a pentacene homojunction is shown in Fig. 5.5. We assume the HOMO of the pentacene matrix to be around −5.05 eV. Here, we use the terms HOMO and LUMO by convention to refer to the effective transport levels for holes and electrons, respectively. The energetic interval $|E_F - E_\mu|$ of the *p*-doped pentacene film from the Seebeck data ia about 0.15 eV (see Table 5.2). This quantity then matches the difference between E_{Fp} (E_F of the *p*-doped film) and HOMO given by UPS (see Table 5.3). This agreement justifies an estimation of the LUMO by adding $|E_F - E_\mu|$ of the *n*-doped pentacene film to E_{Fn} (E_F of the *n*-doped film) of the UPS data. As a result, we obtain approximately −2.95 eV for the LUMO level and 2.1 eV for the energy gap E_g, which are fairly consistent with values reported for pentacene films in the literature (see Table 5.1). It is therefore reasonable to correlate the Fermi difference between the two doped layers to the built-in potential V_{bi} in a pentacene *p*-*i*-*n* homojunction; i.e., $E_{Fn} - E_{Fp} = qV_{bi} = 1.65\,\text{eV}$. The same consideration holds for other matrices. The energetic values are summarized in Table 5.4

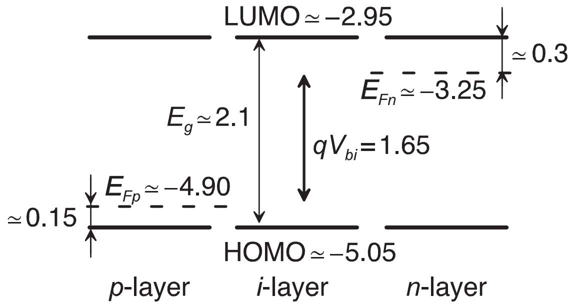

Figure 5.5: Energy diagram for a pentacene *p*-*i*-*n* structure (energy unit in eV): E_g, the energy gap; V_{bi}, the built-in voltage; E_{Fp} and E_{Fn}, the Fermi energy in *p*- and *n*-layers, respectively.

Table 5.4: Summary of energy values obtained from thermovoltage and UPS measurements for three matrices.

Matrix	HOMO (eV)	LUMO (eV)	V_{bi} (V)	E_g (eV)
ZnPc	−5.2	−3.7	1.2	1.5
Pentacene	−5.05	−2.95	1.65	2.1
TER004	−5.2	−2.6	2.24	2.6

5.3 J–V Characteristics

5.3.1 Standard Diode Characteristics

Figure 5.6 shows the dark *J–V* characteristics of the *p-i-n* homojunctions prepared by the three organic matrices. The *J–V* curves exhibit a good blocking behaviour in the reverse-bias region, and rectification factors of nearly 10^5 are obtained at all temperatures. In the forward-bias region below the built-in voltage, a shunt current at first appears to prevail; then, the current exponentially increases with the bias voltage. Such typical diode behaviour is reproducibly observed for each homojunction, indicating that the *J–V* characteristics are in principle described by the standard diode equation

$$J = J_0 \left[\exp\left(\frac{qV}{Ak_BT} \right) - 1 \right] , \tag{5.2}$$

where J_0 is the saturation current and A denotes the ideality factor.
In order to validate the applicability of the standard model, the *i*-layer thickness of ZnPc-

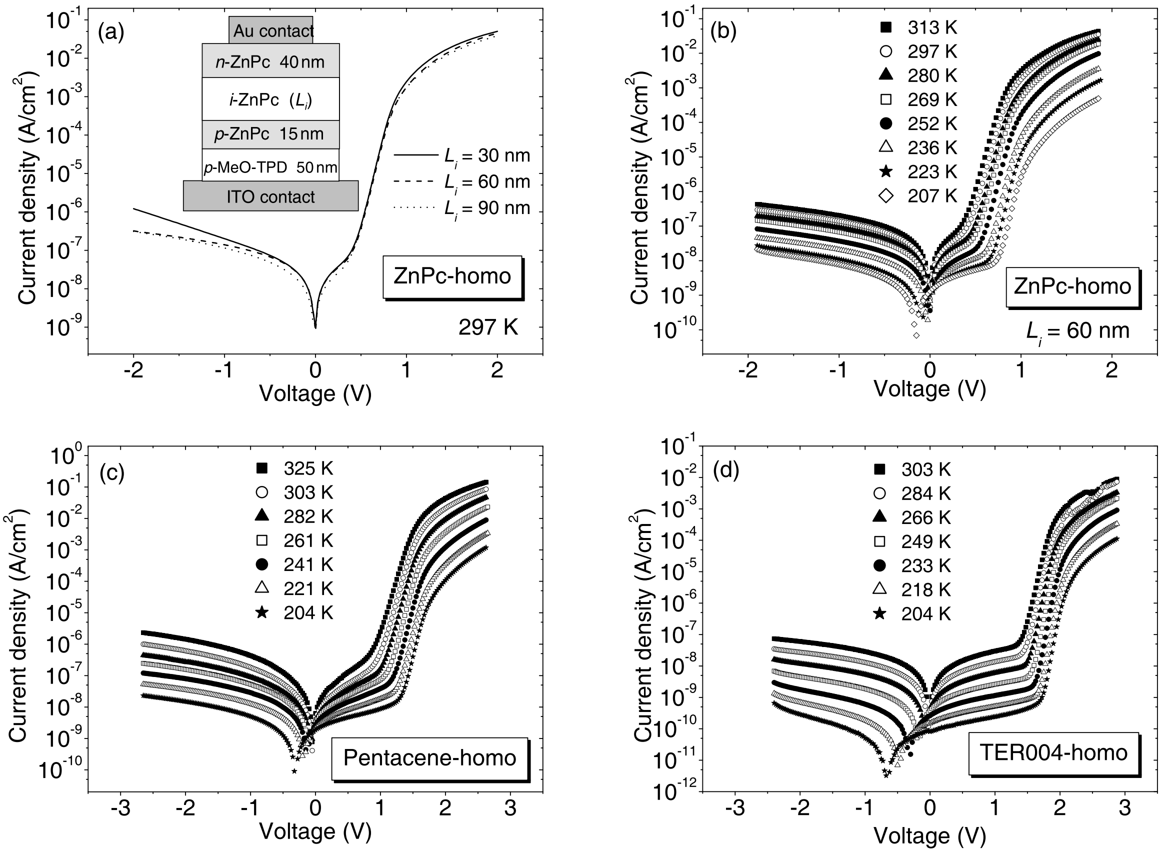

Figure 5.6: *J–V* characteristics of organic *p-i-n* homojunctions: (a) Room temperature characteristics of ZnPc-homojunctions with the *i*-layer thicknesses L_i of 30, 60, and 90 nm. The inset shows the sample structure. Characteristics at different temperatures for (b) ZnPc-homojunction, (c) pentacene-homojunction, and (d) TER004-homojunction.

homojunction is varied from 30 nm to 60 nm and 90 nm, respectively. The three *J*–*V* curves of the homojunctions with different *i*-thicknesses are shown in Fig. 5.6 (a). The curves show exactly same behaviour in the exponential part of the forward-bias region. Hence, we can rule out the influence of space-charge limited currents or field-dependent mobilities, which should strongly depend on the layer thickness and may mimic diode-like characteristics below the built-in potential. Thus, at room temperature, the *J*–*V* characteristics are sufficiently described by the conventional diode equation derived from the Shockley theory.

Furthermore, when the Al top contact of the ZnPc-homojunction is replaced by Au, it does not affect the *J*–*V* characteristics at all: Obviously, Au forms an ohmic contact with *n*-ZnPc. Since the work function difference of the ITO/ Au couple is much smaller and even opposite in sign to the ITO/ Al pair, we can conclude that it is not the contact workfunctions, but indeed the Fermi levels of the *p*- and the *n*-layer which are responsible for the built-in potential.

5.3.2 Temperature Dependence

However, the deviation from the standard theory becomes evident by consideration of the temperature dependence of the ideality factor A and the saturation current J_0. The parameters A and J_0 are acquired from the slope of the exponential *J*–*V* curve and its linear extrapolation. According to the general diode equation (5.2), $\partial(\ln J)/\partial V$ should increase with decreasing temperature if A is a constant. It is obvious from Fig. 5.6 for all the homojunctions that $\partial(\ln J)/\partial V$ depends only weakly on temperature. The estimated values of A at various temperatures can be seen in Fig. 5.7 (a), demonstrating that A increases with

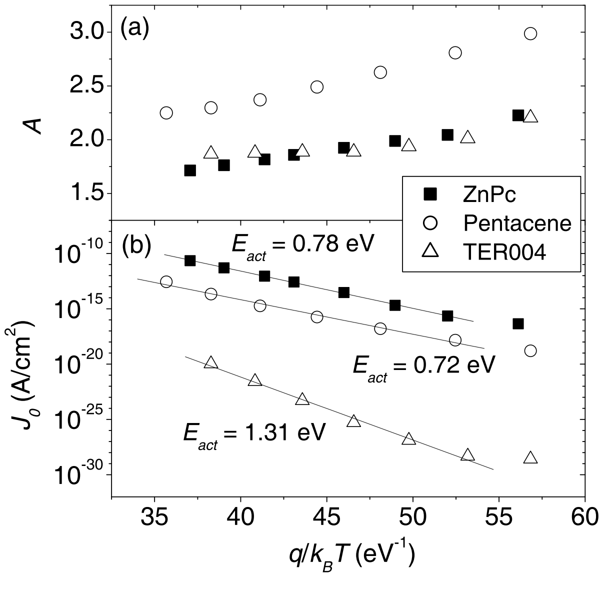

Figure 5.7: Temperature dependence of diode parameters for three homojunctions: (a) The ideality factor A; (b) Saturation current J_0. The solid lines are linear fits of the semilogarithmic plots for the current versus reciprocal temperature, which yield the activation energy E_{act} of J_0.

decreasing temperature.

Also, in the standard semiconductor theories, the activation energy of J_0 should correlate with the band gap of a *p*-*n* junction, or the barrier height of a Schottky junction, which is not the case for our *p*-*i*-*n* homojunctions. Figure 5.7 (b) shows the temperature dependence of J_0; obviously, the activation energies do not reflect the band gaps estimated for the three organic matrices.

The Einstein Relation

The large ideality factors around 2 infer in classical semiconductor junctions that charge carrier recombination in the *i*-layer would have considerable influence. The temperature dependence of A, however, requires another explanation: The deviation from the ideality can be explained by assuming that the quasiequilibrium balance between drift and diffusion currents in the disordered system is not maintained by the conventional Einstein relation.

A general relation between diffusion coefficient D and drift mobility μ is given by the generalized Einstein relation for an energy occupation function and a DOS function as [17]

$$\frac{D}{\mu} = \frac{n}{q\dfrac{\partial n}{\partial \xi}}, \tag{5.3}$$

where n is the charge carrier density and ξ is the chemical potential. In nondegenerate systems at thermal equilibrium, Eq. (5.3) is reduced to the conventional Einstein relation:

$$\frac{D}{\mu} = \frac{k_B T}{q}. \tag{5.4}$$

It has been pointed out that with increasing disorder, the relationship between D and μ of carriers significantly deviates from the conventional Einstein relation and does not explicitly depend on temperature at sufficiently low temperatures [96]. The deviations occur for transport under equilibrium [97] and nonequilibrium conditions [98].

In the Shockley theory for the *p*-*n* junction, the total current and the saturation current are deduced from the diffusion currents of minority carriers at the abrupt *p*-*n* boundary, where the presence of the local field is neglected. In comparison, the drift–diffusion theory takes into account the local field in the depletion layer of a Schottky diode. It is reasonable to assume for our *p*-*i*-*n* homojunctions that the total current is determined by a balance of drift and diffusion currents at the relatively thick *i*-layer; therefore, it should be treated in the framework of the drift–diffusion model.

As mentioned in Section 2.3 of Chapter 2, the Einstein relation is needed to eliminate either μ or D in the general form of the current equation for the drift–diffusion model.

In order to include the effect of the deviation from the conventional Einstein relation, we now tentatively let

$$\frac{D}{\mu} = \frac{n}{q\dfrac{\partial n}{\partial \xi}} = \frac{f(T)}{q}, \tag{5.5}$$

where $f(T)$ is some function that deviates from $k_B T$ and becomes less temperature-dependent at low temperatures. Then, a consideration of the current equation [Eq. (2.70)] for the drift and diffusion currents in the i-layer eventually leads to a usual diode equation [2] as

$$J = J_0 \left[\exp\left(\frac{qV}{f(T)} \right) - 1 \right], \tag{5.6}$$

with, however, a different temperature dependence from Eq. (5.2). The above consideration gives an implication that the ideality factor A should increase in the $1/T$ plot at low temperatures since $f(T)$ becomes temperature independent. This is in good agreement with the observation in Fig. 5.7 (a).

6 Pentacene Homojunctions

In this Chapter, we deal with photovoltaic effects of pentacene homojunctions. We have observed in Chapter 5 a remarkably high built-in voltage of 1.65 V for a pentacene homojunction: It is interesting to investigate whether the open-circuit voltage is directly related to the built-in voltage. We also aim to elucidate the individual charge transport properties of electrons and holes in pentacene thin films using the homojunctions as the archetype of organic semiconductor devices. We discuss in detail a presence of deep carrier trapping states in pentacene films utilizing single-carrier type homojunctions.

6.1 Pentacene p-i-n Homojunctions

Pentacene is one of the most thoroughly investigated organic materials with a large application potential owing to its excellent hole transport properties. While remarkably high hole mobilities have been reported for single crystals [60] and also for thin films [59], it has been indicated that pentacene is actually an ambipolar semiconductor [99] and the generally low electron mobility is merely due to the low injection problem: Indeed, comparably high field-effect mobilities of the order $0.1\,\mathrm{cm}^2/(\mathrm{Vs})$ for both electrons and holes are achieved in thin films [100, 101].

In the following, we first study the relation between the dark and illuminated current–voltage (J–V) characteristics of the pentacene *p*-*i*-*n* homojunction. The temperature and light intensity dependence of the solar cell parameters, such as open-circuit voltage V_{OC} and short-circuit current J_{SC}, of the *p*-*i*-*n* homojunction are investigated in detail. We investigate the single-carrier properties by using another type of pentacene junctions: *p*-*i*-*p* and *n*-*i*-*n* single-carrier homojunctions. The comparison of the rather different dark characteristics and photoconductivity of the two types of homojunctions reveals that the performance of the elementary organic junctions is influenced by a presence of deep carrier trapping states.

6.1.1 Dark Characteristics

Figure 6.1 shows the dark J–V characteristics of the pentacene *p*-*i*-*n* homojunction. The sample structure is also indicated as the inset of Fig. 6.1. Since the effect of series resistance in this region is negligible, we only need to consider a shunt resistance R_p for the standard

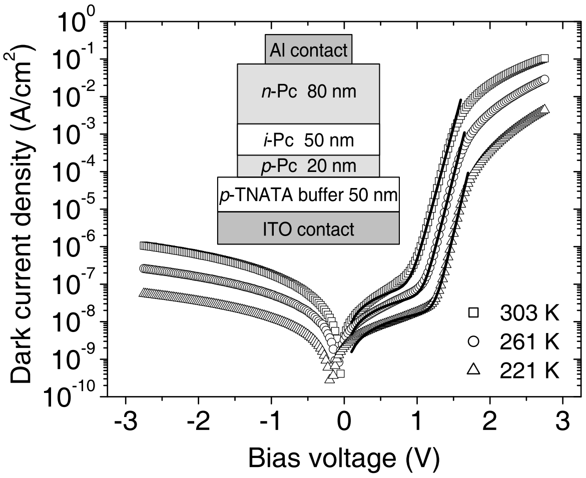

Figure 6.1: Dark J–V characteristics of the p-i-n homojunction at several temperatures (open symbols). The solid lines are the calculated curves in the forward-bias region using Eq. (6.1). The inset shows a schematic picture of the sample structure.

diode equation to describe the realistic dark current density:

$$J_{dark} = \frac{V}{R_p} + J_0(T)\left[\exp\left(\frac{qV}{Ak_BT}\right) - 1\right]. \tag{6.1}$$

In the standard theory, the activation energy of J_0 is correlated with the energy gap E_g. However, as already discussed in Chapter 5, J_0 of an organic homojunction cannot be associated simply with E_g, and A is actually temperature dependent. It is also obvious that the shunt conductance $1/R_p$ is slightly thermally activated. Therefore, a fitting of the J–V curves from Eq. (6.1) necessarily requires a variation of these parameters as temperature is changed. We find 0.13 eV for the activation energy of $1/R_p$ and relatively large values of A increasing with decreasing temperature. A part of the fitting results are listed in Table 6.1.

Table 6.1: Diode parameters for several temperatures obtained from the dark J–V characteristics of the p-i-n homojunction obtained by Eq. (6.1).

T (K)	R_p ($\Omega\,\mathrm{cm}^2$)	J_0 (A/cm^2)	A
303	1.05×10^{7}	2.15×10^{-10}	2.30
261	2.18×10^{7}	1.81×10^{-12}	2.49
221	6.37×10^{7}	1.48×10^{-14}	2.81

6.1.2 Photovoltaic Properties

We now discuss the photovoltaic properties of the pentacene *p-i-n* homojunctions. As can be seen in Fig. 6.2, under illumination of a sun simulator, the homojunction exhibits a V_{OC} of nearly 1.1 V at room temperature, which is about 52 % of the energy gap. The photocurrent is linearly dependent on the bias voltage in the range below V_{OC}, indicating that field-induced dissociation [38,102] is the dominant mechanism for the free-carrier generation. Therefore, the photocurrent density does not saturate at zero bias, yielding a relatively low J_{SC} of $32\,\mu\mathrm{A/cm}^2$. This is a natural consequence of the homojunction structure containing no specific charge separation interface.

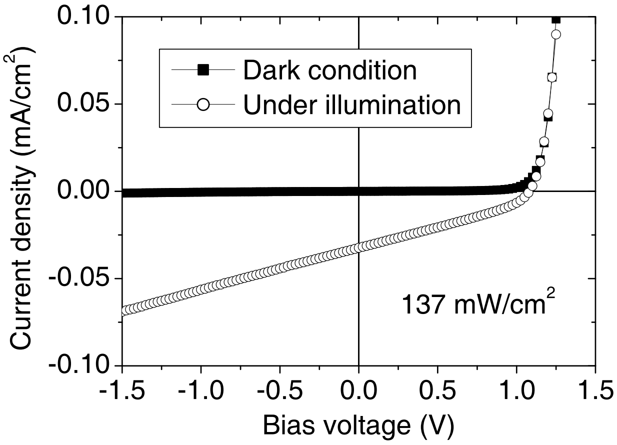

Figure 6.2: *J-V* characteristics of the *p-i-n* homojunction at room temperature under illumination of $137\,\mathrm{mW/cm}^2$ light from a sun simulator. The dark current is also shown for comparison.

Short-Circuit Current

Despite the low current density, the dependence of the photocurrent on light intensity and temperature gives important information on the carrier loss mechanism. Figure 6.3 shows J_{SC} as a function of light intensity I_L at various temperatures. It is known that in a photovoltaic system, the scaling factor α of a power law $J_{SC} \propto I_L^{\alpha}$ ranges from 0.5 to 1, depending on the carrier recombination mechanism. If oppositely charged free carriers are simultaneously present and statistically independent of each other, the carrier recombination is bimolecular [41]; in this case, α typically shows a value of 0.5. In Fig. 6.3, a nonlinearity of J_{SC} to I_L is seen at high temperatures: α is about 0.78 under weak illumination, and as I_L increases, α decreases to 0.57. The reduced value of α can be attributed to the increasing number of electrons and holes both present in the *i*-layer.

It has been reported that for polymeric photovoltaic devices, α has a value of 0.75 when the photocurrent is limited by space charges [103]. However, as it will be shown in the following Subsection, a consideration of space-charge-limited conduction (SCLC) is not relevant for

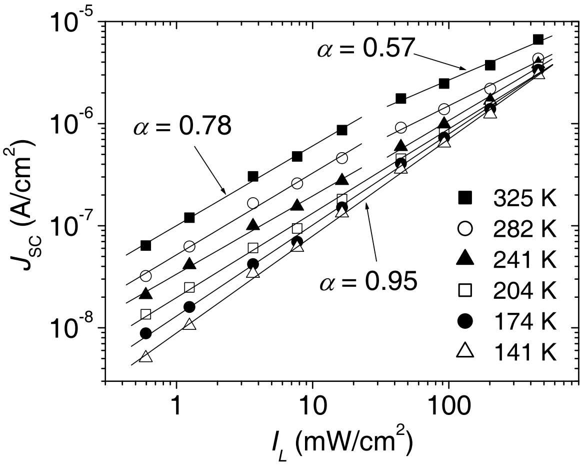

Figure 6.3: Short-circuit current J_{SC} of the *p*-*i*-*n* homojunction at various temperatures as a function of illumination intensity I_L of a xenon lamp. The solid lines indicate a linear fit of the double-logarithm plots, which yield the scaling factor α at each temperature.

our organic homojunctions as the *i*-layer is only several tens of nanometers thick. Therefore, the intermediate value of $\alpha = 0.78$ under low illumination seen in Fig. 6.3 would be due to a low generation rate of free carriers, so that the bimolecular recombination cannot dominate the geminate recombination that is of monomolecular type [16].

On the other hand, a linear response of J_{SC} to I_L usually means that no bimolecular recombination loss is taking place in a photovoltaic cell. In Fig. 6.3, the value of α appears to approach unity as temperature is decreased and is 0.95 at 141 K. The probability of bimolecular recombination is obviously small at low temperatures, but it does not necessarily mean a decrease in the number of both types of carriers. Even at such low temperatures, J_{SC} can reach a comparably high current density of 10^{-6} A/cm^2, indicating that stronger illumination leads to much enhanced charge carrier generation at any temperature. Therefore, the behaviour would be more reasonably attributed to a change in the type of recombination from a bimolecular to a monomolecular one, rather than just to a change in the free-carrier densities. A possible explanation is that one of the two types of carrier, either hole or electron, tends to become immobile when the temperature is decreased, whilst they are almost equally mobile at high temperatures. We will discuss in the next Section details of the individual transport properties of electrons and holes in the homojunctions, which support this explanation.

Open-Circuit Voltage

The open-circuit voltage seen in Fig. 6.2 is actually lower than the expected V_{bi} of 1.65 V for the *p*-*i*-*n* homojunction. However, with a variation of temperature, a drastic change of V_{OC} is observed. Figure 6.4 shows V_{OC} as a function of I_L at various temperatures. It can

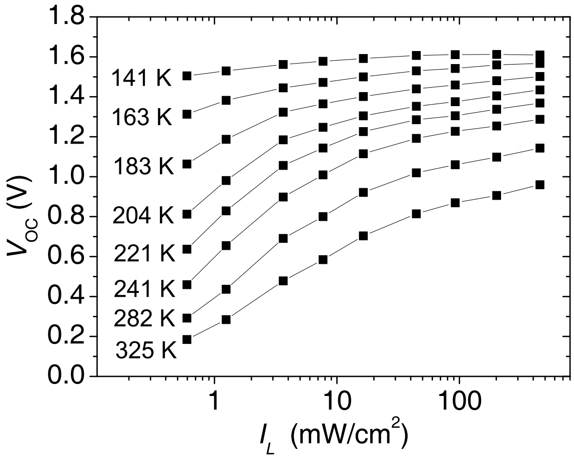

Figure 6.4: Open-circuit voltage V_{OC} of the *p*-*i*-*n* homojunction at various temperatures versus illumination intensity I_L of a xenon lamp. The solid lines are guides for the eye.

be clearly seen that V_{OC} increases with decreasing temperature, being 1.61 V at 141 K, and appears to approach the maximum value limited by V_{bi}. The limitation is due to the fact that the electrochemical energy per electron-hole pair resulting from a strong illumination cannot be fully converted to electrical energy under open-circuit condition [104].

On the other hand, it can be also seen that V_{OC} is generally low under weak illumination and it increases with increasing I_L. In terms of standard solar cell theory, V_{OC} is proportional to the natural logarithm of photocurrent density and, hence, to the natural logarithm of light intensity; i.e., $V_{OC} \propto \ln I_L$. However, no such relation is evidently found in the semilogarithm plots of V_{OC} versus I_L for the homojunction.

The deviation from the standard solar cell model is easily explained by comparison of the dark and illuminated *J*–*V* characteristics. Since V_{OC} is the point where carrier loss mechanisms equal the photogeneration rate, we can associate the dark current density J_{dark} and the photogenerated current density J_{photo} due to the fact that they are balanced at V_{OC}:

$$J_{dark}|_{V=V_{OC}} = - \left. J_{photo}\right|_{V=V_{OC}} . \tag{6.2}$$

In the idealized case, J_{photo} is constant and equal to J_{SC}. Here, we assume that J_{photo} is not saturated, but linearly increases with electric field due to the modified Onsager model [38,102] and that the temperature dependence of the generation rate is negligible compared to the field dependence. The photocurrent density can be calculated with the values of J_{SC} and V_{OC} at each temperature. From the illuminated *J*–*V* characteristics (see Fig. 6.2), we obtain the nonsaturation factor $\vartheta = 0.745$ for a photocurrent density per unit voltage with respect to J_{SC}. Equation (6.2) can be then rewritten in an empirical form

$$\frac{V_{OC}}{R_p(T)} + J_0(T)\left[\exp\left(\frac{qV_{OC}}{A(T)k_BT}\right) - 1\right] = -J_{SC}(T)\left[1 - \vartheta V_{OC}(T)\right]. \tag{6.3}$$

Figure 6.5 shows the calculated J_{photo} from the right-hand side of Eq. (6.3) together with

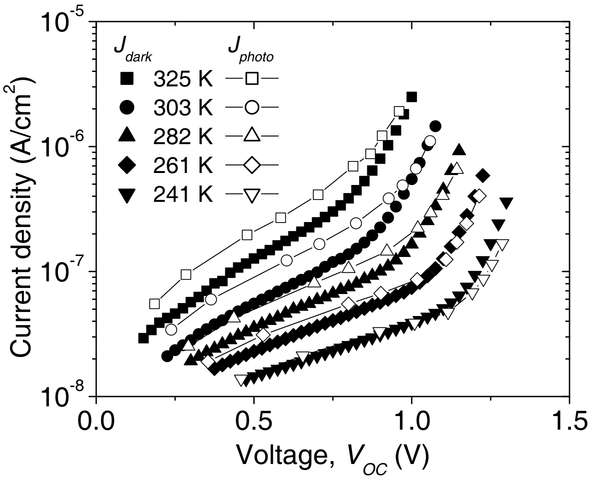

Figure 6.5: Comparison of the dark current density J_{dark} (closed symbols) and the photocurrent density J_{photo} (open symbols) calculated from Eq. (6.3) with the J_{SC} and V_{OC} data at several temperatures.

the measured J_{dark} in a small forward-bias range. It is evident that the characteristics of J_{photo} and J_{dark} are nearly identical at each temperature, and therefore Eq. (6.3) is a correct assumption. This means that in order to reach equilibrium, V_{OC} must follow a voltage regulated by J_{dark}: In other words, V_{OC} is reduced by a voltage drop due to the shunt current.

Thus, because of the relatively low photocurrent density in our *p*-*i*-*n* homojunctions, V_{OC} is inevitably lowered by the dark characteristics loss present especially at higher temperatures. However, at lower temperatures, it reveals that the thermodynamic limitation of V_{OC} is essentially determined by the built-in potential, which we can estimate from the carrier statistics of the doped layers, i.e.,

$$qV_{OC} \leq qV_{bi} = E_{Fn} - E_{Fp}. \tag{6.4}$$

The result agrees with the energy conversion model [104] for a homojunction which states that any photogenerated current driven by an excess quasi-Fermi splitting is to be compensated by currents of majority carriers in the *n*- and *p*-layers, generating entropy for Joule heat, which is, however, not necessarily true for a heterojunction.

6.2 Single-Carrier Homojunctions

The high conductivities in *p*- and *n*- layers lead to ohmic behaviour of the currents even at low temperatures. Therefore, without the restriction of contact problems, we can investigate the individual carrier transport properties of holes and electrons by fabrication of *p-i-p* and *n-i-n* single-carrier organic homojunctions. For each type of device, several samples having different thicknesses of the *i*-layer have been prepared. Table 6.2 summarizes the structures and the *i*-thicknesses L_i of the single-carrier homojunctions.

Table 6.2: Structures and *i*-thicknesses of the *p-i-p* and *n-i-n* pentacene homojunctions. Here, *p*-Pc, *i*-Pc, and *n*-Pc denote the *p*-, *i*-, and *n*-layer of pentacene, respectively.

Type	Structure (thickness: nm)	L_i (nm)
p-i-p (plain)	ITO/ *p*-Pc(20)/ *i*-Pc/ *p*-Pc(85)/ Al	50, 85, 120
p-i-p (buffer)	ITO/ *p*-TNATA(50)/ *p*-Pc(20)/ *i*-Pc/ *p*-Pc(30)/ *p*-TNATA(50)/ Au	80, 160, 240
n-i-n	ITO/ *n*-Pc(20)/ *i*-Pc/ *n*-Pc(65–100)/ Al	50, 80, 110, 160, 240, 320

6.2.1 Dark Characteristics

Figure 6.6 shows the comparison of *p-i-p* and *n-i-n* characteristics at room temperature. For *p-i-p* homojunctions, the currents linearly increase with increasing voltages in the low bias range. Although a superlinear increase of the currents is seen in the high bias range, the relation between the current densities for each sample is roughly in proportion to the electric fields in the *i*-layers; i.e., $J \propto 1/L_i$. Therefore, the superlinear increase of the currents cannot be ascribed to occurrence of SCLC, but might be the consequence of an enhanced effective mobility due to the increasing charge density [29–31, 72, 73]. Thus, the current densities in the ohmic regime, J_{ohm}, are essentially expressed by

$$J_{ohm} = \sigma_{ohm} \left(V/L_i \right), \tag{6.5}$$

with a constant conductivity σ_{ohm}.

For *n-i-n* samples, the behaviour is quite different as seen in Fig. 6.6(b). A sample with $L_i = 50\,\mathrm{nm}$ shows completely ohmic characteristics, while other samples with larger L_i show much reduced J_{ohm} in the ohmic regime, and the reduction of J_{ohm} saturates for $L_i > 160\,\mathrm{nm}$. Furthermore, a very steep increase of current is commonly seen in the high-voltage region for the large-L_i samples. The strong thickness dependence of the J–V characteristics infers a space-charge limitation of the currents. However, the relation between the J–V curves with different L_i does not agree with the trap-free SCLC law $J_{SCLC} \propto V^2/L_i^3$; the exponent factors

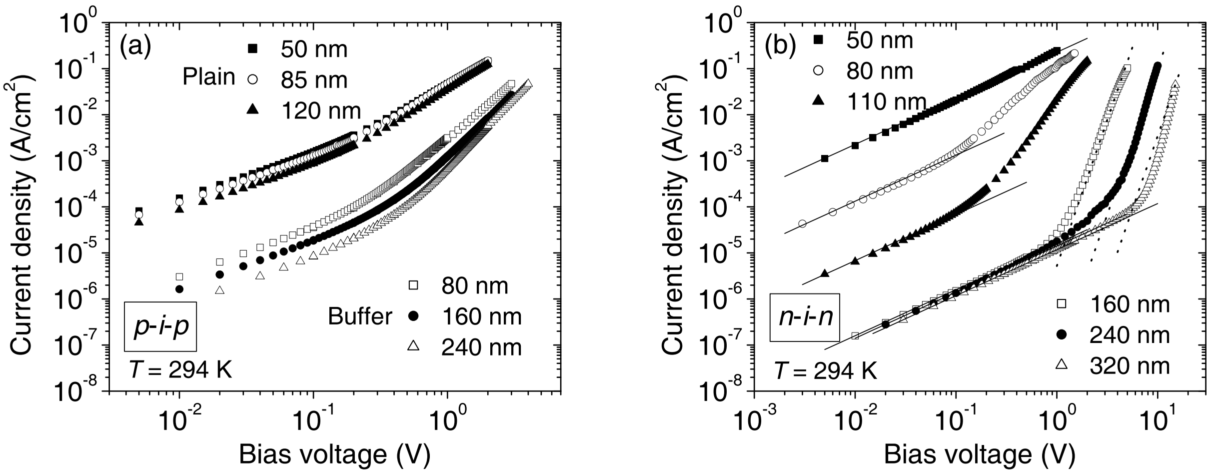

Figure 6.6: Dark J–V characteristics of (a) p-i-p and (b) n-i-n homojunctions with a variety of i-layer thicknesses. The solid lines in (b) are drawn by a linear fit of data to estimate σ_{ohm}. The dotted lines in (b) for three samples are the best fit curves calculated by Eq. (6.6).

for V and L_i are rather large, implying a presence of electron traps. The trap-controlled SCLC is expressed, e.g., for an exponential DOS distribution, as [34]

$$J_{SCLC} \propto \frac{V^{(m+1)}}{L_i^{(2m+1)}} \text{ with } m = \frac{T_C}{T}, \tag{6.6}$$

where T_C is the characteristic parameter which corresponds to the slope of the exponential tail. An attempt to fit Eq. (6.6) to J_{SCLC} data for the samples with $L_i > 160\,\text{nm}$ yields $m = 5.3$ at room temperature [the dotted lines in Fig. 6.6(b)]. However, the temperature dependence of m (not shown here) shows an inconsistency with the model described by Eq. (6.6). Therefore, it can be inferred that the steep increase of J_{SCLC} is not due to a gradual filling of a shallow trap distribution, but is caused by a rapid movement of the quasi-Fermi level through a filling of deep trap states.

6.2.2 Electron Trapping States

The depth of the deep electron trap level can be estimated from the variation of σ_{ohm}. By a linear fit of data in the ohmic regime of Fig. 6.6(b), a variation of σ_{ohm} for each n-i-n sample is achieved, and plotted in Fig. 6.7 as a function of L_i. Since the ohmic current is due to drift of free carriers, σ_{ohm} can be written as

$$\sigma_{ohm} = q\mu n_f \simeq q\mu N_\mu \exp\left(-\frac{E_\mu - E_\Phi}{k_B T}\right), \tag{6.7}$$

where n_f is the free electron density, N_μ is the effective density of states at the transport level, and E_Φ is the quasi-Fermi level in the i-layer. Here, we assume that n_f is different

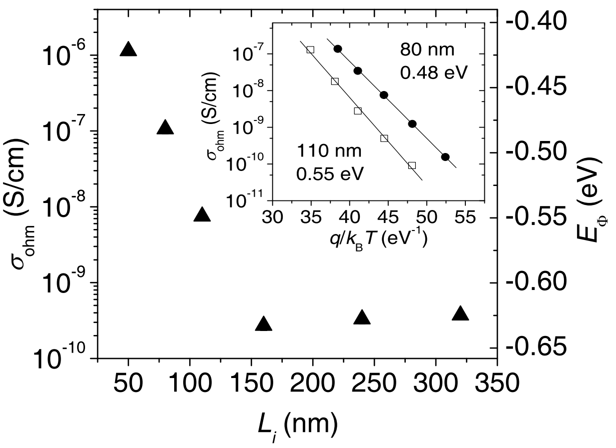

Figure 6.7: Conductivity in the ohmic regime, σ_{ohm}, at room temperature (▲) versus L_i of the n-i-n homojunctions. The right-hand ordinate indicates the corresponding position of the quasi-Fermi level E_Φ measured from the LUMO. Inset shows plots for σ_{ohm} versus reciprocal temperature of the samples with $L_i = 80$ (●) and 110 nm (□), having an activation energy of 0.48 and 0.55 eV, respectively.

from the total injected electron density and it decreases as E_Φ moves downwards. From the temperature dependence of σ_{ohm} (see inset of Fig. 6.7), we can estimate the position of E_Φ measured from the LUMO level, which are -0.48 and -0.55 eV for the samples with $L_i = 80$ and 110 nm, respectively. Accordingly, all σ_{ohm} data in Fig. 6.7 can be associated with the E_Φ levels by means of Eq. (6.7). The E_Φ position is lowered as L_i becomes larger, and it is pinned roughly at -0.63 eV for L_i exceeding 160 nm. The movement of E_Φ would correspond with the degree of electron trapping, and the pinning of E_Φ around -0.63 eV below the LUMO indicates that the deep states are energetically in the immediate vicinity. The total density of deep trap states, N_t, can be estimated by a consideration of the Debye length in the i-layers. The Debye length λ_D characterizes the carrier distribution tail from the n-sides, which would have an effect on the spatial attenuation of E_Φ. Here, λ_D is defined as

$$\lambda_D = \sqrt{\frac{\epsilon_r \epsilon_0 k_B T}{q^2 N_t}}, \tag{6.8}$$

where ϵ_0 is the permittivity of free space. Expecting that the situation at thermal equilibrium is not significantly changed by application of low bias voltages, we can assume for a sufficiently large L_i compared to $2\lambda_D$, the contribution of the electron distribution tail is negligible. Therefore, most of the injected carriers are trapped by the unoccupied deep states in the i-layer, leading to a pinning of E_Φ. On the other hand, when L_i is smaller than approximately $2\lambda_D$, a certain portion of the deep states at the center of the i-layer are already filled due to electron diffusion from the n-sides. This would lead to an increased free-carrier density and hence a variation of E_Φ under a low-bias condition. From the plots in Fig. 6.7, the onset of the E_Φ variation is presumably found at $L_i = 150$ nm. By inserting the critical thickness $L_i/2$ into λ_D of Eq. (6.8), we obtain $1.5\times10^{16}\,\mathrm{cm}^{-3}$ for N_t.

The trap density can be also confirmed in terms of the onset of SCLC under a nonequilibrium steady state: The crossover from J_{ohm} to J_{SCLC} occurs at the voltage V_x when the trap states are filled by the ohmic injection [34], i.e.,

$$V_x = \frac{qN_tL_i^2}{\epsilon_r\epsilon_0}. \tag{6.9}$$

From Fig. 6.6(b), we find V_x approximately at 1.2, 2.8, and 5.1 V for samples with $L_i = 160$, 240, and 320 nm, respectively. Calculations using Eq. (6.9) commonly give a value of $N_t = 1.5 \times 10^{16}\,\mathrm{cm}^{-3}$ for each sample, which is consistent with the aforementioned estimation.

The maximum electron mobility attainable in the *n-i-n* homojunctions can be roughly estimated as $4.3\times10^{-2}\,\mathrm{cm}^2/(\mathrm{Vs})$ by assuming that the effective density of states N_μ in Eq. (6.7) is comparable to the molecular density $2.9\times10^{21}\,\mathrm{cm}^{-3}$. Actually, Eq. (6.7) can properly describe the behaviour of the σ_{ohm} data only at lower temperatures; above room temperature, σ_{ohm} appears to saturate at around $10^{-7}\,\mathrm{S/cm}$ and does not exceed $10^{-6}\,\mathrm{S/cm}$, implying that the carrier transport in the device is limited by other factors, such as geometric resistance or phonon scattering. The *p-i-p* samples show also saturated conductivities of about $10^{-7}\,\mathrm{S/cm}$ at room temperature. Therefore, we expect that electrons and holes have qualitatively the same order of effective mobilities in the *i*-layer of homojunctions at sufficiently high temperatures, in agreement with literature reports [100, 101].

6.2.3 Photoconductivity

The existence of electron deep trap states is more evidently seen in the photoconductivity of the single-carrier devices. Figure 6.8 shows the change in the J–V characteristics of single-carrier homojunctions under illuminated conditions. The *n-i-n* sample exhibits a considerable enhancement of the current density as the light intensity is increased, while the degree of the current enhancement in the *p-i-p* sample is very small. It is therefore obvious that for the *n-i-n* sample, a filling of the deep states by excitation of molecules readily enlarges the portion of free electrons that contributes to the drift currents.

In order to confirm the energetic level E_t of the deep trap states, we have performed a monochromatic excitation of the *n-i-n* sample. The current response is shown in Fig. 6.9 as a function of the excitation energy, together with the absorption spectrum of a pentacene thin film for comparison. A small photocurrent already seen at lower excitation energies infers a small probability of electronic transitions between gap states. It should be noted, however, that a steep increase of the photocurrent arises for a subtle increase of the absorption shoulder, implying that the trap filling dominantly occurs through an electron transfer from the singlet state of a molecule to a neighboring trap site. The efficient charge transfer would suggest that E_t is indeed located at a deeper level than the exciton binding energy.

The origin of the deep states is at present unknown. Such electron traps located at simi-

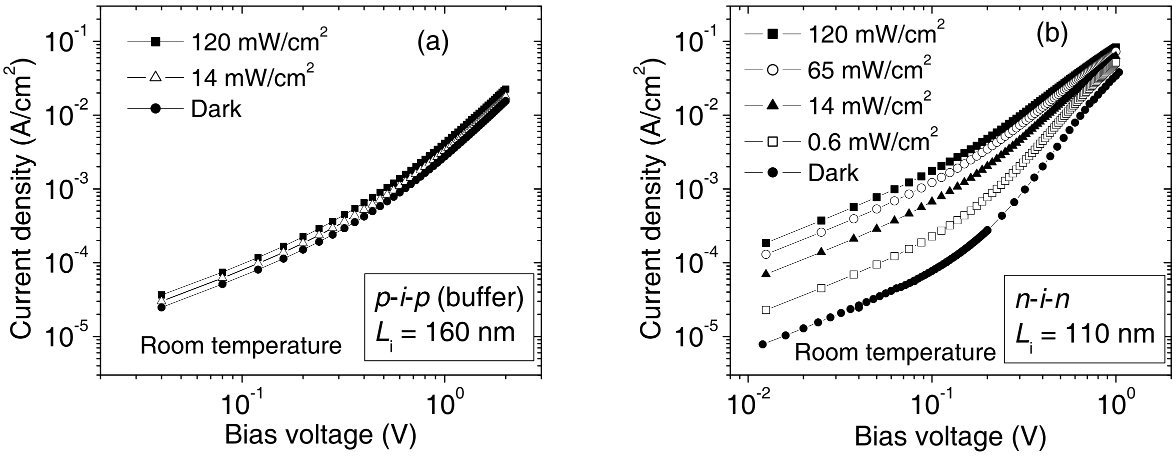

Figure 6.8: Change in the J–V characteristics by illumination of light from a sun simulator with a variety of light intensities for the (a) *p-i-p* and (b) *n-i-n* homojunctions with $L_i = 160$ and $110\,\mathrm{nm}$, respectively.

lar energy levels have been reported for pentacene films utilizing deep-level transient spectroscopy [105]. It is known that oxygen- and hydrogen-induced impurities such as pentacenequinone [60] and dihydropentacene [106] are typically present in pentacene compounds. However, molecular orbital calculations indicate that the LUMO levels of these impurities are located above that of pentacene host; they are basically inert for electron transport. Therefore, we speculate that, in general, no gap state active as electron trap is introduced by these chemical impurities unless the pentacene film is strongly stressed by a bias field [106, 107] or irradiation [108].

The overall energy scheme obtained in this study is summarized as the diagram in Fig. 6.10. By the filling of a neighbouring deep state via a Frenkel exciton state, a geminate pair may be formed. The increasing number of the geminate pairs would not directly contribute to a hole current density, but it does promote a drift current at the electron transport level in pentacene.

6.3 Summary: Performance of Pentacene Homojunctions

We investigate the properties of pentacene *p-i-n* homojunctions having well-rectifying and reproducible diode characteristics. We show that the open-circuit voltage of the pentacene *p-i-n* homojunction is connected to the high built-in voltage of 1.65 V attained by the efficient *p*- and *n*-type doping of pentacene. The thermodynamic limitation of the open-circuit voltage certainly follows the Würfel model which has been successfully applied for the description of inorganic solar cell performance. The monomolecular-type recombination process found in the temperature dependence of the short-circuit current originates from the immobility

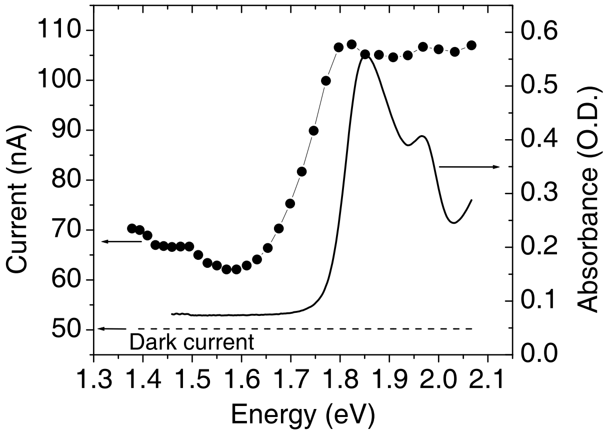

Figure 6.9: Change in the currents (●) by excitation of monochromatic light for the *n*-*i*-*n* homojunction ($L_i = 110\,\mathrm{nm}$) at a constant bias. The dashed line indicates the dark current level of the sample with the same bias. The solid line shows the absorption spectrum of a pentacene thin film with 100 nm thickness.

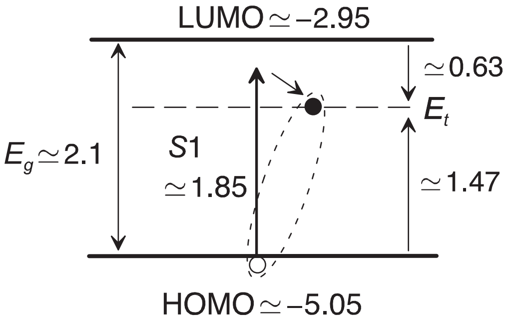

Figure 6.10: Schematic energy diagram of a pentacene thin film, assuming the existence of electron trapping states whose energetic position E_t deeper than the singlet exciton level $S1$.

of electrons at low temperatures. The existence of electron deep states is inferred from the studies for single-carrier-type homojunctions. By combination of electrical and optical measurements, quantitative estimations can be given, revealing that the deep states are located around $-0.63\,\mathrm{eV}$ below the LUMO with the total trap density $1.5{\times}10^{16}\,\mathrm{cm}^{-3}$.

7 Homojunction OLED

We have found in Chapter 5 that the built-in potential of TER004-homojunction is exceptionally high. This matrix actually is an efficient red phosphorescent emitter. Therefore, we can expect electroluminescence from the homojunction structure. In this Chapter, we discuss the performance and the charge balance of the homojunction OLED.

7.1 Red Phosphorescent Homojunction

The rare-earth metal complex TER004 is originally provided for the use as red triplet emitter in OLEDs. Figure 7.1 shows the photoluminescence (PL) spectra of TER004. The isolated compound exhibits a triplet emission at 615 nm, and a broadening and a red-shift of the emission peak typical to an aggregate formation is observed from the thin film.

We have observed that TER004 can be both p- and n-doped efficiently, implying good electron and hole transport properties. A surprisingly high built-in voltage of about 2.2 V for a TER004-homojunction is estimated from the UPS and thermovoltage measurements, and the J–V characteristics show well rectifying behaviour (see Chapter 5). A typical sample structure used in this study and the expected energetics for the TER004-homojunctions are shown in Fig. 7.2. The large thicknesses of the doped layers are chosen so that the optimum light out-coupling is attained.

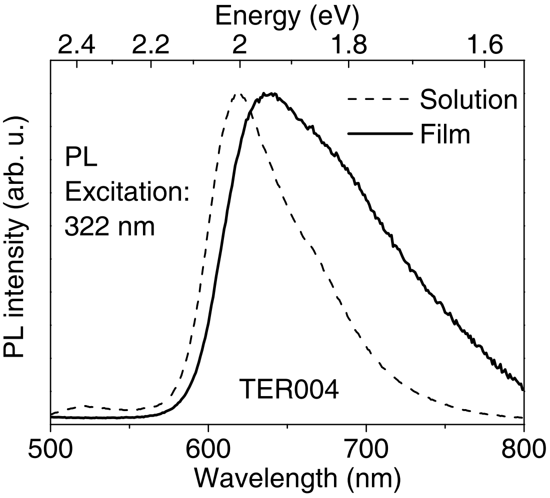

Figure 7.1: Photoluminescence spectra of isolated TER004 in THF solution (2 mg/ℓ) and of solid-state TER004 (100 nm thin-film).

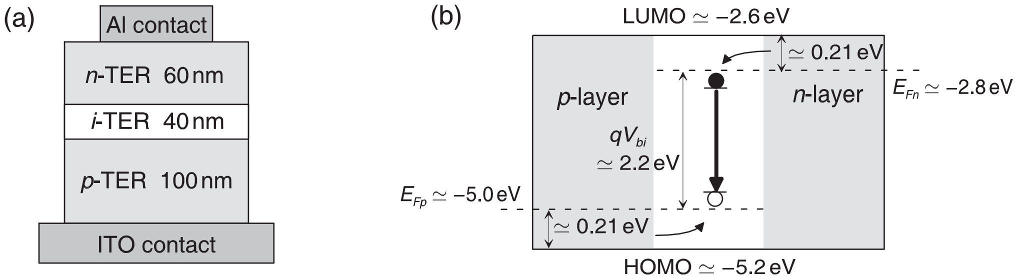

Figure 7.2: (a) Sample structure of a TER004 *p*-*i*-*n* homojunction. (b) Energetic diagram of a TER004 *p*-*i*-*n* homojunction.

7.1.1 Performance of Homo-OLED

Considering the high built-in voltage of TER004 homojnction and the triplet energy of TER004 around 1.9–2.0 eV from the photoluminescence, we can expect a possibility of electroluminescence (EL) using the simple *p*-*i*-*n* structure. Indeed, applying a forward bias, the TER004-homojunction shows fairly intense red light at room temperature. Figure 7.3 presents the performance of the prototype homojunction OLED. Through the transparent anode, visible light is observed with low driving voltages of about 3 V. However, the quantitative evaluations indicate that the quantum yield of our homojunction OLED is much lower than the standards of the currently reported red-OLEDs with a single emission layer: e.g., $100\,\mathrm{cd/cm^2}$ at 3 V with the quantum efficiency $\eta_{ext}^{\mathrm{led}} = 12.4\,\%$ [109].
The low quantum yield of the homojunction OLED can be, e.g., attributed to a self-quenching of the triplet states due to aggregation of the matrix: In general, an aggregate formation provides states for nonradiative recombination such as excimers [110]. Besides that, one of the reasons for the low efficiency could be due to the unbalanced states of electron and hole density in the emission layer under a forward bias, which reduces the probability of exciton formation. In the following, we discuss an approach to examine the charge balance status in the TER004 homojunction.

7.1.2 Examination of Charge Balance

In order to investigate the charge balance status, we additionally prepare test samples with either an electron-blocking or a hole-blocking layer inserted at the respective position in the homojunction as seen in Fig 7.4 (a) and (b), respectively. For the electron blocker, a wide-gap hole transport material MeO-TPD is used; the HOMO level of MeO-TPD is close to that of TER004. For the hole-blocker, a Bphen-derivative electron transport material is provided from Novaled AG; the LUMO level of the hole-blocker is also close to that of TER004.

Figure 7.5 shows the comparison of the *J*–*V* characteristics between the test samples and a

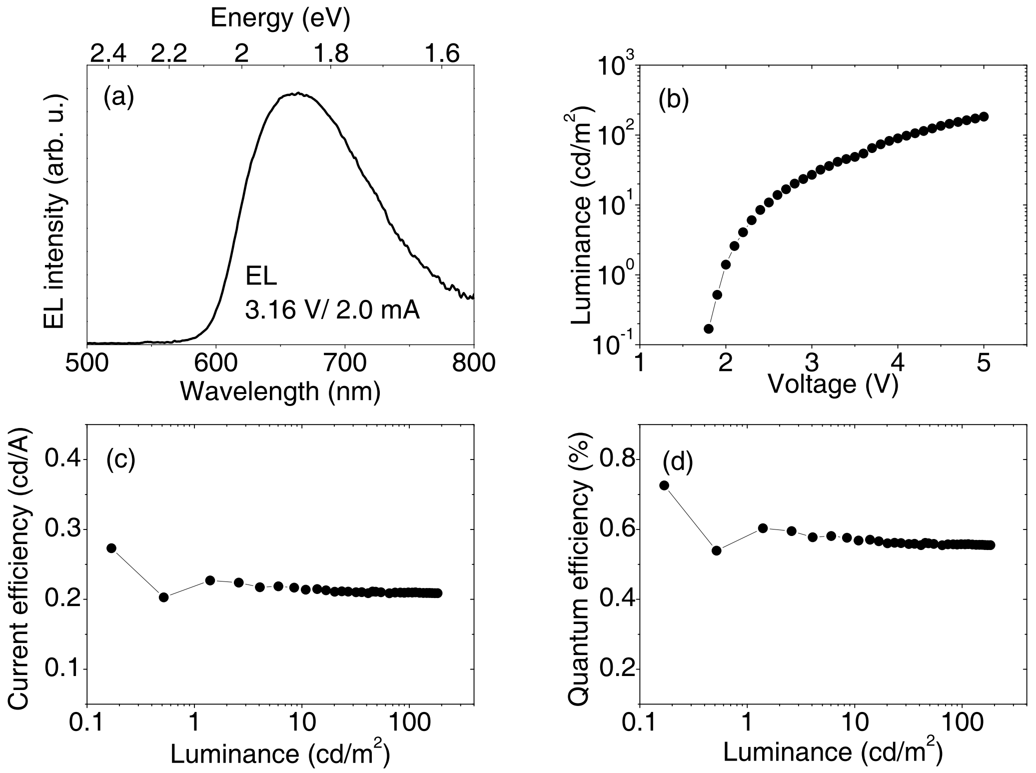

Figure 7.3: EL performance of a TER004 homojunction: (a) EL spectrum; (b) Luminance L_m versus bias voltage; (c) Current efficiency η_L versus L_m; (d) External quantum efficiency $\eta_{ext}^{\mathrm{led}}$ versus L_m.

plain homojunction. The test samples also show well-rectifying diode characteristics similar to that of the plain homojunction. A somewhat reduced forward-bias current is seen for the hole-blocking sample; this might be attributed to a slight LUMO offset between the blocking layer and TER004.

Figure 7.6 shows the comparison of EL performance between the three samples. It can be seen that with the electron-blocker, the performance is improved in the complete current-density range; the sample shows a high luminance with a relatively low driving voltage. On the other hand, the sample with the hole-blocker requires high driving voltages to achieve a high efficiency; the high current efficiency seen at a high luminance is mainly due to the low forward current density. It is obvious that radiative recombination efficiently occurs at the *i*-layer with the electron-blocking layer. Therefore, we can conclude that the electron mobility in the TER004 matrix would be much higher than the hole mobility. This is also consistent with the results of conductivity measurements, where we have found two orders of magnitude higher conductivity for *n*-doped TER004 compared to *p*-doped one.

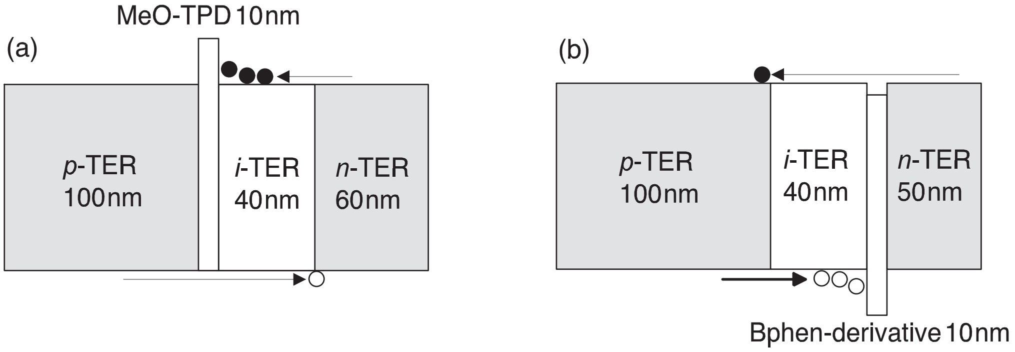

Figure 7.4: Schematics of test samples with (a) an electron-blocking layer and (b) a hole-blocking layer inserted in the homojunction structures.

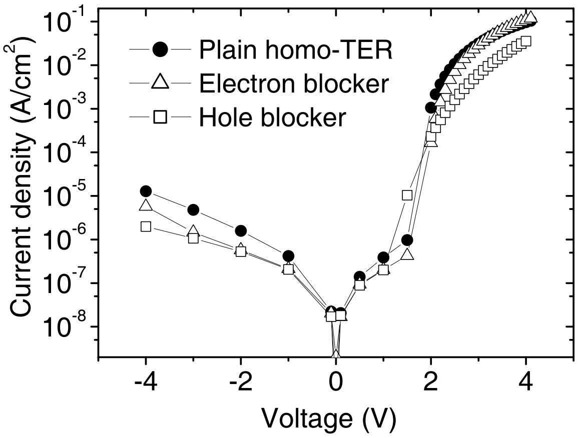

Figure 7.5: Comparison of J–V characteristics between a plain homojunction and test samples with a carrier blocking layer.

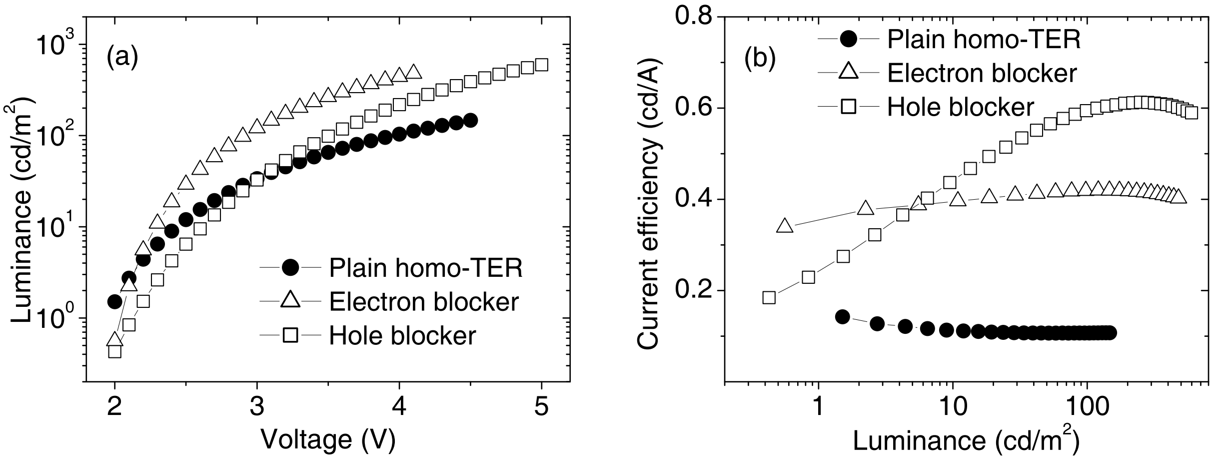

Figure 7.6: Comparison of EL performance between a plain sample and test samples: (a) Luminance L_m versus bias voltage; (b) Current efficiency η_L versus L_m.

7.2 Summary: Homo-OLED Applicaion

A red phosphorescent OLED application is realized using the exceptionally high built-in voltage of 2.2 V in the TER004 *p*-*i*-*n* homojunction, without utilizing any other transport materials. The homo-OLED shows visible emission around 650 nm with low operation voltages. One of the reasons for the relatively low EL efficiency is the unbalanced charge status at the emission layer. We demonstrate that the organic *p*-*i*-*n* homojunction can be used to examine the balance of electron and hole current densities. It is found that the electron transport in TER004 is much more efficient than the hole transport.

8 Conclusions and Outlook

8.1 Conclusions

Field-effect measurements for the electron transport matrix C_{60} doped with the cationic donor AOB are performed to investigate the basic carrier transport properties in doped organic thin films. It is shown that the charge density introduced by the n-doping is sufficient to fill the low-mobility states present in disordered organic films. Unlike all the previous reports for organic thin films, the doping ratio dependence of the C_{60} mobility can be described by the Matthiessen rule generally observed for inorganic semiconductors. Consequently, it becomes possible to discuss the electron scattering mechanisms in C_{60} films. The deviation from the scattering theory is explained by a thermionic emission current at grain boundaries. The strong n-doping with $[\mathrm{Ru(t\text{-}but\text{-}terpy)_2}]^0$ or NDN1 together with the efficient p-dopant allows bipolar doping of large-gap matrices. Thus, we realize organic p-i-n homojunctions of several organic matrices with different energy gaps. Because of the large carrier densities, the Fermi energies in the p- and n-doped layers are experimentally well defined. The energy gap and built-in potential of the organic p-i-n homojunctions can thus be precisely determined. From the photovoltaic response of pentacene homojunctions, it can be concluded that the open-circuit voltage in the organic homojunctions is limited by the built-in potential of 1.65 eV: Photogenerated current with an excess quasi-Fermi splitting cannot be fully converted to the electrical energy. The individual carrier transport properties of electrons and holes are investigated utilizing n-i-n and p-i-p single-carrier organic homojunctions. We observe an influence of electron traps on the transport. The quantitative estimations yield an energy level of $-0.63\,\mathrm{eV}$ and a total density of $1.5\times10^{16}\,\mathrm{cm^{-3}}$ for the electron deep traps. The electron trapping is considered to be the reason for a monomolecular recombination, which is inferred from the temperature dependence of the short-circuit currents.

An application of a p-i-n homojunction in the red phosphorescent OLED is demonstrated. The high built-in potential of 2.2 eV is sufficient for the electroluminescence in the TER004 homojunctions. Using charge-blocking test samples, it turns out that the electron transport in the TER004 matrix is much more efficient than the hole transport.

The above results support the fact that the organic homojunction can be an archetype device to investigate fundamental charge transport properties and related device performances in organic thin-film applications.

8.2 Outlook

The high field-effect mobility found in the *n*-doped C_{60} infers that a band-like transport may be possible even in organic films if a trap-free dielectric interface and/or an elaborate film preparation technique are utilized. Besides, an interesting trial to achieve an improved mobility would be fabrication of a modulation-doped OFET: An undoped layer deposited onto the dielectric, followed by a doped layer; a large charge density would be induced by transfer from the doped to the undoped layer, where no ionized impurity scattering is expected.

The advantages of organic *p*-*i*-*n* structures are the negligible electric field in the doped layers, ohmic contacts with the anode and cathode, and the concomitant low series resistance of the device. This allows a flexible design of the layer thickness. Utilizing many other large-gap matrices, a variety of basic transport studies become possible: The individual charge transport properties of electrons and holes can be studied analogously to the single-carrier studies in the pentacene homojunctions, or the charge balance studies in the TER004 homojunctions; in addition, the exciton diffusion properties in a matrix may be investigated by inserting a quenching layer at a respective position in the homojunction.

For the fabrication of further large-gap organic homojunctions, much stronger donor and acceptor molecules would be required, which could be provided by a a sophisticated chemical synthesis. Such developments are in progress at, e.g., Novaled AG in Dresden, and are also possible by collaboration with a research group in chemistry. The candidates for a new class of homojunction matrices are, e.g., tetraphenylporphyrin and its derivatives, rubrene, etc.

Although the deviation from the conventional Einstein relation is the background of the non-ideality of the diode parameters, an open question remains: The exact meaning of the diode ideality factor in disordered organic homojunctions is not fully clear. For a precise analysis of the *J*–*V* curves at the nonequilibrium steady state, it may be necessary to consider the real band-bending, the recombination rate, and the quasi-Fermi profile in the *i*-layer.

Bibliography

[1] W. Warta and N. Karl, Phys. Rev. B **32**, 1172 (1985).

[2] K. Harada, A. G. Werner, M. Pfeiffer, C. J. Bloom, C. M. Elliott, and K. Leo, Phys. Rev. Lett. **94** 036601 (2005).

[3] M. Pfeiffer, A. Beyer, T. Fritz, and K. Leo, Appl. Phys. Lett. **73**, 3202 (1998).

[4] J. Endo, T. Matsumoto, and J. Kido, Jpn. J. Appl. Phys. **41**, L358 (2002).

[5] W. Gao and A. Kahn, Appl. Phys. Lett. **79**, 4040 (2001).

[6] A. Werner, F. Li, K. Harada, M. Pfeiffer, T. Fritz, and K. Leo, Appl. Phys. Lett. **82**, 4495 (2003).

[7] F. Li, A. Werner, M. Pfeiffer, K. Leo, and X. Liu, J. Phys. Chem. B **178**, 17076 (2004).

[8] F. Li, M. Pfeiffer, A. Werner, K. Harada, K. Leo, N. Hayashi, K. Seki, X. Liu, and X.-D. Dang, J. Appl. Phys. **100**, 023716 (2006).

[9] C. J. Bloom, C. M. Elliott, P. G. Schroeder, C. B. France, and B. A. Parkinson, J. Phys. Chem. B **107**, 2933 (2003).

[10] E. A. Silinsh, *Organic Molecular Crystals: Their Electronic States*, pp. 29, 84, 127, 162 (Springer-Verlag, Berlin, 1980).

[11] E. A. Silinsh and V. Gepak, *Organic Molecular Crystals: Interaction, Localization and Transport Phenomena*, pp. 2, 125, 169 (American Institute of Physics, New York, 1994).

[12] J. Simon and J.-J. André, *Molecular Semiconductors*, p. 30 (Springer-Verlag, Berlin, 1985).

[13] G. H. Wannier, Phys. Rev. **52**, 191 (1937).

[14] J. Frenkel, Phys. Rev. **54**, 647 (1938).

[15] L. E. Lyons, J. Chem. Soc., 5001 (1957).

[16] M. Pope and C. E. Swenberg, *Electronic Processes in Organic Crystals and Polymers*, pp. 71, 74, 135, 509 (Oxford University Press, New York, 1999).

[17] N. W. Ashcroft and N. D. Mermin, *Solid State Physics*, pp. 447, 553, 612 (Saunders College Publishing, Fort Worth, 1976).

[18] L. Friedman, Phys. Rev. **133**, 191 (1964).

[19] L. B. Schein, Phys. Rev. B **2**, 1024 (1977).

[20] P. W. Anderson, Phys. Rev. **109**, 1492 (1958).

[21] H. Böttger and V. V. Bryksin, *Hopping Conduction in Solids*, pp. 88, 105 (Akademie-Verlag, Berlin, 1985).

[22] J. T. Edwards and D. Thouless, J. Phys. C: Solid State Phys. **5**, 807 (1972).

[23] N. F. Mott, Adv. Phys. **16**, 49 (1967).

[24] M. Cunter and N. F. Mott, Phys. Rev. **181**, 1336 (1969).

[25] A. Miller and E. Abrahams, Phys. Rev. **120**, 745 (1960).

[26] V. Ambegaokar, B. I. Halperin, and J. S. Langer, Phys. Rev. B **4**, 2612 (1971).

[27] N. F. Mott, Phil. Mag. **19**, 835 (1969).

[28] H. Bässler, Phys. Stat. Sol. B **175**, 15 (1993).

[29] M. C. J. M. Vissenberg and M. Matters, Phys. Rev. B **57**, 12 964 (1998).

[30] B. Maennig, M. Pfeiffer, A. Nollau, X. Zhou, K. Leo, and P. Simon, Phys. Rev. B **64**, 195208 (2001).

[31] G. Horowitz, R. Hajlaoui, and P. Delannoy, J. Phys. III France **5**, 355 (1995); G. Horowitz, M. E. Hajlaoui, and R. Hajlaoui, J. Appl. Phys. **87**, 4456 (2000).

[32] W. Shockley, Bell Syst. Tech. J. **28**, 435 (1949).

[33] S. M. Sze, *Physics of Semiconductor Devices*, 2nd ed., pp. 248–258, 438 (Wiley, New York, 1981).

[34] M. A. Lampert and P. Mark, *Current Injection in Solids* (Academic Press, New York, 1970).

[35] S. Nešpurek and E. A. Silinsh, Phys. Stat. Sol. A **34**, 747 (1976).

[36] M. Hack and M. Shur, J. Appl. Phys. **58**, 997 (1985).

[37] B. Sapoval and C. Hermann, *Physics of Semiconductors*, p. 226 (Springer, New York, 1995).

[38] L. Onsager, Phys. Rev. **54**, 554 (1938).

[39] R. H. Batt, C. L. Braun, and J. F. Hornig, J. Chem. Phys. **49**, 1967 (1969); R. R. Chance and C. L. Braun, J. Chem. Phys. **59**, 2269 (1973).

[40] E. A. Silinsh, V. A. Kolesnikov, I. J. Muzikante, and D. R. Balode, Phys. Stat. Sol. B **113**, 379 (1982).

[41] P. Langevin, Annales de Chimie et de Physique **28**, 289 (1903).

[42] C. W. Tang, Appl. Phys. Lett. **48**, 183 (1986).

[43] J. Xue, S. Uchida, B. P. Rand, and S. R. Forrest, Appl. Phys. Lett. **85**, 5757 (2004).

[44] C. W. Tang and S. A. VanSlyke, Appl. Phys. Lett. **51**, 913 (1987).

[45] D. R. Kearns, G. Tollin, and M. Calvin, J. Chem. Phys. **32**, 1020 (1960).

[46] M. Maitrot, G. Guillaud, B. Boudjema, J.-J. André, and J. Simon, J. Appl. Phys. **60**, 2369 (1986).

[47] A. Nollau, M. Pfeiffer, T. Fritz, and K. Leo, J. Appl. Phys. **87**, 4340 (2000).

[48] J. Blochwitz, M. Pfeiffer, T. Fritz, K. Leo, D. M. Alloway, P. A. Lee, and N. R. Armstrong, Organic Electronics **2**, 97 (2001).

[49] Fullerene C_{60} doped with 2 mol% NDN1-type molecules (from Novaled AG), measured in this work, unpublished.

[50] P. A. Heiney, J. E. Fisher, A. R. McGhhie, W. J. Romanow, A. M. Denestejn, J. P. McCauley Jr., A. B. Smith III, and D. E. Cox, Phys. Rev. Lett. **66**, 2911 (1991).

[51] R. C. Haddon, A. F. Hebard, M. J. Rosseinsky, D. W. Murphy, S. J. Duclos, K. B. Lyons, B. Miller, J. M. Rosamilia, R. M. Fleming, A. R. Kortan, S. H. Glarum, A. V. Makhija, A. J. Muller, R. H. Wick, S. M. Zahurak, R. Tycko, G. Dabbagh, and F. A. Thiel, Nature **350**, 320 (1991); A. F. Hebard, M. J. Rosseinsky, R. C. Haddon, D. W. Murphy, S. H. Glarum, T. T. M. Palstra, A. P. Ramirez, and A. R. Kortan, Nature **350**, 600 (1991).

[52] A. Bernanose, British Journal of Applied Physics **4**, S56 (1953).

[53] A. Dodabalapur, H. E. Katz, L. Torsi, and R. C. Haddon, Science **269**, 1560 (1995).

[54] C. C. Leznoff and A. B. P. Lever, *Phthalocyanines: Properties and Applications*, p. 295 (VCH Publishers, New York, 1989).

[55] J. Lee, S. S. Kim, K. Kim, J. H. Kim, and S. Im, Appl. Phys. Lett. **84**, 1701 (2004).

[56] S. Yoo, B. Domercq, and B. Kippelen, Appl. Phys. Lett. **85**, 5427 (2004).

[57] A. K. Pandey, S. Dabos-Seignon, and J.-M. Nunzi, Appl. Phys. Lett. **89**, 113506 (2006).

[58] Z. R. Hong, R. Lessmann, B. Maennig, Q. Huang, K. Harada, M. Riede, and K. Leo, Appl. Phys. Lett., submitted.

[59] S. Lee, B. Koo, J. Shin, E. Lee, H. Park, and H. Kim, Appl. Phys. Lett. **88**, 162109 (2006).

[60] O. D. Jurchescu, J. Baas, and T. T. M. Palstra, Appl. Phys. Lett. **84**, 3061 (2004).

[61] L. B. Coleman M. J. Cohen, D. J. Sandman, F. J. Yamagishi, A. F. Garito, and A. J. Heeger, Solid State Commun. **12**, 1125 (1973).

[62] R. S. Potember, P. O. Poehler, and D. O. Cowan, Appl. Phys. Lett. **34**, 405 (1979).

[63] B. O'Regan and M. Grätzel, Nature **353**, 737 (1991).

[64] M. K. Nazeeruddin, P. Péchy, and M. Grätzel, Chem. Commun. **34**, 1705 (1997).

[65] C. M. Elliott, private communication.

[66] Y. Jean, *Molecular Orbitals of Transition Metal Complexes*, p. 150 (Oxford University Press, Oxford, 2005).

[67] D. E. Morris, K. W. Hanck, and M. K. DeArmond, J. Am. Chem. Soc. **105**, 3032 (1983); D. E. Morris, K. W. Hanck, and M. K. DeArmond, J. Electroanal. Chem. **149**, 115 (1983).

[68] N. H. Liu and D. Emin, Phys. Rev. B **6**, 3250 (1984).

[69] H. Fritzsche, Solid State Commun. **9**, 1813 (1971).

[70] Y. Shirota and H. Kageyama, Chem. Rev. **107**, 953 (2007).

[71] V. Podzorov, E. Menard, A. Borissov, V. Kiryukhin, J. A. Rogers, and M. E. Gershenson, Phys. Rev. Lett. **93**, 086602 (2004).

[72] Y. Roichman, Y. Preezant, and N. Tessler, Phys. Stat. Sol. A **201**, 1246 (2004).

[73] W. F. Pasveer, J. Cottaar, C. Tanase, R. Coehoorn, P. A. Bobbert, P. W. M. Blom, D. M. de Leeuw, and M. A. J. Michels, Phys. Rev. Lett. **94**, 206601 (2005).

[74] T. B. Singh, N. Marjanovic, G. J. Matt, S. Gnes, N. S. Sariciftci, A. Montaigne Ramil, A. Andreev, H. Sitter, R. Schwödiauer, and S. Bauer, Organic Electronics **6**, 105 (2005).

[75] T. D. Anthopoulos, B. Singh, N. Marjanovic, N. S. Sariciftci, A. Montaigne Ramil, H. Sitter, M. Cölle, and D. M. de Leeuw, Appl. Phys. Lett. **89**, 213504 (2006).

[76] K. Itaka, M. Yamashita, J. Yamaguchi, M. Haemori, S. Yaginuma, Y. Matsumoto, M. Kondo, and H. Koinuma, Adv. Mater. **18**, 1713 (2006).

[77] A. R. Völkel, R. A. Street, and D. Knipp, Phys. Rev. B **66**, 195336 (2002).

[78] A. Tapponnier, I. Biaggio, and P. Günter, Appl. Phys. Lett. **86**, 112114 (2005).

[79] L.-L. Chua, J. Zaumsell, J.-F. Chang, E. C.-W. Ou, P .K.-Ho, H. Sirringhaus, and R. H. Friend, Nature **434**, 194 (2005).

[80] J. Bardeen and W. Shockley, Phys. Rev. **80**, 72 (1950).

[81] E. Conwell and V. F. Weisskopf, Phys. Rev. **77**, 388 (1950).

[82] S. F. Nelson, Y.-Y. Lin, D. J. Gundlach, and T. N. Jackson, Appl. Phys. Lett. **72**, 1854 (1998).

[83] O. Ostroverkhova, D. G. Cooke, S. Shcherbyna, R. F. Egerton, and F. A. Hegmann, Phys. Rev. B **71**, 035204 (2005).

[84] J. W. Orton and M. J. Powell, Rep. Prog. Phys. **43**, 1263 (1980).

[85] R. A. Street, J. E. Northrup, and A. Salleo, Phys. Rev. B **71**, 165202 (2005).

[86] A. B. P. Lever, Inorg. Chim. Acta **203**, 171 (1993).

[87] Determined by cyclic voltammetry (Fc/Fc$^+$) in THF solution, measured at Novaled AG (Dresden, Germany), unpublished.

[88] H. Matsuura, A. Matsuda, H. Okushi, and K. Tanaka, J. Appl. Phys. **58**, 1578 (1985).

[89] S. S. Hegedus, N. Salzman, and E. Fagan, J. Appl. Phys. **63**, 5126 (1988).

[90] A. Mittiga, P. Florini, M. Falconieri, and F. Evangelisti, J. Appl. Phys. **66**, 2667 (1989).

[91] K. Yamashita, Y. Kunugi, Y. Harima, and A. Chowdhury, Jpn. J. Appl. Phys. **34**, 3794 (1995).

[92] M. Hiramoto, K. Ihara, and M. Yokoyama, Jpn. J. Appl. Phys. **34**, 3803 (1995).

[93] S. Hamm and H. Wachtel, J. Chem. Phys. **103**, 10689 (1995).

[94] Q. Pei, G. Yu, C. Zhang, Y. Yang, and A. J. Heeger, Science **269**, 1086 (1995).

[95] A. von Mühlenen, N. Errien, M. Schaer, M.-N. Bussac, and L. Zuppiroli, Phys. Rev. B **75**, 115338 (2007).

[96] S. D. Baranovskii, T. Faber, F. Hensel, and P. Thomas, Phys. Stat. Sol. (b) **205**, 87 (1998).

[97] Y. Roichman and N. Tessler, Appl. Phys. Lett. **80**, 1948 (2002).

[98] R. Richert, L. Pautmeier, and H. Bässler, Phys. Rev. Lett. **63**, 547 (1989).

[99] G. Paasch, Th. Lindner, C. Rost-Bietsch, S. Karg, W. Riess, and S. Scheinert, J. Appl. Phys. **98**, 084505 (2005).

[100] R. Schmechel, M. Ahles, and H. von Seggern, J. Appl. Phys. **98**, 084511 (2005).

[101] Th. B. Singh, F. Meghdadi, S. Günes, N. Marjanovic, G. Horowitz, P. Lang, S. Bauer, and N. S. Sariciftci, Adv. Mater. **17**, 2315 (2005).

[102] R. R. Chance and C. L. Braun, J. Chem. Phys. **59**, 2269 (1973).

[103] V. D. Mihailetchi, J. Wildeman, and P. W. M. Blom, Phys. Rev. Lett. **94**, 126602 (2005).

[104] P. Würfel, *Physics of Solar Cells: From Principles to New Concepts* (Wiley-VCH, Weinheim, 2005), p. 93.

[105] Y. S. Yang, S. H. Kim, J.-I. Lee, H. Y. Chu, L.-M. Do, H. Lee, J. Oh, T. Zyung, M. K. Ryu, and M. S. Jang, Appl. Phys. Lett. **80**, 1595 (2002).

[106] J. E. Northrup and M. L. Chabinyc, Phys. Rev. B **68**, 041202(R) (2003).

[107] G. Gu, M. G. Kane, J. E. Doty, and A. H. Firester, Appl. Phys. Lett. **87**, 243512 (2005).

[108] R. Plugaru, C. Anghel, and A. M. Ionescu, in *Proceedings of CAS 2006 International Semiconductor Conference* (IEEE, 2006), vol. 2, p. 315.

[109] R. Meerheim, K. Walzer, G. He, and K. Leo, in *Proceedings of Organic Optoelectronics and Photonics II* (SPIE, 2006), vol. 6192, p. 61920.

[110] V. Bulović, A. Shoustikov, M. A. Baldo, E. Bose, V. G. Kozlov, M. E. Thompson, and S. R. Forrest, Chem. Phys. Lett. **287**, 455 (1998).

Acknowledgements

Many people have helped and contributed to the thesis presented here. I would like to express sincere gratitude to my supervisor Prof. Dr. K. Leo for giving me the great opportunity to do my thesis work at the Insitut für Angewandte Photophysik (IAPP) of the Technische Universität Dresden. I also thank him for insightful discussions and proof-reading of the manuscript of this thesis and other publications. I wish to thank Dr. A. G. Werner at Novaled AG and Dr. F. Li at Linköping university since the work was initially supported by their continuous help. I also thank Dr. M. Pfeiffer and Dr. B. Maennig at Heliatek GmbH for helpful suggestions and discussions. They introduced me to the study of organic semiconductors with deep knowledge and insight.

I am grateful for advice and support from Dr. M. Riede and Dr. K. Walzer at IAPP: It was due to their continuous help that I could carry out the thesis, publications, and presentations. Discussions with Dr. R. Schüppel, C. Uhrich, K. Schulze, R. Lessmann, and other solar-cell group members have been great help, and motivated me to perform the photovoltaic studies. S. Olthof helped me in UPS measurements. S. Pfützner gave me insightful comments on the thesis. Advice from G. Schwartz for OLED measurements and information on red OLED from R. Meerheim have been necessary to complete the thesis. Technical support by C. Kolberg and C. Wolf has been always great help to me. I also acknowledge the support from all people at IAPP. I really enjoyed the pleasant atmosphere of cooperation and friendship.

I wish to acknowledge Prof. Dr. G. Paasch and Prof. Dr. M. Hiramoto for their willingness to prepare reports on this thesis. My gratitude is also expressed towards Prof. Dr. C. M. Elliott at Colorado State University for providing a variety of n-dopant molecules, which are the key to success in the studies of homojunctions. I gratefully thank Dr. O. R. Hild at IPMS Fraunhofer Institut for providing pentacene compounds: He also contributed a lot of information on the impurities in the pentacene: Contribution from Prof. Dr. D. Wöhrle and colleagues at the University of Bremen is also acknowledged.

Financial support by the Deutsche Forschungsgemeinschaft (Grants No. LE 747/35-1 and Leibniz prize) is gratefully acknowledged.

Versicherung

Hiermit versichere ich, daß ich die vorliegende Arbeit ohne unzulässige Hilfe Dritter und ohne Benutzung anderer als der angegebenen Hilfsmittel angefertigt habe; die aus fremden Quellen direkt oder indirekt übernommenen Gedanken sind als solche kenntlich gemacht. Die Arbeit wurde bisher weder im Inland noch im Ausland in gleicher oder ähnlicher Form einer anderen Prüfungsbehörde vorgelegt.

Diese Arbeit wurde am Institut für Angewandte Photophysik der Technischen Universität Dresden unter der wissenschaftlichen Betreuung von Prof. Dr. Karl Leo angefertigt.

Ich erkenne die Promotionsordnung der Fakultät Mathematik und Naturwissenschaften der Technischen Universität Dresden vom 20. März 2000 an.

Dresden, den 06. März 2008

(Kentaro Harada)